Trabajo Fin de Máster
Ingeniería Aeronáutica

Transonic CFD Analysis of an External Store Carried on a Military Aircraft Wing

Autor: José Ignacio Rico Álvarez
Tutor: Francisco Gavilán Jiménez

Dpto. Ingeniería Aeroespacial y Mecánica de Fluidos
Escuela Técnica Superior de Ingeniería
Universidad de Sevilla
Sevilla, 2022

Trabajo Fin de Máster
Ingeniería Aeronáutica

Transonic CFD Analysis of an External Store Carried on a Military Aircraft Wing

Autor:
José Ignacio Rico Álvarez

Tutor:
Francisco Gavilán Jiménez
Profesor Contratado Doctor

Dpto. Ingeniería Aeroespacial y Mecánica de Fluidos
Escuela Técnica Superior de Ingeniería
Universidad de Sevilla
Sevilla, 2022

Trabajo Fin de Máster: Transonic CFD Analysis of an External Store Carried on a Military Aircraft Wing

Autor: José Ignacio Rico Álvarez

Tutor: Francisco Gavilán Jiménez

El tribunal nombrado para juzgar el Trabajo arriba indicado, compuesto por los siguientes miembros:

Presidente:

Vocales:

Secretario:

Acuerdan otorgarle la calificación de:

Fecha:

El Secretario del Tribunal

Abstract

A good understanding of physics in carriage and release of external stores from an aircraft is of primary concern to military aircraft designers. The flow field encountered on stores in the vicinity of an aircraft is usually very complex due to mutual interferences. This situation sharpens when transonic fluid flows are considered. Traditionally, designers have resorted to wind tunnel tests to assess these and other questions. However, recent years have seen an emergence of application of CFD methods as a cheaper alternative since they provide accurate results when the appropriate models are applied.

The main aim of this TFM is to validate an inviscid flow solution based on an unstructured grid approach over a stationary wing/pylon/store configuration. The efficiency of the designed setup is compared, when possible, against published literature and experimental data. Rigid body aerodynamics and mutual interference effects are explored to justify the limits of the model. From this ambitious goal, three main constitutive objectives arise.

First, to design a valid CFD setup to faithfully reproduce the real behaviour of a generic store carried on a military delta wing at transonic speeds. Along this part, different design methods are evaluated, searching for their benefits and drawbacks. Thereby, the final geometry, grid approach, and fluid flow solver is found. Chosen design solution must provide reliable results with an affordable computational cost. As part of this objective, a parametric study in terms of surface grid resolution is accomplished to determine how this parameter impacts on results' accuracy. Additionally, a comparison analysis against a viscous approach is performed.

Secondly, to validate the final CFD setup by comparing various simulations against published literature and experimental data. Achieved outcomes include force and moment coefficients and surface pressure distributions. This allows to determine the limits of the model and to validate its correct operation.

Finally, to theoretically define the fundaments to perform non-stationary store separation simulations. Within this part, main obstacles, conforming blocks, and interactions among the different elements of the simulation are described. It is worth mentioning, though, that accomplishing a CFD simulation of a store releasing from an aircraft requires of enormous computational resources. Currently, this is unaffordable for a personal computer; therefore, the simulation itself is out of the scope for this TFM.

When working with CFD tools, one must bear in mind that a particular approach may never work the best for all geometries, flight conditions, and all configurations. However, as it will be demonstrated throughout this report, the problem assessed during this TFM can be correctly suited by an inviscid approach with unstructured meshing. The efficiency of the proposed setup provides an acceptable level of accuracy with a significant savings in time, effort, and computational cost. The fact that this setup is successfully demonstrated at transonic speeds makes the technique an attractive tool not only for preliminary design but also for more sophisticated assessments.

Table of Contents

LIST OF TABLES

LIST OF FIGURES

List of Abbreviations

CAD	Computer-Aided Design
CFD	Computational Fluid Dynamics
FDM	Finite Differential Method
FEM	Finite Element Method
FVM	Finite Volume Method
ISA	International Standard Atmosphere
RANS	Reynolds-Averaged Navier-Stokes
TFM	Trabajo Fin de Máster
6-DOF	Six-degree of Freedom

1 INTRODUCTION

A good understanding of physics in carriage and release of external stores from an aircraft is of primary concern to military aircraft designers. The flow field encountered on stores in the vicinity of an aircraft is usually very complex due to mutual interferences. This situation sharpens when transonic fluid flows are considered. Furthermore, aerodynamic forces and moments acting on stores have not only an impact on mission's performance, but also a safety influence on the aircraft. Traditionally, designers have resorted to wind tunnel tests to assess these and other questions. However, recent years have seen an emergence of application of computational fluid dynamics (CFD) methods as a cheaper alternative since they provide accurate results when the appropriate models are applied.

The main aim of this Master's Thesis (TFM) is to validate an inviscid flow solution based on an unstructured grid approach over a stationary wing/pylon/store configuration. The efficiency of the proposed configuration is compared, when possible, against published literature and experimental data. Not only rigid body aerodynamics and but also mutual interference effects are explored to justify the limits of the model. Conclusions achieved along this report will ease to rigorously develop non-stationary store separation simulations in the future.

Within this chapter, the reader will be provided with the necessary context to understand the scope of the project and follow the rest of the report naturally. **Section 1.1** is intended to present the framework of the challenge carried out along this thesis, providing the reader with some background ideas to understand its main aim and technical complexity; **Section 1.2** summarises the main objectives undertaken during this TFM; **Section 1.3** seeks to introduce the main requirements and considerations that shape and constrain the whole design process; finally, **Section 1.4** illustrates the structure of the rest of the report.

1.1 Problem Statement

With the introduction and huge development of computational science and numerical algorithms, CFD methods have been stablished as an indispensable tool for both engineering design and scientific research. Due to the growth of computational resources, the complexity of problems that can be modelled has also increased. Aerodynamic simulation of moving-body problems, such as store separation or manoeuvring aircraft envelopes are important goals for CFD experts [1].

The aerodynamic behaviour of stores as they are released from aircraft is critical not only to the accurate arrival of the piece but also to the safety of the operation itself [2]. In the past, this question was assessed exclusively by flying tests. This approach was very time-consuming, often requiring years to certify a design solution. Likewise, it was expensive and occasionally led to the loss of an aircraft due to unexpected behaviour on the model being tested.

In the 1960s, wind tunnel tests were developed to tackle the aforementioned issues. These experiments have proven to be so valuable that they are still an essential resource for designers. However, wind tunnel tests are still expensive, have long lead times, and suffer from limited precision in certain situations. Additionally, as small-scale models must often be used, scaling problems might reduce accuracy on results. An example of a wind tunnel test setup is shown in **Figure 1.1**.

More recently, computational modelling and simulation have been implemented to reduce both certification cost and lead time, while increasing the margin of safety for subsequent flight tests. CFD approaches to simulating release events began with steady-state solutions combined with semi-empirical approaches [3]. Due to evolution of CFD techniques, nowadays unsteady full field simulations can be performed with or without viscous effects.

The challenge with using CFD techniques is to provide accurate results in timely manner. Computational cost is often high because fine grids and small-time steps may be required for accuracy purposes. Often, the costliest aspect of CFD, both in terms of time and money, is grid generation and assembly. This is especially notable for complex geometries.

Figure 1.1 Wind tunnel test setup [4]

Aerodynamic and physical parameters affect store separation simulations. These parameters are highly coupled and react with each other in a complex manner [5]. An accurate prediction of the trajectory of stores releasing from an aircraft involves a correct prediction of the flow field around them, the resulting forces and moments, and an accurate integration of the equations of motion. This translates into a coupling between the CFD solver and a six-degree of freedom (6-DOF) rigid body dynamics model [6]. Simulation errors in each of those models have an accumulative effect: any error in the calculated aerodynamic forces may imply a wrong attitude and position of the body, and vice-versa.

Moreover, store separation simulations need for a dynamic mesh approach. A dynamic mesh method allows to model flows where the domain's shape changes with time due to motion on the boundaries. Combined with the 6-DOF solver, a dynamic mesh allows the trajectory of a moving object to be determined by calculating the aerodynamic forces produced by the surrounding flow field. There are different dynamic mesh schemes depending on the features of the problem. A dynamic mesh method is always required when the motion itself is part of the solution (e.g., when a 6-DOF solver is required to solve the problem). This complicates the resolution since higher computational resources are required.

Computational cost is a critical factor that drives many of the assumptions made in the geometric model, grid generation, and fluid flow solver within a CFD model. In this context, one of the major assumptions of any fluid dynamics problem is whether to treat the flow field either as viscous or inviscid. From a CFD perspective, the inclusion of viscous effects means a significant increase in the size of the computational domain since the resolution of the boundary layer necessitates that the grid spacing normal to any solid surface be at least two orders of magnitude smaller than the equivalent inviscid grid.

The smaller spacing generally produces instability issues on the solution, causing the computational time to increase significantly when compared with inviscid solutions. Additionally, some grid methods become a more tedious task when boundary layers are considered. A wall function approximation allows to increase the grid spacing by about an order of magnitude, which might alleviate some of the mentioned issues [7].

Another key aspect when considering a viscous approach is turbulence modelling. Turbulence is caused by excessive kinetic energy in parts of a fluid flow, which overcomes the damping effect of fluid's viscosity. Consequently, highly random fluctuations appear on flow's properties. Since a deterministic approach is not possible, one has to resort to statistical tools. In order to make it approachable, Reynolds conceived the concept of average variables. Based on this, the variables of the problem can be expressed as a sum of mean and fluctuating part. Thus, the problem can be studied by the Reynolds-Averaged Navier-Stokes (RANS) equations. However, in order to make it a closed system, it is necessary to formulate one or several additional equations, usually known as turbulence models. These models can be classified into zero, one or two-equations models. Each of them has its own advantages and disadvantages and, therefore engineers must be trained to carefully apply the correct model to satisfy the requirements of the problem under consideration. This adds even more complexity when generating a design approach.

In terms of computational performance, a viscous approach requires the computation of additional quantities that, in addition to the larger computational domain, increases the computational cost as well as the memory required. It quickly becomes clear that an inviscid approach facilitates the design process, but the penalty in terms of fidelity of the simulation must be taken into consideration. It is also worth mentioning that while viscous methodologies are shaped by RANS equations, inviscid approaches are solved by Euler equations. Further insights regarding these two approaches are shown in **Chapter 2**.

Regarding grid generation techniques, they can be distinguished between structured and unstructured approaches. In the case of structured grids, both multi-blocked [1] and overlapping grid methods [6] have been successfully used to solve multi-body problems. The multi-blocked technique decomposes the flow field and the geometric configuration into a set of blocks. The union of these blocks fills the entire flow field without either holes or overlaps. While very efficient, multi-blocked gid generation requires considerable amount of time. For overlapping schemes such as Chimera, on the other hand, individual grids are generated for the components involved in the problem of interest, and they are overlaid with each other to form a complete mesh system. This makes the grid generation less arduous, and the grid movements can be independently modelled for the individual mesh. Nevertheless, subsequent flow solver tends to be more sophisticated because of a large amount of data processing is required for interpolation between parts of the grid. Therefore, these two approaches have a negative impact on computational cost.

To overcome this issue, unstructured grid methodologies have grown considerably in recent years due to their ability to produce quality grids around complex configurations with ease. The technology for generating grids and solving the fluid flow equations on unstructured grids has matured to the point that they are being applied for computing solutions over complex configurations. This flexibility makes the methodology a good candidate for the analysis of fluid flows around multi-body configurations, in both stationary and non-stationary problems. Additionally, unstructured meshes lend themselves very well to solution-adaptative mesh refinement and coarsening techniques, especially useful in capturing shock waves [8].

The critical aerodynamic behaviour of stores carried on or releasing from an aircraft occurs in the transonic speed regime. While numerical models in the subsonic and supersonic ranges rely on a range of assumptions and can be executed relatively fast, transonic models are very sensitive to geometry and are computationally demanding. This can be attributed to the complex shock structure that exists on stores at those transonic speeds. The flow field at that point is characterised by strong viscous-inviscid shock/boundary layer interactions and a large, separated flow region behind the store base. This is qualitatively shown in **Figure 1.2** for the case of an aerofoil. Transonic behaviour, together with the aerodynamic interferences among the different bodies, complicates the simulation.

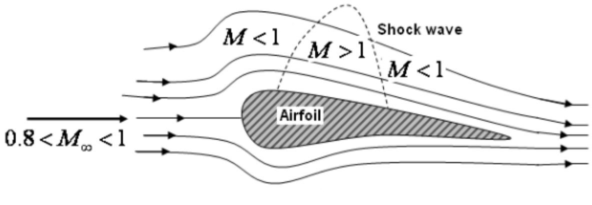

Figure 1.2 Transonic flow illustration [9]

Bearing all this in mind, building a CFD configuration to faithfully reproduce the real behaviour of a generic store releasing from an aircraft implies a huge technical complexity. Commercial CFD software packages such as ANSYS Fluent employ a fully converged steady state solution as initial condition to analyse subsequent non-stationary experiments. Therefore, a stationary wing/pylon/store configuration assessment is of due importance since it will provide valuable inferences to correctly develop non-stationary store separation simulations in the future.

Finally, validation in CFD is a rigorous requirement. The case of a generic finned store carried on a pylon beneath a delta wing has been experimentally studied in a campaign of wind tunnel tests [10], in which aerodynamic loads on the store and other aerodynamic properties were obtained. In this report, this resource is used to validate an inviscid flow solution based on an unstructured grid approach with the aim of economically predicting (in terms of computational cost) the store behaviour while it is carried on aircraft, but also capturing the transonic fluid flow phenomena. Achieved outcomes include, among other things, force and moment coefficients and surface pressure distributions. Subsequent conclusions will allow to develop non-stationary release simulations in the future. All the ideas exhibited during this section are expanded and discussed along this report.

1.2 Thesis Objectives

The main goal of this TFM is to validate an inviscid flow solution based on an unstructured grid approach over a generic finned store carried on a pylon beneath a delta wing, in stationary configuration. The efficiency of the proposed setup is compared, when possible, against experimental data. Both rigid body aerodynamics and mutual interference effects are explored to justify the limits of the model. Achieved conclusions will ease to rigorously develop non-stationary store separation simulations in the future. From this ambitious goal, three main constitutive objectives arise:

- To design and justify a valid CFD setup to faithfully reproduce the real behaviour of a generic store carried on a military delta wing at transonic speeds. During this part, different design methods are evaluated, searching for their benefits and drawbacks. Thereby, the final geometry, grid approach, and fluid flow solver is found. Chosen design solution must provide reliable results with an affordable computational cost. As part of this objective, a parametric study in terms of surface grid resolution is accomplished to determine how this parameter impacts on results' accuracy. This objective is tackled in **Chapter 3**.
- To validate the final CFD setup by comparing various simulations against published literature and experimental data. Achieved outcomes include, among other things, force and moment coefficients and surface pressure distributions. This allows to determine the limits of the model and to validate its correct operation. This objective is dealt in **Chapter 4**.
- To theoretically define the fundaments to perform non-stationary store separation simulations. Within this part, main obstacles, conforming blocks, and interactions among the different elements of the simulation are described. This objective is reached in **Chapter 5**. It is worth mentioning, though, that accomplishing a CFD simulation of a store releasing from an aircraft requires of enormous computational resources. Currently, this is unaffordable for a personal computer; therefore, the simulation itself is out of the scope for this TFM.

1.3 Main Requirements and Considerations

Having reached this point it is of due significance to summarise the main requirements, constraints, and hypotheses that shape this report, as they have an impact on the overall design process. Requirements affect the design enclosure in terms of functional and performance conditions, and they will allocate the high-level interfaces amongst other design elements. These constraints are described in detail below and their compliance is justified throughout the rest of this report.

- **R.01**: Final CFD setup shall be validated. Hence, selected geometric model shall allow to compare its simulation results against experimental data.

Wind tunnel experiments for a generic pylon/store geometric configuration attached to a clipped delta wing were conducted at the Arnold Engineering Development Centre [10]. *Available results from these studies include trajectory information (in release configuration) and surface pressure distributions at carriage position. The computational geometry used along this report matches the experimental model with the exception of the physical model being 1/20 scale. A complete description of the geometry is shown in* ***Chapter 3****.*

- **R.02**: Different configurations of the selected geometric model shall be assessed to validate the final CFD setup.

  First, the store alone over a range of angles of attack is considered. Then, the full store/wing/pylon configuration is evaluated at three different store positions. These positions are representative of the carriage position (baseline), an intermediate position when the store is released (near), and the farthest position when the store is released (far). The latter two positions are defined by their translations and rotations with respect to the store centre of gravity while in carriage position. Further details are shown in ***Chapter 3****.*

- **R.03**: Each configuration defined in **R.02** shall be simulated under steady-state fluid flow conditions.

  This assumption simplifies problem's formulation in terms of its conforming blocks, and it alleviates the expected computational cost. As mentioned before, the release case implies a coupling between the CFD solver and a 6-DOF rigid body dynamics model, and its resolution over a significant time spam is unaffordable for a personal computer. Therefore, only the carriage configuration is assessed during this report.

- **R.04**: All simulations are realised to a flight altitude of $11600\ m$, where the corresponding ambient pressure is $20588\ Pa$, the ambient temperature is $216.65\ K$, and the air density is $0.3310\ kg/m^3$.

  These conditions are the same as those used during the wind tunnel tests. The International Standard Atmosphere (ISA) model (described in ***Appendix A****) has been employed to obtain ambient fluid conditions from flight altitude.*

- **R.05**: Simulations shall be carried out at transonic speeds to assess shock wave regions.

  Two flight speeds (M = 0.95 and M = 1.2) are considered since they represent the current flight envelope of a military aircraft. Moreover, these speeds allow to find regions where transonic behaviour appears. This consideration adds extra complexity but allow us to validate the model that has been designed.

- **R.06**: Simulations shall run until the minimum convergence conditions are met.

  There are not universal metrics for judging convergence. Residual definitions that are useful for one class of problem are sometimes misleading for others. Therefore, it is a good idea to judge convergence not only by examining residual levels, but also by monitoring relevant quantities such as force and moment coefficients. During this report, we consider that convergence is met when either two of the following conditions are met: residuals decrease to 1e-5 for all equations except for the energy, for which criterion is 1e-7; both residuals and force and moment coefficients converge to a stable value for several iterations (50 or more iterations). Further discussion about this topic is found in ***Chapter 4****.*

- **R.07**: Final CFD setup shall be designed based on inviscid fluid flow features.

  Fluid flow is considered as compressible, and it is described by Euler equations. Further details about this requirement are shown in ***Chapter 3****.*

- **R.08**: Final CFD setup shall be designed based on unstructured grid generation techniques. Additionally, created grid shall fulfil the minimum quality standards.

  This requirement guarantees to provide reliable results. Further details about this requisite are described in ***Chapter 3****.*

- **R.09**: Final CFD setup shall be compatible with non-stationary release simulations requirements.

  We must recall that the third objective within this TFM is to stablish the fundaments to correctly perform non-stationary release simulations. Therefore, final setup must be designed consistent with release experiment requirements.

1.4 Structure of the Report

This section illustrates how the rest of the report is organised. **Chapter 2** first provides the necessary background to understand how challenging is to faithfully reproduce, by means of CFD simulations, the real behaviour of a generic store carried on a military delta wing at transonic speeds. This enables to identify main constraints, design approaches, and technical limits when using CFD tools. Among those ideas, the most significant CFD approaches (e.g., viscous vs inviscid approaches; structured vs unstructured grid approaches; pressure vs density-based algorithms; etc.) are recognised in published literature. **Section 2.1** deals with these ideas. **Section 2.2** describes all the analysis tools applied throughout this report. First, it is worth mentioning how ANSYS Fluent works. Then, the main features and limitations of the published experimental case used during this report are explained. This allows to understand and justify subsequent discrepancies found on some results. **Chapter 2** concludes with **Section 2.3**, where some principles of Aerodynamics are introduced as they are necessary to understand some complex ideas raised in **Chapter 3**, where the final design approach is explained.

Along **Chapter 3**, the final CFD setup is obtained. From geometry to grid generation and fluid flow solver, each of these blocks are described to show how important they are to accomplish a good modelling. Further Aerodynamics principles are introduced to justify each design decision. During this chapter, different design methods are evaluated, searching for their benefits and drawbacks. Thereby, the final geometry, grid approach, and fluid flow solver is found. Chosen design solution must provide reliable results with an affordable computational cost. As part of this objective, a parametric study in terms of surface grid resolution is accomplished to determine how this parameter impacts on results' accuracy and computational cost.

Chapter 4 summarises the main results and discussions raised during this work. When possible, CFD results are assessed against experimental data to validate the design approach. Likewise, all the assumptions previously considered during this work are reviewed. This will allow us to justify their consistence and discuss their limits.

Then, **Chapter 5** reviews overall conclusions and recommended future work. Additionally, the fundaments to perform non-stationary release simulations are theoretically defined to show the reader their main complications. Within this part, main obstacles, conforming blocks, and interactions among the different elements of the simulation are described. Finally, this report is enhanced by several appendices.

2 STATE OF THE ART

This chapter provides the necessary background to understand how challenging is to faithfully reproduce, by means of CFD simulations, the real behaviour of a generic store carried on a military delta wing at transonic speeds. **Section 2.1** deals with the main constraints, design approaches, and technical limits recognised in published literature when using CFD tools to solve similar conditions. **Section 2.2** describes all the different analysis tools applied throughout this report. Finally, **Section 2.3**, aims at describing some principles of Aerodynamics as they are necessary to understand some complex ideas raised in subsequent chapters.

2.1 Literature Review

The prediction of the separation trajectory of an external store carried on a military aircraft wing under transonic speeds is an important mission in the aerodynamic design area in order to define the safe operational and release envelopes. Its assessment is complex: the store flow field depends upon its flight conditions (e.g., attitude and velocity); the presence of the store near the wing/pylon structure causes aerodynamic interferences that must be accounted for; finally, those perturbation effects vary with distance from the parent structure. In the past, this question was assessed exclusively by flying tests. This approach was very time-consuming, often requiring years to certify a design solution. Likewise, it was expensive and occasionally led to the loss of an aircraft due to unexpected behaviour on the model being tested. For this reason, defining safe store carriage and separation envelopes is a question that has received considerable attention historically.

In the 1960s, wind tunnel tests were developed to overcome some of the aforementioned issues. These experiments have proven to be so valuable that they are still an essential resource for designers. However, wind tunnel tests are still expensive, have long lead times, and suffer from limited precision in certain situations. Past attempts to mitigate these obstacles tried to generalise store behaviour data from one store to another based on the similarities in geometry and inertial characteristics of various stores. As a result, many stores were cleared for flight by analogy.

In this context, Meyer, R. et al. [11] developed an influence function method for predicting the forces and moments on a store during separation based on previous wind tunnel data for another store in the same flow field conditions. This technique used either measured or theoretically determined parent aircraft flow field data and estimated nose, mid-section, and tail-section force and moment contributions as a function of their respective local angle of attack. Predicted aerodynamic characteristics for stores during separation based on this method demonstrated good correlation with supersonic experimental data. It is worth mentioning that semi-empirical tools such as Datcom employ some of these considerations when generating their outcomes.

However, influence function methods fall far behind the accuracy that actual CFD techniques can provide, so that new techniques appeared. Covert, E. [2] studied the trajectory of external stores ejected from aircraft with the goal of developing simple safe operation criteria. As a result, it was found that the initial velocity and acceleration provide a means of defining a sufficient condition for safe separation. In particular, if both velocity and acceleration are sufficiently large in the pitch plane and small enough in the lateral plane, the store would have a trajectory that allows it to separate safely. The obtained condition, based on a constant force model, is simple enough to be easily programmed. Additionally, since the found condition is only sufficient, any store that fails to satisfy this requirement entails a further detailed study to determine whether its separation is safe or not.

In the last few years, the development of CFD techniques has successfully contributed to the prediction of the flow field through the store carriage and separation problem. CFD approaches to simulating release events began with steady-state solutions combined with semi-empirical approaches. Cenko, A. et al. [3], for example, used a panel method, called PAN AIR, to analyse complex flow phenomena associated with aircraft/weapons carriage and mutual interference during separation. This method is intended to deal with a variety of boundary value problems in steady subsonic or supersonic inviscid flows, by solving the classic Prandtl-Glauert equation[1] for linearised compressible flows. To achieve that, the configuration is represented by a distribution of source and doublet singularities. Consequently, this method is able to analyse a huge variety of setups such as individual aircraft and weapon configurations, carriage configurations, and mutual interference effects during store separation. However, results were not accurate enough to be useful at transonic Mach numbers. To improve this issue, Madson, M. et al. [12] developed TranAir, a tool able to solve the full potential equations for subsonic, transonic, and supersonic flows about arbitrary configurations based on the same surface panelling used in PAN AIR.

Due to evolution of CFD techniques, nowadays unsteady full field simulations can be performed. The most accurate computational tool for determining the flow field on complex configurations would be a solution to the time-dependent full Navier-Stokes equations [13]. For most configurations of interest, such solution is beyond the estate of the art of computers' performance and is usually attempted only for simple shapes or for a small region of the flow field. Hence, some simplifications must be considered.

Within this context, one of the major assumptions of any fluid dynamics problem is whether to treat the flow field either as viscous or inviscid. Westmoreland, S. [7] discussed the choice of fluid dynamic governing equations, either the inviscid Euler equations or the viscous Navier-Stokes equations, on a store trajectory. Differences between these two CFD simulations were observed in the carriage loads, though an analysis showed that the overall load distribution compared very well between the two solutions and pointed to specific locations where the differences occurred (it was found that the differences occurred in areas where viscous effects were dominant, i.e., where flow separation and boundary layer growth were prevalent). Although aerodynamic loads differences were observed in carriage, the ejector forces initially dominate the dynamics of the separation. Thus, trajectory comparisons showed little variation between the two solutions, and both compared well with flight test data. Additionally, viscous simulations took almost 6 times more of computational cost when compared to inviscid models. These conclusions justify that almost all the published literature employ an inviscid approach to simulate similar conditions.

Another of the most expensive aspects of CFD, both in terms of time and money, is grid generation and assembly. Grids can be distinguished between structured and unstructured approaches. Regarding structured grids, both multi-blocked and overlapping grid methods have been successfully used to solve multi-body problems. Arabshahi, A. et al. [1] developed a multi-blocked approach to solve the three-dimensional unsteady Euler equations about a wing/pylon/store configuration. The multi-blocked technique decomposes both the flow field and the configuration into a set of blocks. The union of these blocks fills the entire flow field without either holes or overlaps. While very efficient, multi-blocked gid generation requires considerable amount of time. Koomullil, R et al. [6] and MacLucas, D. et al. [14], on the other hand, used an overlapping framework to simulate flow past bodies in relative motion. This scheme generates individual grids for each of the components involved in the problem of interest, and they are overlaid with each other to form a complete mesh system. This makes the grid generation less arduous, and the grid movements can be independently modelled for the individual mesh. Nevertheless, subsequent flow solver tends to be more sophisticated because of a large amount of data processing is required for interpolation between parts of the grid.

To overcome this issue, unstructured grid methodologies have grown considerably in recent years due to their ability to produce quality grids around complex configurations with ease. Most of the found literature employ this scheme to solve both the carriage and store release problems.

Regarding the carriage configuration, Parikh, P et al. [15] validated a solution package consisted of an advancing front tetrahedral unstructured grid generator and an upwind, cell-centred, finite volume Euler solver using experimental data. A considerable reduction in grid generation times were found in comparison with structured approaches. For all cases under consideration, a very close agreement with the experimental data

---

[1] $\beta^2\phi_{xx} + \phi_{yy} + \phi_{zz} = 0$, where $\beta^2 = 1 - M_\infty^2$ is known as the Prandtl-Glauert factor.

was obtained.

On the other hand, Panagiotopoulos, E. et al. [16] and Snyder, D. et al. [8] employed a dynamic unstructured tetrahedral mesh approach to simulate a safe store separation event from underneath a delta wing under transonic conditions. The model is combined with a spring-based smoothing and local remeshing and an implicit, second order upwind Euler solver. A 6-DOF routine using a fourth-order multi-point time integration scheme is coupled with the flow solver to update the store trajectory information. Results were validated against experimental data, showing that CFD with unstructured dynamic meshing can be an effective tool for modelling transonic store separation envelopes.

Finally, parallel computing offers a very effective way to improve productivity in CFD analyses. Prewitt, N. et al. [17] reviewed recent progress made in parallel computing applied to store separation problems. This method makes sense in overlapping, structured grids as they accept the use of efficient flow solvers and allows for grid motion without stretching or re-gridding. Results showed that parallel computing techniques allow the CPU time to be reduced from several days on a single processor computer to about hours on a parallel computer.

This section has intended to provide a brief description of the state of the art regarding CFD approaches to solve the problem of a generic finned store carried beneath a military wing. Some other topics such as turbulence models within viscous approaches are described in detail in **Section 2.3**.

2.2 Analysis Tools

This section is focused on describing the different analysis tools used throughout this report. **Subsection 2.1.1** aims at describing the fundamentals of ANSYS Fluent. This commercial software package has been used to build all the CFD simulations developed along this work. Then, **Subsection 2.2.2** briefly describes a campaign of published wind tunnel tests used to experimentally study a generic finned store carried on and released from a pylon beneath a delta wing. The final CFD setup is validated in **Chapter 4** against both experimental data and published literature.

2.2.1 ANSYS Fluent

Historically, when analysing the behaviour of a fluid, the use of specific facilities such as wind tunnels has always been the main option for aerodynamicists, where the main aim was to reproduce as faithfully as possible the conditions to be studied. This entails some drawbacks such as the cost, not only of the experiments themselves, but also of the facilities. Also, the rigidity when facing possible changes in the experiments is another important matter, since the models must be manufactured, with the time and difficulty that this entails. Therefore, the use of computational methods is an option that has been gaining weight over time, since it partially solves the problems that have been pointed out.

Although it solves these problems, it also presents others, such as the difficulty involved in the validation of the results, as this approach employs mathematical models and discretisation procedures to represent physical phenomena. Additionally, the cost in terms of time must be accounted when very detailed analyses are carried out. These aspects will be discussed later, but it is convenient to describe the bases of CFD methods, in particular those for ANSYS Fluent.

There are three different methods for computationally analysing fluids, each of them with their own benefits and inconveniences. These are Finite Element Methods (FEM), Finite Differential Methods (FDM) and Finite Volume Methods (TVM). Along this work, ANSYS Fluent is employed. This software works with the FVM, the most employed method for CFD analyses.

The FVM is a technique for assessing partial differential equations in the form of algebraic expressions. In the FVM, volume integrals in a partial differential equation that contain a divergence term are converted to surface integrals, using the divergence theorem. These terms are then evaluated as fluxes at the surfaces of each finite volume. Because the flux entering a given volume is identical to that leaving the adjacent volume, these methods are considered as conservative. Another advantage is that it is easily formulated to allow for unstructured meshes. This report is not intended at describing this method in detail; therefore, any reader interested in this topic can refer to [18].

In this context, ANSYS Fluent provides modelling capabilities for a wide range of incompressible and compressible, laminar and turbulent fluid flow problems. Steady-state or transient analyses can be performed with ease. In this software, a broad range of mathematical models for transport phenomena (such as heat transfer or chemical reactions) are combined with the ability to model complex geometries. Examples of admissible applications include laminar non-Newtonian flows; external aerodynamics; and flow through compressors. Additionally, accurate turbulence models are built in ANSYS Fluent. Those turbulence models have a broad range of applicability, and they include the effects of compressibility. Additionally, special care has been devoted to addressing issues of near-wall accuracy by using extended wall functions.

2.2.2 Experimental Data

Validation in CFD is a rigorous requirement. The case of a generic finned store carried on a pylon beneath a delta wing has been experimentally studied in a campaign of wind tunnel tests built by the Arnold Engineering Development Centre [10]. Test objectives were to obtain pressure distribution and flow visualisation data from geometrically simple wing and store shapes under mutual interference conditions with the store both at its carriage position and at selected points along a realistic store separation trajectory. Accomplishment of these objectives required using a Captative Trajectory Support System and testing with both balance-mounted and pressure-instrumented stores.

Test article configurations consisted of a generic finned store shape and a clipped delta wing (with NACA 64A010 aerofoil section) with a 45-degree leading edge sweep angle and a detachable pylon. The wing and pylon combination contained 146 pressure orifices for measuring pressure distributions at chordwise row locations near the store carriage position. In particular, wing pressures were required for both upper and lower surface orifices at locations inboard, outboard, and in the plane of the pylon. The pressure model of the store included 228 pressure orifices arranged in 5 longitudinal rows on the body and 2 chordwise rows on each of the 4 fins. The fin design incorporated use of the NACA 0008 aerofoils section and a 60-deg leading edge sweep angle. Boundary-layer transition strips were not used on either the wing or the store models, therefore a realistic turbulent boundary layer was not obtained. **Figure 2.1** shows the pressure-instrumented store configuration. A detailed description of the geometry can be found in both **Section 3.1** and **Appendix B**, as the final CFD setup was built using the same geometric configuration.

Pressure and flow visualisation data were acquired for wing and store at several angles of attack. Test conditions included Mach numbers of 0.95 and 1.2. Those test conditions were held constant while varying the store or the wing and store model attitudes. Further information about instrumentation setup, test environment, store physical properties, ejector force data for the separation trajectories, and data acquisition procedures can be found in [10].

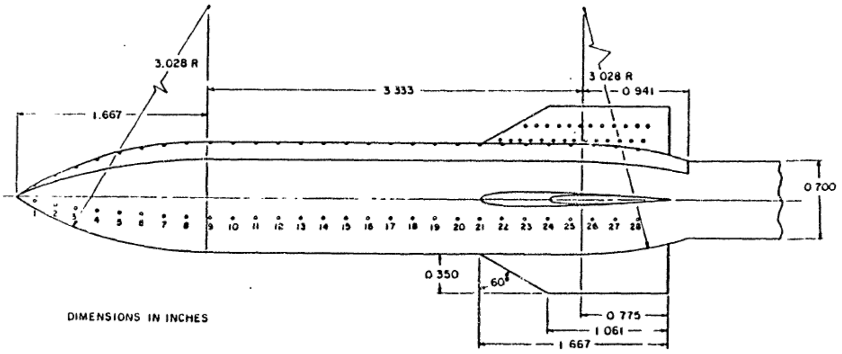

Figure 2.1 Pressure-Instrumented store details [10]

It must be noticed that experimental trajectory propagations during those tests were computed based on quasi-steady assumptions, therefore it is not a time-accurate computation, and some differences may arise with respect to a truly non-stationary release CFD experiment. However, this feature will allow us to numerically simulate intermediate positions of the store relative to the wing/pylon structure and compare those CFD results against experimental data.

2.3 Principles of Aerodynamics

Before focusing on describing the designed methodology, it is of due importance to have a brief overview of some principles of Aerodynamics that are necessary to understand the remaining chapters of this report. Those concepts are illustrated in the following subsections.

2.3.1 Reference Frames, Orientation Angles, and Aerodynamic Coefficients

Along this work, we are mainly focused on studying aerodynamic forces and moments acting on the store in several configurations. Consequently, it is necessary to describe how to obtain those parameters correctly, being always consistent with experimental data.

Two main reference frames were used during this work. **Figure 2.2** shows the global reference frame $Oxyz$ orientation. The origin O is fixed at the store centre of gravity while in carriage; x-axis runs from the tail to nose of the store; y-axis points away from the aircraft; and z-axis points downward along the direction of the gravity, all of that forming a right-handed coordinate system.

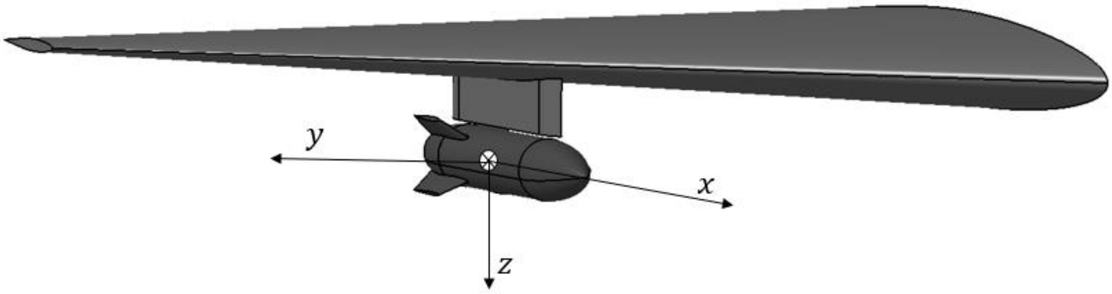

Figure 2.2 Global reference frame orientation

Aerodynamic force and moment coefficients are obtained in terms of the body reference frame $Ox_by_bz_b$, which is shown in **Figure 2.3**. The origin O is located at the store centre of gravity; x_b-axis runs from the tail to nose of the store, parallel to the store longitudinal axis; y_b-axis is perpendicular to x_b and z_b directions, positive to the right looking upstream when the store is at zero yaw and roll angles; z_b-axis is perpendicular to the x_b direction and parallel to the aircraft plane of symmetry when the store and aircraft are at zero yaw and roll angles, positive downward when the store is at zero pitch and roll angles.

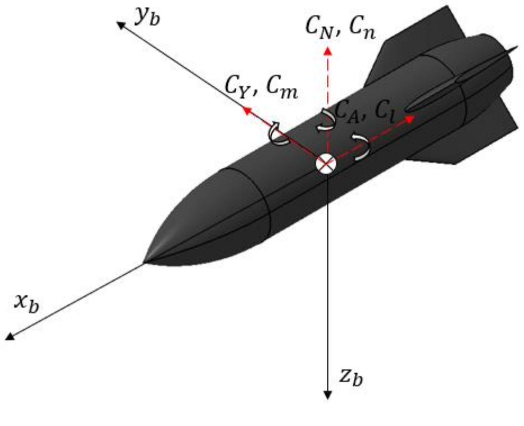

Figure 2.3 Body reference frame orientation

The orientation of the store along its detachment trajectory is defined by the orientation of the body reference frame with respect to the global reference frame by three Euler's angles:

- Yaw angle, ψ: angle between the projection of the store longitudinal axis in the x-y plane and the x axis, positive for the nose to the right.
- Pitch angle, θ: angle between the store longitudinal axis and its projection in the local x-y plane, positive when the store nose is raised.
- Roll angle, ϕ: angle between the store lateral axis y_b and the intersection of the y_b-z_b plane and the local x-y plane, positive for the clockwise rotation when looking upstream.

Store's force and moment coefficients are calculated from aerodynamic forces and moments, respectively. Those coefficients, illustrated in **Figure 2.3**, can be computed as follow:

$$(-C_A, C_Y, -C_N) = \frac{F^A_{x_b, y_b, z_b}}{\frac{1}{2}\rho_\infty U_\infty^2 S_{ref}} \tag{2.1}$$

$$(C_l, C_m, C_n) = \frac{M^A_{x_b, y_b, z_b}}{\frac{1}{2}\rho_\infty U_\infty^2 S_{ref} D} \tag{2.2}$$

where $\boldsymbol{F}^A$ is the total aerodynamic force; $\boldsymbol{M}^A$ is the total aerodynamic moment (with respect to the store's centre of gravity); ρ_∞ is the density of the free stream; U_∞ is the velocity of the free stream; S_{ref} is the reference area; finally, D is the reference length. During this report, S_{ref} is the store's frontal area, whereas D is the store's diameter (more information about S_{ref} and D can be found in **Section 3.1**). Based on those previous considerations, store's aerodynamic force and moment coefficients can be defined as follow:

- Axial force coefficient, C_A: positive in the negative x_b.
- Side force coefficient, C_Y: positive in the positive y_b.
- Normal force coefficient, C_N: positive in the negative z_b.
- Rolling moment coefficient, C_l: positive in the positive x_b.
- Pitching moment coefficient, C_m: positive in the positive y_b.
- Yawing moment coefficient, C_n: positive in the positive z_b.

Previous considerations allow to obtain force and moment coefficients, by means of CFD simulations, consistent with experimental data.

Finally, the last aerodynamic parameter that will be introduced is the pressure coefficient C_p, which is used to describe relative pressures in any flow field. In this case, it will be used to characterise the pressure distribution along the upper and lower surface of a particular body of the geometry; furthermore, this coefficient allows to identify shock and expansion wave locations. Its definition is presented below:

$$C_p = \frac{p - p_\infty}{\frac{1}{2}\rho_\infty U_\infty^2} \tag{2.3}$$

where p is the static pressure at the point under consideration and p_∞ is the static pressure of the free stream.

2.3.2 Compressibility Effects

Compressibility effects are encountered in gas flows at high velocity and/or in which there are large pressure changes. Particularly, when the flow velocity approaches or exceeds the speed of sound ($M \sim 1$), the variation of the gas density with pressure has a significant impact on the flow velocity, pressure, and temperature. Under these conditions, the flow may contain shock and expansion waves that can impact in the flow pattern significantly. Compressible flows create a unique set of flow physics for which one must be aware of the special input requirements and solution techniques, especially when dealing with CFD methods. As an example of that, the static pressure and temperature in the flow vary with respect to the Mach number. **Chapter 3** deals with all the particularities that one must be aware when simulating compressible flows in ANSYS Fluent.

2.3.3 Shock Waves

When a body moves at subsonic speeds ($M < 1$), the air ahead of it is warned of the body's coming by a pressure change transmitted at the speed of sound. Because of this warning, the air moves aside before the body arrives and is prepared to let it pass easily.

But as the moving body reaches the local speed of sound ($M \sim 1$) and catches up to its own pressure waves, the air ahead of it receives no warming of the body's approach. Hence, the moving body makes its way through the air by creating a shock wave. An example of that is shown in **Figure 2.4**.

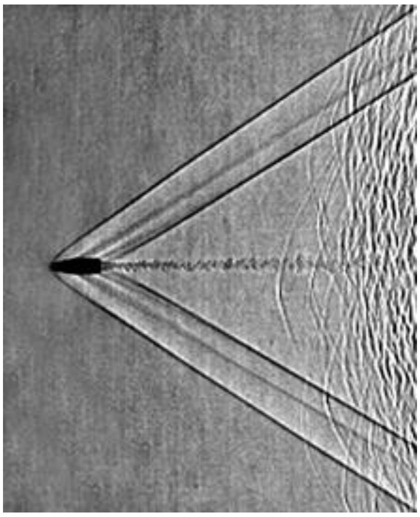

Figure 2.4 Shadowgram of shock waves from a supersonic bullet [19]

As the air flows through the shock wave, its pressure, density, and temperature abruptly increase (as a consequence of a sharp decrease in flow's velocity). One of the principal effects of a shock wave is the formation of a dense high-pressure region immediately behind the wave. The instability of the high-pressure region, and the fact that part of the kinetic energy of the air stream is converted to heat as it flows through the wave, translate into a drag rising. This component is better known as wave drag. Finally, if the shock wave is strong enough, the boundary layer may not have sufficient kinetic energy, so that airflow separation might occur.

When airflow separation occurs, a turbulent wake behind the moving body appears, causing the resulting aerodynamic forces and moment to oscillate. Notice that this phenomenon was found in some of the CFD simulations undertaken during this work, where some of the force and moment coefficients oscillated throughout the numerical simulations. Turbulent wake can also have an impact on the pressure coefficient distribution along the body surface. Consequently, the final position of the centre of pressure and its resulting pitching moment may also oscillate. A more detailed discussion is shown in **Chapter 4**.

2.3.4 Inviscid Model. Euler Equations

As discussed in **Chapter 1**, one of the major assumptions of any fluid dynamics problem is whether to treat the flow field either as viscous or inviscid. Inviscid flow analyses neglect the effect of viscosity on the flow and are appropriate for high-Reynolds-number applications where the inertial forces tend to dominate viscous forces. Inviscid flows are solved by the Euler equations, a simplification of the full Navier-Stokes equations. The mass conservation equation is the same as for a laminar flow, but the momentum and energy conservation equations are reduced due to the absence of molecular diffusion:

$$\frac{\partial \rho}{\partial t} + \nabla \cdot (\rho \boldsymbol{v}) = 0 \qquad \textbf{(2.4)}$$

$$\frac{\partial}{\partial t}(\rho \boldsymbol{v}) + \nabla \cdot (\rho \boldsymbol{v}\boldsymbol{v}) = -\nabla p \qquad \textbf{(2.5)}$$

$$\frac{\partial}{\partial t}(\rho E) + \nabla \cdot \big(\boldsymbol{v}(\rho E + p)\big) = 0 \qquad \textbf{(2.6)}$$

where E is the total energy per unit volume. Equations **(2.4) - (2.6)**, together with a suitable constitutive equation (during this work, the ideal gas model is employed), form a quasilinear hyperbolic system of equations. **Chapter 3** explains how to numerically solve it for our particular problem. That chapter also underlines the ideal gas law definition.

2.3.5 Viscous Model. RANS Equations

Even though the main aim of this TFM is to design an inviscid fluid flow solution over a generic wing/pylon/store configuration, it is worth mentioning how a viscous approach should be handled. Notice that **Chapter 4** includes some results for a viscous simulation as a way to validate the designed inviscid approach.

The first concept that must be mentioned is that due to the complexity of viscous flows, a deterministic approach cannot be reachable. Reynolds understood this issue, and in order to make it approachable, conceived the concept of average variables. Based on this, the solution variables in the instantaneous Navier-Stokes equations can be expressed as a sum of mean (time-averaged) and fluctuating part. For velocity components, for example:

$$\boldsymbol{u}(\boldsymbol{x},t) = \overline{\boldsymbol{u}}(\boldsymbol{x},t) + \boldsymbol{u}'(\boldsymbol{x},t) \qquad \textbf{(2.7)}$$

where $\overline{\boldsymbol{u}}$ is the mean velocity; $\boldsymbol{u}'$ is the fluctuating part; and $\boldsymbol{x}$ is the position vector. Following the definition of the time averaging, the subsequent expression is obtained:

$$\overline{\boldsymbol{u}}(\boldsymbol{x},t) = \lim_{T\to\infty} \frac{1}{t+T} \int_{t_0}^{t_0+T} \boldsymbol{u}(\boldsymbol{x},t)dt \qquad \textbf{(2.8)}$$

which means that the value taken by the velocity at a fixed place in space over a time span that is large enough is in fact the average term of this velocity.

For compressible flows, the fluctuation of other quantities such as density and temperature must be taken into consideration, along with the energy equation. This increases the complexity of the system. If the Reynolds time averaging methodology is used, the final form of the system presents multiple correlations between the different magnitudes, making more difficult the closure of the problem. Consequently, Favre introduced the density-weighted time-average operator. This operator applied to velocity represents mass-averaged values:

$$\widetilde{\boldsymbol{u}}(\boldsymbol{x},t)=\frac{1}{\bar{\rho}}\lim_{T\to\infty}\frac{1}{t+T}\int_{t_0}^{t_0+T}\rho(\boldsymbol{x},\tau)\boldsymbol{u}(\boldsymbol{x},\tau)d\tau \qquad \textbf{(2.9)}$$

being $\bar{\rho}$ the time-averaged density.

Substituting expressions of this form for the flow variables into the instantaneous continuity and momentum equations[2] and taking a time average, yields the Reynolds-averaged Navier-Stokes (RANS) equations:

$$\frac{\partial\rho}{\partial t}+\frac{\partial}{\partial x_i}(\rho u_i)=0 \qquad \textbf{(2.10)}$$

$$\frac{\partial}{\partial t}(\rho u_i)+\frac{\partial}{\partial x_j}(\rho u_i u_j)=-\frac{\partial p}{\partial x_i}+\frac{\partial}{\partial x_j}\left[\mu\left(\frac{\partial u_i}{\partial x_j}+\frac{\partial u_j}{\partial x_i}-\frac{2}{3}\delta_{ij}\frac{\partial u_l}{\partial x_l}\right)\right]+\frac{\partial}{\partial x_j}\left(-\rho\overline{u_i' u_j'}\right) \qquad \textbf{(2.11)}$$

where $i=x,y,z$. Note that each time-averaged magnitude $\bar{\phi}$ has been substituted by ϕ to simplify the notation. This system of equations has the same form as the instantaneous Navier-Stokes equations, with the velocities and other solution variables now representing time-averaged values. Additional terms now appear that represent the effects of turbulence. These are the Reynolds stresses, $-\rho\overline{u_i' u_j'}$, that must be modelled in order to close the system. Closing the system is where the different turbulence models take part.

For compressible flows, equations **(2.10)** – **(2.11)** are interpreted as Favre-averaged Navier-Stokes equations, with the velocities representing mass-averaged values.

2.3.5.1 Turbulence Models

As explained before, Favre version of Navier-Stokes equations is not a closed problem. Thus, in other to close the system, it is necessary to formulate one or several additional equations, which are usually known as turbulence models. These models can be classified into zero, one or two-equations models. It is important to note that zero-equation models owe their name to the fact that only algebraic equations are involved. Prior to speak about the recommended model for the problem dealt during this report, a brief description of the different benefits and disadvantages of each model is made, in order to understand better the problem [19].

For zero-equation models, the main advantage is the simplicity, allowing to analyse turbulence with little computational effort, being relatively simple to implement in terms of coding. However, they have important limitations when trying to analyse complicated phenomena such as shock boundary layer interactions and separated flows. Other problem that they present is that they are not local, which means that the equation at one point depends upon the solution obtained from other points. Hence, these models will not perform properly with unstructured grids. Therefore, they are commonly used for simple problems.

Two-equations models are more reliable when analysing complex phenomena, however they involve higher computational effort, requiring finer grids near the walls and being more problematic in terms of convergence. Also, they can present some difficulties when setting values for the free stream conditions.

One-equation models generally present better results in terms of computational effort than the two-equations models. They are also able to give satisfactory predictions for boundary layers in pressure gradients and are

---

[2] A similar analysis can be done for the energy equation, though it is not shown for sake of brevity.

local (unlike the zero-equation models), which make them compatible with any type of grid. They can also use trivial values for the turbulence variables at the free stream, unlike the two-equations models. Thus, the model used during this work will be a one-equation model, in particular the Spalart-Allmaras model.

Focusing in the Spalart-Allmaras model, it solves a modelled transport equation for the kinematic eddy viscosity. The Spalart-Allmaras model was designed specifically for aerospace applications involving wall-bounded flows and has been shown to give good results for boundary layers subjected to adverse pressure gradients. Also, as it will be seen in **Chapter 3**, this turbulence model has an enhanced wall treatment which allows the application of the model independent of the near wall y^+ resolution, alleviating grid generation and its subsequent computational cost. The reader interested in the mathematical formulation behind Spalart-Allmaras formulation, applied to ANSYS Fluent resolutions, can refer to [20].

2.3.5.2 Boundary Layer

Finally, a brief explanation about boundary layer theory will allow to understand some conclusions and design approaches obtained in **Chapter 3**. In fluid mechanics, a boundary layer is the thin layer of the fluid in the immediate vicinity of a surface formed by the fluid flowing along the surface. Fluid's interaction with the wall induces a no-slip boundary condition (i.e., zero velocity at the wall). Then, the flow velocity monotonically increases above the surface until it reaches free stream conditions. Therefore, the thin layer consisting of fluid whose velocity has not yet returned to the free stream velocity is called the velocity boundary layer. On aerodynamics, this is the region of the flow where viscous forces distort the surrounding non-viscous flow.

The thickness of the velocity boundary layer, δ_v, is a function of the Reynolds number, $\delta_v \sim 1/\sqrt{Re}$. There are two different types of boundary layer flows: laminar and turbulent [21]. **Figure 2.5** shows the common evolution of a boundary layer along a generic surface. Notice that it will be necessary to approximately compute the thickness of the boundary layer for our problem in order to correctly design the inflation layers in ANSYS Mesh Application.

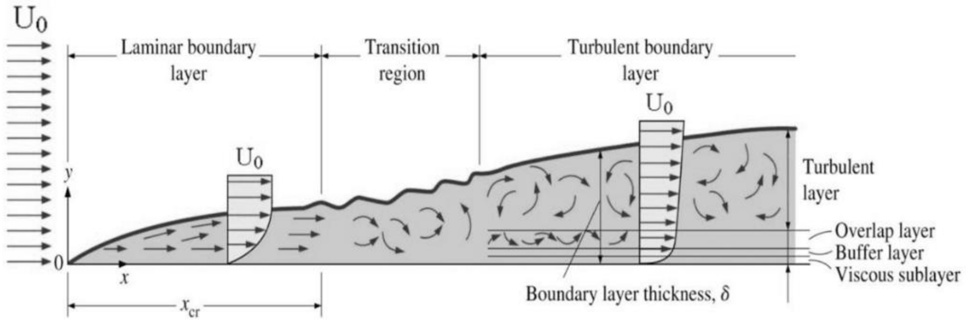

Figure 2.5 Boundary layer structure [23]

3 DESIGN METHODOLOGY

Along this chapter, the final CFD setup is developed. From geometry to grid generation and fluid flow solver, each of these blocks are described to show the reader how important they are to achieve a good modelling. As part of this objective, several design approaches are evaluated, searching for their benefits and drawbacks. Within this framework, further Aerodynamics principles would be introduced to justify each design decision. Thereby, the final geometry, grid approach, and fluid flow solver is found. **Section 3.1** summarises all the geometric configurations to be simulated. This also includes the enclosure generation process. Notice that the former is a crucial component within the geometry setup, particularly when transonic fluid flows are considered. **Section 3.2** tackles the grid generation process and summarises the chosen approach. **Section 3.3** discusses the main characteristics of the fluid flow solver, which is used to solve the governing fluid-dynamic equations over the control volume.

It should be remembered that the final design setup ought to provide reliable results with an affordable computational cost. As part of this objective, a parametric study has been built to determine how surface grid resolution impacts on both results' accuracy and computational cost.

3.1 Computational Geometry

It must be remembered that requirement **R.02** stated that several configurations of the selected geometric model shall be assessed in order to validate the final CFD setup. That said, we identify a baseline geometry, described in detail **Subsection 3.1.1**, and several additional configurations, explained in **Subsection 3.1.2**. Finally, **Subsection 3.1.3** describes the enclosure generation process.

Every geometric configuration, including its volume control, was created in Catia v5. This commercial software for computer-aided design (CAD) allows to transfer geometric designs into ANSYS Fluent environment easily, by exporting the final model in *.stp* format[3].

3.1.1 Baseline Geometry

CFD approach is demonstrated on a generic pylon/store configuration attached to a clipped delta wing, as shown in **Figure 3.1**. Computational geometry matches the experimental model described in **Subsection 2.2.2**, with the exception of the physical model being 1/20 scale[4]. In this regard, aircraft's wing is a 45-deg clipped delta with 7.62 m root chord L_c, 6.6 m semi-span b, and NACA 64A010 aerofoil section[5]. The pylon is located spanwise 3.3 m from the root and extends 61 cm below the wing leading edge.

---

[3] Even though *.igs* format is also recommended by some experts, it was found to be unpractical since several errors were reported due to the complexity of the geometry. These errors were avoided by using the *.stp* format.

[4] Wind tunnel tests described in **Subsection 2.2.2** do not scale with Reynolds number since no turbulence tripping at suspected transition locations was attempted. Notice that tripping is usually applied in wind tunnel testing as it makes the turbulent transition independent of the local condition of the free stream. Therefore, it helps to obey flow similarity for scaled models [30].

[5] All NACA aerofoils were easily obtained from www.airfoiltools.com.

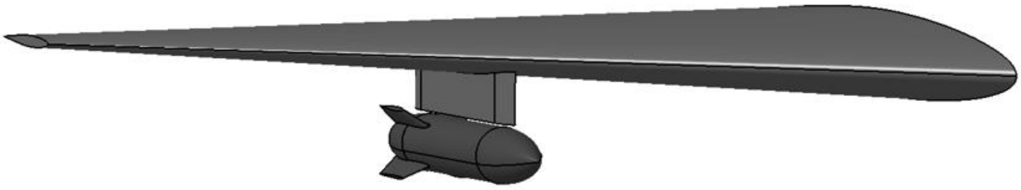

Figure 3.1 Baseline geometry perspective view

The store, shown in detail in **Figure 3.2**, consists of a tangent ogive forebody, clipped tangent-ogive afterbody, and cylindrical body 50 cm in diameter. Overall, the store length is approximately 3.0 m. Four fins are attached, each consisting of a 60-deg sweep clipped delta wing with NACA 0008 aerofoil section. The afterbody ogive is truncated to represent as faithfully as possible experimental conditions (the experimental model was truncated to accommodate the Captive Trajectory Support System). The store is positioned directly below the pylon with a small gap of 3.56 cm while in carriage position.

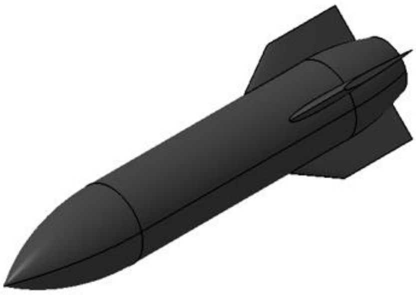

Figure 3.2 Store model

The reference lengths of the model are tabulated in **Table 3.1**. These values are used to obtain force and moment coefficients throughout all the simulations, as discussed in **Subsection 2.3.1**. More information about geometric generation, including technical drawings, can be found in **Appendix B**.

Characteristic magnitudes	**Values**
Reference surface S_{ref}, $[m^2]$	0.196
Reference Diameter D, [m]	0.5
Centre of gravity x_{CG}, [m]	1.417 (after nose store)

Table 3.1 Main reference lengths of the model

3.1.2 Additional Configurations

As stated in **R.02**, additional geometric configurations are required to validate the final CFD setup. First, the store alone over a range of angles of attack is considered. This setup, known as free stream configuration, allows to obtain longitudinal and lateral stability data. Hence, induced interferences when the store is close to the wing can be studied. Then, the full store/wing/pylon model is evaluated with the store translated in two different positions. These locations are representative of an intermediate (near) and the farthest position (far) when the store is released from aircraft. These two positions are defined by their translations and rotations with respect to the store centre of gravity while in carriage position. **Table 3.2** and **Table 3.3** represent near and far translations and rotations, respectively.

Store position	$\Delta X\ [m]$	$\Delta Y\ [m]$	$\Delta Z\ [m]$
Near	-0.064	-0.052	0.543
Far	-0.238	-0.094	1.213

Table 3.2 Store translations

Store position	$\psi[°]$	$\theta\ [°]$	$\phi[°]$
Near	4.95	5.20	2.80
Far	12.01	2.27	6.30

Table 3.3 Store rotations

Translations ΔX, ΔY, and ΔZ are referenced with respect to the global coordinate system, defined in **Subsection 2.3.1**. Rotations ψ, θ, and ϕ are the yaw, pitch, and roll angles, respectively. These rotations are positive with yaw outboard, pitch nose up, and roll clockwise when looking upstream, respectively. Store rotations correspond with a standard 321 Euler transformation about the store centre of gravity. Further details about how to obtain those rotations can be found in **Appendix C**. Finally, **Figure 3.3** and **Figure 3.4** illustrate near and far configuration, respectively.

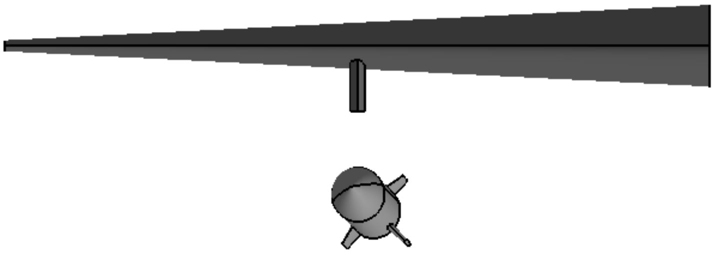

Figure 3.3 Near position

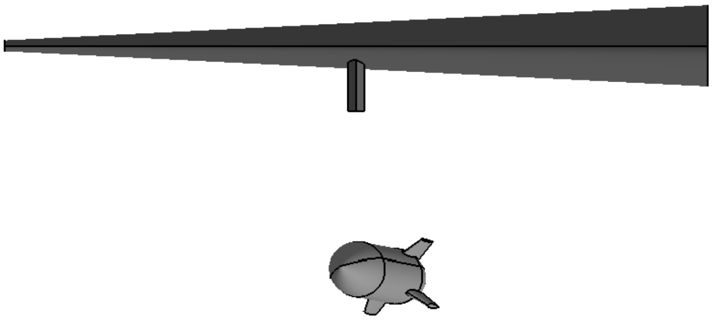

Figure 3.4 Far position

3.1.3 Enclosure

An external enclosure is necessary to envelope the bodies conforming a model so that the material surrounding them can be assigned as a fluid in ANSYS Fluent's environment. Additionally, the external enclosure shall approximate infinite-extents conditions. Although this aspect is argued in detail in **Section 3.3**, due to the type of chosen boundary conditions (i.e., pressure far-field), the inlet boundary is set as a quarter of sphere with a radius of $\sim 20L_C$ from the global frame origin, as suggested in theory guides [24]. At the wing root, a symmetry plane is applied to correctly reproduce the real behaviour. The downstream boundary is located approximately at $x = -20L_c$. Following these guidelines, the external enclosure was created, together with each geometric model, in Catia v5. **Figure 3.5** illustrates its characteristic shape. Notice that this enclosure must be the same for the full store/wing/pylon configuration with the store translated in different positions.

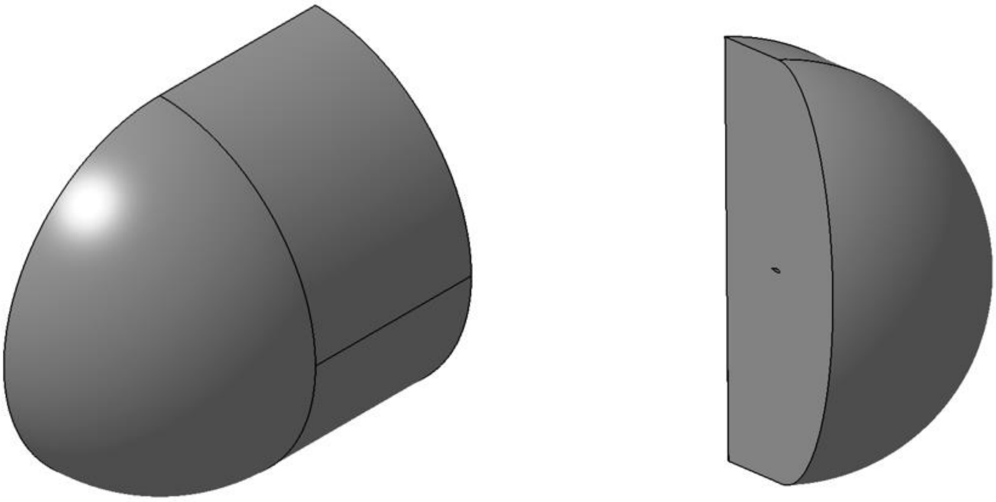

Figure 3.5 Enclosure perspectives

An inner enclosure near the wing/pylon/store structure could have been created in order to ease mesh refinement in the region close to the geometry, as there is where most of the variations in the fluid flow occurs. However, this type of approach would complicate the dynamic remeshing task when the store is released from aircraft. Therefore, this type of improvement is discarded.

In the free stream case (store alone), similar conditions were applied. This time, the inlet boundary was a quarter of sphere with a radius of $100D$, and the downstream boundary was located approximately at $x = -100D$. Additionally, a symmetry plane was used. Taking advantage of the former property, only half of the store had to be assessed, reducing a considerable amount of computational cost.

Then, within ANSYS Fluent's environment, an extrude Boolean operation is required between the external enclosure and the geometric model. Thus, the control volume can be set as a fluid, being subsequently meshed and assessed by the fluid flow solver.

3.2 Grid Generation

Modelling a reliable mesh, refined but also efficient is perhaps one of the most critical aspects within a CFD simulation as it has an explicit impact on fluid flow solver operation, both in convergence and accuracy of results. Several factors are involved but having a good comprehension about problem's physics is crucial in order to produce a mesh that guarantees that obtained results are reliable and sufficiently close to the real behaviour.

Regarding this last statement, a particular mesh could be refined as much as required to improve accuracy; however, this entails a subsequent increasing in the computational cost. Hence, finding a balance between these two characteristics is crucial. On the other hand, it is worth noting that the ANSYS Fluent software used during this work is the student version[6]. This package has some limitations with respect to the commercial version. One of them is the maximum number of admissible elements throughout the grid generation process. This value is limited to 520.000 elements; therefore, this is another restriction that must be considered in our design approach. However, as it will be seen later, former constraint is not restrictive at all as high quality meshes can be achieved.

The main goal of this section is to validate an unstructured grid setup based on an inviscid approach over each geometric configuration previously described. As a result of all that, two main topics are covered during this section. First, we study how surface grid resolution impacts on mesh quality and accuracy of results. Then, we identify the main factors that differentiate a mesh when a viscous fluid flow approach is required. Hence, an alternative mesh solution is created, and its quality is discussed. Among these objectives, the main requirement throughout this section is to ensure that created meshes provide grid independent solutions.

Thus, **Subsection 3.2.1** describes the main metrics that allow to justify whether a grid has been created with an appropriate quality. **Subsection 3.2.2** shows the grid generation process for each geometric configuration described in **Section 3.1**. To justify a correct meshing, some quality metrics are shown. Additionally, some experimental and published data are compared against numerical results to validate each solution. Finally, **Subsection 3.2.3** describes an alternative mesh setup when a viscous fluid flow solution is required.

3.2.1 Evaluating Grid Quality

ANSYS Fluent requires high quality meshes to avoid numerical diffusion. Several factors may affect mesh quality such as: small edges, gaps between faces or sharp angles within CAD model; inappropriate mesh resolution and distribution of elements; incorrect usage of Advanced Size function; inappropriate usage of Meshing Method function; inflation layers, etc.

To quantify mesh quality, several mesh metrics are involved. Those are: Element Quality, Aspect Ratio, Jacobian Ratio, Warping Factor, Parallel Deviation, Maximum Corner Angle, Skewness, and Orthogonal Quality. The minimum, maximum, averaged, and standard deviation for each metric can be shown within ANSYS Meshing Application.

In worst scenarios, and depending on the solver used, ANSYS Fluent might tolerate poor mesh metrics. However, poor mesh quality may lead to inaccurate results, bad physics description, and/or slow convergence. Among the beforementioned metrics, the most critical when working with Fluent are Skewness, Aspect Ratio and Orthogonal Quality. **Table 3.4** summarises these parameters with their minimum requirements. Finally, it is worth noting that every mesh shall guarantee that the minimum cell volume is positive (ANSYS reports negative cell volumes if mesh contains degenerated cells).

---

[6] This work has been developed using ANSYS Workbench 2021 R2, student version.

Mesh Metric	Allowable Range	Quality Requirement
Skewness	$[0,1]$	It shall be less than 0.9 for tetrahedral meshes. In some circumstances, the pressure-based solver can handle a small percentage of cells with skewness ~ 0.98.
Aspect Ratio	$[1,\infty)$	It should be less than 40, but more than 50 may be tolerated at the inflation layers.
Orthogonal Quality	$[0,1]$	It shall be always higher than 0.1.

Table 3.4 Main mesh metrics requirements for ANSYS Fluent

3.2.2 Inviscid Approach

When an inviscid approach is considered, fluid flow viscosity is considered to be neglected. Consequently, the Reynolds number approaches infinity and thus, the viscous forces can be neglected against inertial forces. Under these hypotheses, Navier-Stokes equations can be simplified to a form known as the Euler equations, as discussed in **Subsection 2.3.4**. On the other hand, the volume control can be meshed neglecting its boundary layer in the proximity of a solid. This simplifies the grid generation process.

Under this hypothesis, meshes for each geometric configuration of interest were created using tetrahedral elements. This setup is recommended when an unstructured grid approach is required due to its simplicity and ability to represent complex domains in an efficient manner [25]. To improve its behaviour, quadratic order elements were considered. This option retains mid-side nodes on each element so that, mesh properly captures the curvature of the geometry. However, it increases the degrees of freedom of the problem; therefore, the subsequent computational cost required by the fluid flow solver may increase. Following ANSYS Fluent user guide, *smoothing* parameter was set to *high* since it improves mesh quality by moving locations of nodes with respect to surrounding nodes and elements. Mesher is also set to *capture curvature* and *capture proximity*, to faithfully reproduce geometry characteristics. Finally, the *Patch Conforming Algorithm* was used. This feature applies an advancing-front point insertion technique for mesh refinement.

Three different grids, summarised in **Table 3.5**, were considered to study how surface grid resolution impacts on mesh quality and accuracy of results. The surface grid resolution on the store for each mesh type is represented by L_s, whereas L_w represents the surface grid resolution on the wing/pylon structure. Each grid setup is analysed below for all the geometric configurations.

Grid Type	$L_s\ [m]$	$L_w\ [m]$
Coarse	0.15	0.3
Nominal	0.075	0.2
Fine	0.0375	0.1

Table 3.5 Grid resolution options

3.2.2.1 Free-Stream Configuration

Based on surface grid resolution on the store L_s, three different meshes were produced for the free stream configuration (store alone). **Table 3.6** summarises the total number of elements for each type of grid.

Grid Type	Number of elements
Coarse	219990
Nominal	283570
Fine	401800

Table 3.6 Grid resolution for the free-stream problem

Surface grid resolution on the store for coarse, nominal and fine meshes are represented in **Figure 3.6**, **Figure 3.7**, and **Figure 3.8**, respectively. **Table 3.7 - Table 3.9** summarise the most important mesh metrics obtained by each grid approach.

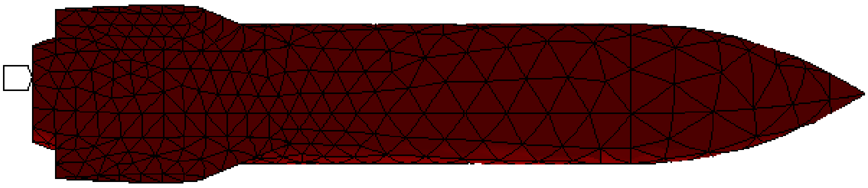

Figure 3.6 Coarse grid for the free stream configuration

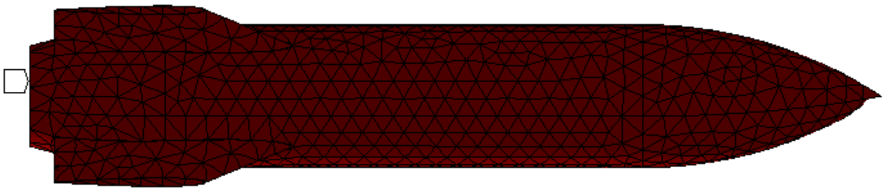

Figure 3.7 Nominal grid for the free stream configuration

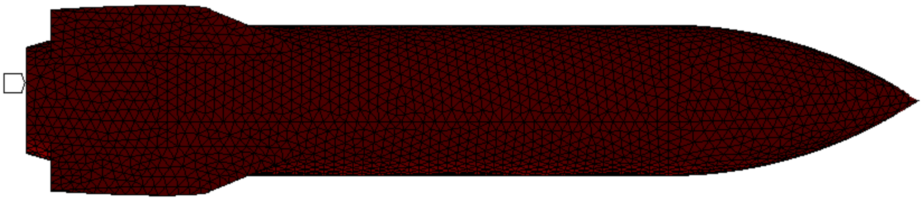

Figure 3.8 Fine grid for the free stream configuration

Mesh Metric	Minimum	Maximum	Average	Standard Deviation
Element Quality	0.30	0.99	0.80	$8.21 \cdot 10^{-2}$
Aspect Ratio	1.18	5.54	1.92	0.37
Skewness	$4.57 \cdot 10^{-4}$	0.72	0.27	$9.59 \cdot 10^{-2}$
Orthogonal Quality	0.28	0.99	0.73	$9.45 \cdot 10^{-2}$

Table 3.7 Mesh metrics for coarse grid

Mesh Metric	Minimum	Maximum	Average	Standard Deviation
Element Quality	0.31	0.99	0.80	$8.13 \cdot 10^{-2}$
Aspect Ratio	1.17	5.53	1.91	0.37
Skewness	$6.36 \cdot 10^{-4}$	0.72	0.27	$9.51 \cdot 10^{-2}$
Orthogonal Quality	0.28	0.99	0.73	$9.36 \cdot 10^{-2}$

Table 3.8 Mesh metrics for nominal grid

Mesh Metric	Minimum	Maximum	Average	Standard Deviation
Element Quality	0.32	1	0.81	$8.02 \cdot 10^{-2}$
Aspect Ratio	1.17	5.87	1.90	0.36
Skewness	$6.66 \cdot 10^{-4}$	0.77	0.26	$9.46 \cdot 10^{-2}$
Orthogonal Quality	0.23	0.99	0.73	$9.31 \cdot 10^{-2}$

Table 3.9 Mesh metrics for fine grid

As reflected in the above tables, mesh quality for the free stream configuration is more than acceptable, even for the coarse approach. On the other hand, there is not a significant improvement on mesh metrics with respect to surface grid resolution refinement.

Even though a more detailed assessment is tackled in **Chapter 4**, it is worth assessing how grid resolution has an impact on aerodynamic force and moment coefficients. **Table 3.10** summarises force and moment coefficients obtained by both wind tunnel tests and CFD simulation for each grid approach, for $M = 0.95$ and $\alpha = 0°$. As it can be seen, all meshes produce results in quite good agreement with experimental data. Discrepancies in C_N, C_A and C_m will be justified in **Chapter 4**.

Based on this analysis, two main conclusions can be inferred: a tetrahedral unstructured grid approach provides a reliable mesh with an acceptable quality for the free stream configuration; simulation results are almost grid independent. However, it must be proven if these conclusions remain when a more complex geometry is considered. Therefore, a similar analysis is performed for the baseline configuration.

Case	C_N	C_Y	C_A	C_m	C_n	C_l
Experimental	0.052	−0.012	0.268	−0.072	−0.044	0.005
Coarse	0.024	−0.013	0.402	−0.110	−0.038	0.006
Nominal	0.005	−0.013	0.354	−0.011	−0.039	0.005
Fine	0.004	−0.006	0.329	−0.006	−0.019	0.009

Table 3.10 Force and moment coefficients for free stream problem

3.2.2.2 Baseline Configuration

In a similar way, three different meshes were created for the baseline configuration based on L_s and L_w parameters. **Table 3.11** summarises the total number of elements for each type of grid.

Grid Type	Number of elements
Coarse	191323
Nominal	230506
Fine	469512

Table 3.11 Grid resolution for the baseline configuration

Surface grid resolution on baseline geometry for coarse, nominal, and fine approach are represented in **Figure 3.9**, **Figure 3.10**, and **Figure 3.11**, respectively. **Table 3.12 - Table 3.14** summarise the most important mesh metrics obtained by each grid approach.

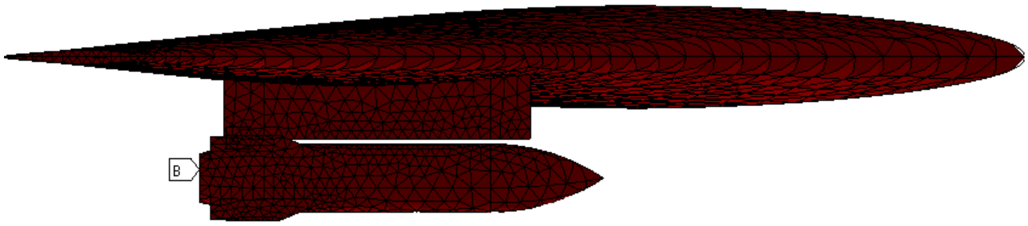

Figure 3.9 Coarse grid for baseline configuration

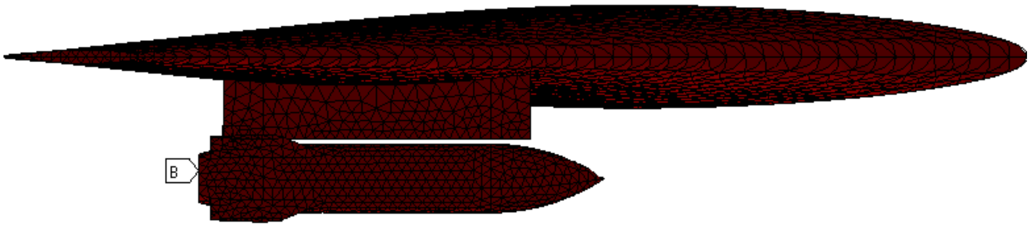

Figure 3.10 Nominal grid for baseline configuration

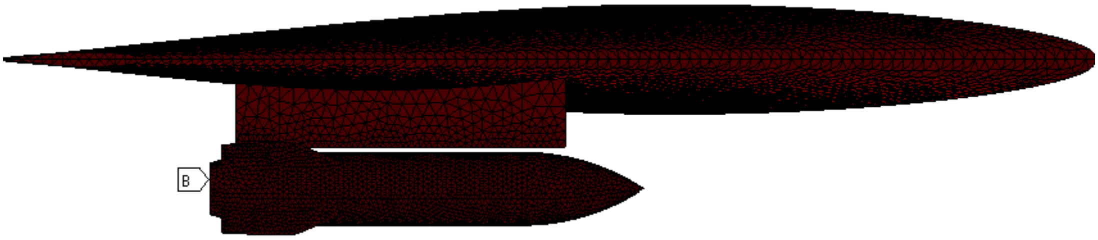

Figure 3.11 Fine grid for baseline configuration

Mesh Metric	Minimum	Maximum	Average	Standard Deviation
Element Quality	0.31	0.99	0.80	$8.22 \cdot 10^{-2}$
Aspect Ratio	1.18	5.53	1.91	0.37
Skewness	$1.86 \cdot 10^{-3}$	0.73	0.27	$9.68 \cdot 10^{-2}$
Orthogonal Quality	0.27	0.99	0.73	$9.54 \cdot 10^{-2}$

Table 3.12 Mesh metrics for coarse grid

Mesh Metric	Minimum	Maximum	Average	Standard Deviation
Element Quality	0.28	0.99	0.81	$8.16 \cdot 10^{-2}$
Aspect Ratio	1.18	5.52	1.90	0.37
Skewness	$1.02 \cdot 10^{-3}$	0.72	0.27	$9.64 \cdot 10^{-2}$
Orthogonal Quality	0.28	0.99	0.73	$9.50 \cdot 10^{-2}$

Table 3.13 Mesh metrics for nominal grid

Mesh Metric	Minimum	Maximum	Average	Standard Deviation
Element Quality	0.25	0.99	0.81	$8.00 \cdot 10^{-2}$
Aspect Ratio	1.18	5.94	1.89	0.36
Skewness	$1.83 \cdot 10^{-3}$	0.78	0.26	$9.55 \cdot 10^{-2}$
Orthogonal Quality	0.22	0.99	0.74	$9.41 \cdot 10^{-2}$

Table 3.14 Mesh metrics for fine grid

As reflected in the above tables, mesh quality is more than acceptable, even for the coarse approach. On the other hand, there is not a significant improvement on mesh metrics with respect to surface grid resolution refinement, as happened with the free stream configuration.

As we did previously, it is worth assessing how grid resolution has an impact on aerodynamic force and moment coefficients. **Table 3.15** summarises store's force and moment coefficients obtained by wind tunnel tests, published literature, and CFD simulation for each grid approach, for $M = 0.95$ and $\alpha = 0°$[7]. As it can be seen, all meshes produce results in quite good agreement with experimental data. Discrepancies in C_N, C_A and C_m will be justified in **Chapter 4**.

Case	C_N	C_Y	C_A	C_m	C_n	C_l
Experimental	0.644	−0.954	0.901	−1.430	1.520	0.100
Published [15]	0.687	−1.036	1.132	−1.761	1.791	0.104
Coarse	0.941	−1.007	1.167	−1.910	1.574	0.092
Nominal	0.967	−1.091	1.188	−1.957	1.704	0.096
Fine	0.928	−0.852	1.102	−1.747	1.449	0.058

Table 3.15 Force and moment coefficients on store for baseline configuration

Based on this analysis, two main conclusions can be inferred: a tetrahedral unstructured grid approach provides a reliable mesh with an acceptable quality for the baseline configuration; simulation results are almost grid independent. Consequently, it is decided that only nominal grids will be assessed for the rest of the work.

3.2.2.3 Full Configuration With The Store Translated In Two Positions

As justified previously, only nominal grids will be assessed throughout the rest of this work. Therefore, grids for the two store translation configurations are shown in **Figure 3.12** and **Figure 3.13**, respectively. Mesh metrics for each configuration are also shown in **Table 3.16** and **Table 3.17** to justify their correct modelling.

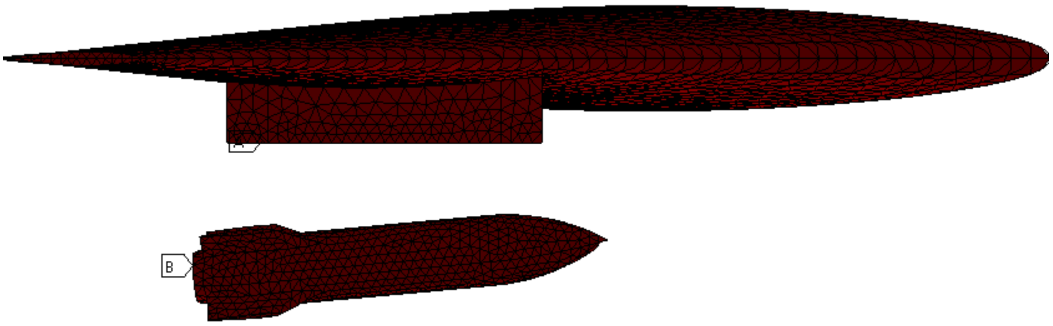

Figure 3.12 Grid for near configuration

---

[7] An analogous analysis was accomplished for $M = 1.2$ where similar results were obtained; however, it is not shown in this section for the sake of brevity. A more detailed analysis of results is shown in **Chapter 4**.

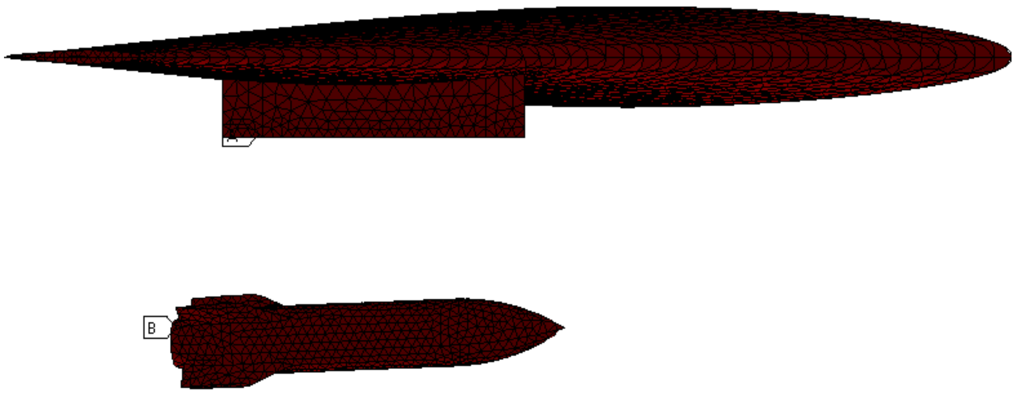

Figure 3.13 Grid for far configuration

Mesh Metric	Minimum	Maximum	Average	Standard Deviation
Element Quality	0.32	0.99	0.81	$7.95 \cdot 10^{-2}$
Aspect Ratio	1.17	5.88	1.89	0.36
Skewness	$4.06 \cdot 10^{-4}$	0.77	0.26	$9.48 \cdot 10^{-2}$
Orthogonal Quality	0.27	0.99	0.74	$9.34 \cdot 10^{-2}$

Table 3.16 Mesh metrics for near configuration

Mesh Metric	Minimum	Maximum	Average	Standard Deviation
Element Quality	0.32	0.99	0.81	$7.98 \cdot 10^{-2}$
Aspect Ratio	1.16	5.34	1.89	0.36
Skewness	$3.87 \cdot 10^{-5}$	0.72	0.26	$9.49 \cdot 10^{-2}$
Orthogonal Quality	0.28	0.99	0.73	$9.35 \cdot 10^{-2}$

Table 3.17 Mesh metrics for far configuration

As reflected in above tables, obtained mesh quality for each of the two configurations is more than acceptable. This situation will guarantee, on first instance, that numerical results are in good correlation to real behaviour.

3.2.3 Viscous Approach

Fluid behaviour near wall regions has a decisive impact on aerodynamic results. As described in **Section 2.3**, several turbulent models are available to model this behaviour. It is a responsibility of the designer to select the model that suit the best the conditions of the stated problem. In this context, a huge number of turbulent flows tend to describe a similar behaviour when close to a wall or surface. This behaviour can be displayed in terms of dimensionless parallel speed u^+ and dimensionless length from the wall y^+ [22] as:

$$y^{+} = \frac{y u_{\tau}}{\nu} \; ; \; u^{+} = \frac{u}{u_{\tau}} \qquad \textbf{(3.1)}$$

with,

$$u_{\tau} = \sqrt{\frac{\tau_{w}}{\rho}} \qquad \textbf{(3.2)}$$

where u_{τ} is known as the shear velocity, τ_{w} is the wall shear stress, ρ is the density, and ν is the kinematic viscosity. Hence, three different layers can be observed when plotting these two variables: laminar sublayer, turbulent layer, and buffer layer (see **Figure 3.14**).

Thus, the laminar sublayer is characterised by a linear behaviour, where:

$$y^{+} = u^{+} \qquad \textbf{(3.3)}$$

The turbulent layer is described by the logarithmic behaviour, where:

$$u^{+} = \frac{1}{k} ln \; (y^{+}) + B \qquad \textbf{(3.4)}$$

with k being the Karman constant ($k \approx 0.41$) and $B \approx 5$ for a smooth wall, based on experiments [26].

Finally, buffer layer is a transition zone between these two previous defined regions. These three layers can be distinguished in **Figure 3.14**.

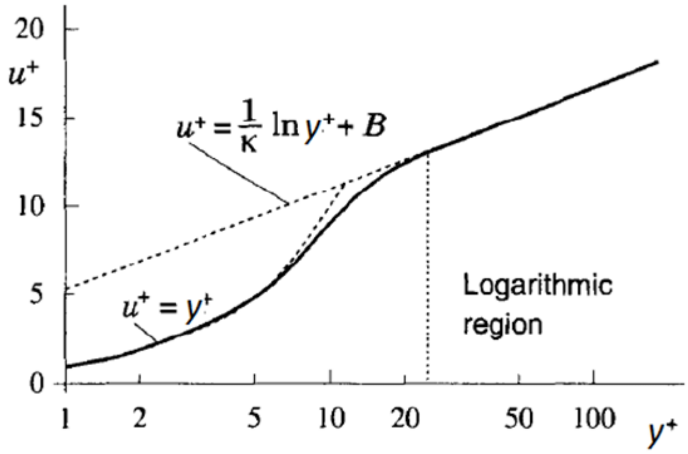

Figure 3.14 Dimensionless horizontal velocity near the wall [27]

Figure 3.14 shows that for $y^+ < 5$ the profile is linear, whereas for $y^+ > 30$ it is logarithmic (notice that the figure is represented in a logarithmic scale). Finally, in buffer layer $(5 < y^+ < 30)$ there is a transition in between both profiles. Capturing the entire profile is crucial in CFD simulations in order to obtain accurate results; therefore, the first mesh layer shall be at a heigh equivalent to $y^+ \approx 1$. However, assessing the complete profile is a complex task due to numerical instabilities and associated computational cost. Depending on the turbulence model, some have a feature called *wall treatment*, which are approximations that allows to start meshing at the logarithmic region, modelling the buffer and viscous layer by semi-empirical functions.

This is the case of the Spalart-Allmaras model, having an insensitive wall treatment that automatically blends from the viscous layer to the logarithmic one. In the intermediate regions, the model maintains its integrity, providing consistent values for the wall shear stresses and other variables [21]. Based on user guide recommendations, y^+ is set to 35 for the rest of this work. On the other hand, wing/pylon structure is remained as an inviscid surface because its modelling has little impact when the store is detached from the parent structure; therefore, only the store is considered as a viscous body.

After these conclusions, the only aspect left is knowing the vertical coordinate value y of the first inflation layer within our CFD model. To calculate it, the wall shear stress must be known. However, this will not be possible as the problem has not been solved yet. To overcome this issue, it is common to use the flat plate boundary layer behaviour as a reference, as it gives sufficiently similar results in most of the cases. In this case, the procedure followed is shown.

First, the Reynold number in the vicinity of the store must be estimated.

$$Re = \frac{\rho_\infty U_\infty D}{\mu_\infty} \tag{3.5}$$

With this, the friction coefficient can be obtained, based on Prandtl's one-seventh-power law [23]:

$$C_f = \frac{0.026}{Re^{1/7}} \tag{3.6}$$

Knowing this, the wall shear stress can be obtained as:

$$\tau_w = C_f \frac{1}{2} \rho_\infty U_\infty^2 \tag{3.7}$$

Finally, the shear velocity is calculated with **(3.2)** obtaining, after that, the vertical distance of the first inflation layer y as:

$$y = \frac{y^+ \mu_\infty}{\rho_\infty u_\tau} \tag{3.8}$$

The vertical distance of the first inflation layer for each flight envelope considered during this work is represented in **Table 3.18**.

M	$y\ [m]$
0.95	$2.335 \cdot 10^{-4}$
1.2	$2.255 \cdot 10^{-4}$

Table 3.18 Distance of the first layer for each flight envelope

Finally, it shall be guaranteed that the velocity boundary layer thickness δ_v is contained within the total height of the inflation layer y_T. Hence:

$$y_T = \delta_v \tag{3.9}$$

where, according to [26]:

$$\delta_v = \frac{0.38L}{Re_L^{\frac{1}{5}}} \tag{3.10}$$

where L is the total length of the store. If a geometric growth rate is applied to build the inflation layers[8], its total height can be computed as:

$$y_T = \sum_{k=0}^{N-1} y \cdot G^k = y \cdot \frac{1 - G^N}{1 - G} \tag{3.11}$$

where y is the vertical distance of the first layer, G is the growth rate (set as 1.2 for our problem), and N is the total number of layers. Applying above considerations, at least 21 layers shall be considered for both flight envelopes to guarantee that the boundary layer is fully contained within our inflation layer. **Figure 3.15** shows the inflation layer around the store for the free stream configuration, at $M = 0.95$ and nominal grid features.

Finally, **Table 3.19** summarises the main mesh metrics for the above configuration. Minimum quality requirements were not accomplished for some metrics. This is thought to be due to the restriction on the maximum number of grid elements. Moreover, it must be noticed that the addition of inflation layers challenge meshing development when an unstructured approach is considered. A structured approach is thought to improve the quality of the generated grid however, this solution is out of the scope of this work. The viscous approach is simulated for the free stream configuration and main results are shown in **Chapter 4**.

---

[8] ANSYS Mesher Application allows other types of schemes to build the inflation layers.

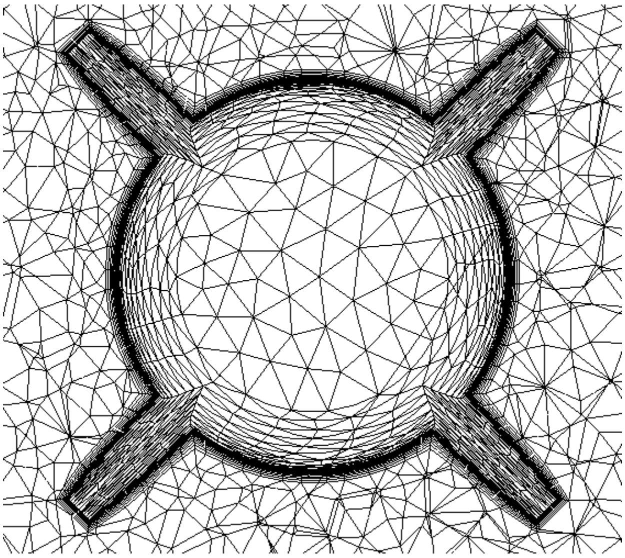

Figure 3.15 Inflation layer around store

Mesh Metric	Minimum	Maximum	Average	Standard Deviation
Element Quality	$1.84 \cdot 10^{-3}$	1	0.65	0.32
Aspect Ratio	1.17	434.02	18.52	42.37
Skewness	$9.54 \cdot 10^{-4}$	0.95	0.25	0.11
Orthogonal Quality	$1.21 \cdot 10^{-2}$	0.99	0.73	0.14

Table 3.19 Mesh metrics for viscous mesh

3.3 Fluid Flow Solver

Another critical aspect within CFD simulation is fluid flow solver selection, which is used to solve the governing fluid-dynamic equations over the control volume. Several factors are involved but having a good comprehension about problem's physics is crucial in order to produce a CFD simulation that guarantees that obtained results are reliable and sufficiently close to the real behaviour. To accomplish it, several aspects must be considered such as the type of solver, fluid flow model, chosen boundary conditions, solution method, or a correct convergence of results. Along this section, the main features that characterise the fluid flow solver are discussed, trying to find out a solver setup that reproduces in the best possible way the physics behind our problem.

3.3.1 Solver Type

ANSYS Fluent allows to choose between two numerical methods to solve the governing fluid-dynamic equations: pressure-based and density-based solver. Historically, the pressure-based approach was mainly used for low-speed incompressible flows, while the density-based approach was mainly used for high-speed compressible flows. However, recently both methods have been extended and reformulated to solve a wide range of flow conditions beyond their original intent.

In both methods, the velocity field is obtained from the momentum equations. In the density-based approach, the continuity equation is used to obtain the density field while the pressure field is determined from the equation of state. On the other hand, in the pressure-based approach, the pressure field is extracted by solving a pressure equation which is obtained by manipulating continuity and momentum equations [21].

In density-based solver, time plays an important role, whether the formulated problem is steady or transient, by incorporating a transient term in the equations to be solved (this term is represented by the Courant number in steady state problems). This might translate into some stability issues. Fluent User Guide certainly recommends using a density-based solver over a pressure-based solver when $M > 1.5$. For compressible flows below this value, solver selection depends upon problem's nature. Hence, a comparative analysis between these two approaches was developed to determine the best approach for our problem[9].

Baseline configuration was simulated for $M = 0.95$ and $\alpha = 0°$. Pressure-based solver outperformed in terms of stability, convergence of residuals, and computational cost. This can be justified by observing **Figure 3.16** and **Figure 3.17**. **Table 3.20** summarises required computational cost for each solver[10]. Finally, **Table 3.21** shows that force and moment coefficients for each solver type are almost equivalent, and they are in good correlation with respect to experimental data.

A similar analysis was developed for $M = 1.2$. In that case, residuals tended to infinite for the density-based solver. By applying solution steering with a transonic model correction, residuals decreased this time, although pressure-based solver still outperformed in terms of computational cost, stability, and convergence of residuals.

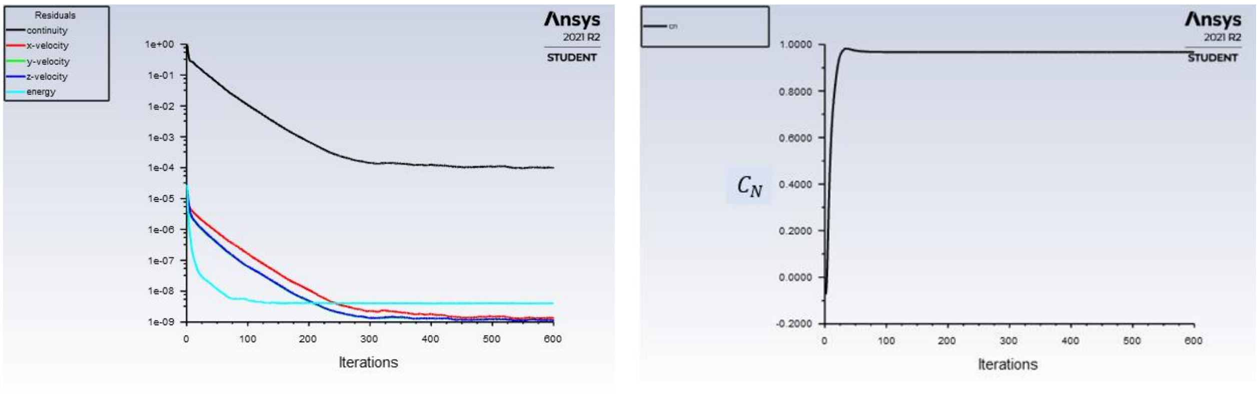

Figure 3.16 Residuals and C_N evolution for pressure-based solver

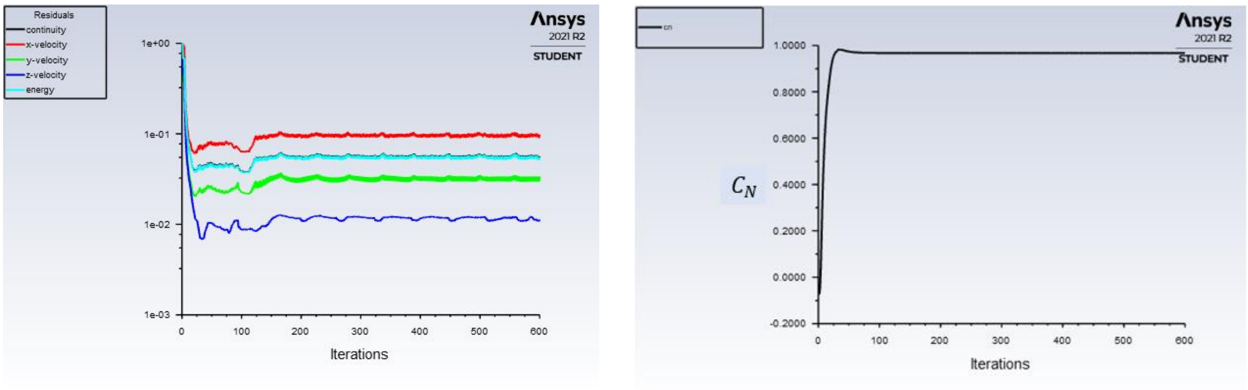

Figure 3.17 Residuals and C_N evolution for density-based solver

---

[9] Pressure-based solver was compared against density-based solver. The former option employed an implicit Roe-FDS method (implicit approach improves convergence over explicit approach), with a second order upwind discretisation and a Green-Gauss node-based scheme. Additionally, a pseudo-transient relaxation method was applied (it helped to solution stabilisation while improving convergence). Finally, a hybrid initialisation was used.

[10] The computer used to perform all the simulations is an Intel Core i7-4510U CPU @2.00 GHz – 2.60 GHz, with 6.00GB of RAM memory.

Case	Computational Cost, CC	Number of Iterations, N	CC/N
Pressure-based	$26'22''$	600	$2.64''$
Density-based	$43'36''$	600	$4.36''$

Table 3.20 Computational cost required by each solver

Case	C_N	C_Y	C_A	C_m	C_n	C_l
Experimental	0.644	-0.954	0.901	-1.430	1.520	0.100
Pressure-based	0.967	-1.091	1.188	-1.957	1.704	0.096
Density-based	0.960	-1.106	1.214	-1.934	1.807	0.092

Table 3.21 Force and moment coefficients for each solver

It must be noticed that viscosity inclusion does not have an impact on previous comparative analysis since turbulence quantities are calculated in an independent step of the algorithm, whether the solver is pressure-based or density-based.

Thus, a pressure-based solver is considered to be the most efficient option to work out our problem, mainly due to its lower computational cost. Remember that computational cost will be a demanding requirement when assessing the non-stationary release problem. Two different algorithms are available in ANSYS-Fluent for a pressure-based solver: a segregated and a coupled algorithm. Its election is discussed in **Subsection 3.3.4**.

Finally, fluid flow solver is computed under steady conditions and gravity acceleration is ignored. The former condition is justified by the fact that Froude number, representing the ratio of the flow inertia to the gravity field, follows $Fr \gg 1$ with:

$$Fr = \frac{U_\infty}{\sqrt{gL}} \tag{3.12}$$

where U_∞ is the free stream velocity, g is the gravity acceleration, and L is the total length of the store.

3.3.2 Model Selection

ANSYS Fluent provides modelling capabilities for a wide range of incompressible and compressible, laminar and turbulent fluid flow problems. To achieve that, several features are provided within its interface. Having a good comprehension about problem's physical behaviour is crucial in order to choose, among these features, those that guarantee that obtained results are reliable and sufficiently close to the real behaviour. Based on requirements stated in **Section 1.3**, our fluid flow can be characterised by the following two main assumptions:

- Compressible fluid flow: compressible effects are encountered when $M > 0.3$. These flows are characterised by having significant changes in density with pressure, having an impact on flow's velocity, pressure, and temperature.
- Adiabatic fluid flow: an adiabatic process occurs when there is not transferring heat or mass between the thermodynamic system and its environment.

Regarding the first assumption, compressible flows are described by the standard continuity and momentum equations in ANSYS Fluent. However, the energy equation incorporates the coupling between flow's velocity and static temperature. Consequently, this equation shall be activated whether a compressible flow is solved within ANSYS Fluent.

Concerning the second assumption, an adiabatic process can be mathematically expressed by the ideal gas model. This equation describes the relationship between pressure, density, and temperature for a fluid, by:

$$\rho = \frac{p}{R_g T} \tag{3.13}$$

where the specific heat C_p, thermal conductivity, viscosity, and molecular weight are considered to be constant; additionally, default values were used during all the simulations.

Finally, viscous/inviscid behaviour shall be assessed. ANSYS Fluent incorporates an option to analyse inviscid flows. Under this consideration, Fluent solves the Euler equations. In this model, the mass conservation equation is the same as for a laminar flow, but the momentum and energy conservation equations are reduced due to the absence of molecular diffusion.

If a viscous approach is selected, ANSYS Fluent solves RANS equations. As it was discussed in **Chapter 2**, the Spalart-Allmaras model is considered throughout this work. This turbulent approach is a one-equation model that solves a modelled transport equation for the kinematic eddy viscosity. In its original form, the Spalart-Allmaras model is efficiently at low Reynolds numbers, requiring the viscous sublayer of the boundary layer to be properly resolved (this means $y^+ \sim 1$ meshes, as described in previous section). However, this model has been extended with a y^+ insensitive wall treatment (called *enhanced wall treatment*), which allows the application of the model independent of the near wall y^+ resolution, considerably alleviating some of its computational cost. It only should be ensured that the boundary layer is resolved with a minimum resolution of 10-15 layers (this requirement was previously guaranteed in **Subsection 3.2.3**). Finally, Spalart-Allmaras model is based upon several experimental constants, which are remained with their default values during all the simulations.

3.3.3 Boundary Conditions and Reference Values

Boundary conditions specify the flow and thermal variables on the edges of the physical model. They are a critical component of the simulation; therefore, it is important that they are specified properly. In this regard, a non-permeable wall boundary condition is imposed on both the wing/pylon structure and the store. A pressure far-field condition is used at the upstream, downstream, and lateral extents of the control volume. Finally, at the wing root, a symmetry plane is employed.

Pressure far-field is commonly used for compressible flows to model a free stream condition at infinity, with Mach number, static pressure, static temperature, and flow direction being specified. Two Mach number values are assessed during this work ($M = 0.95$ and $M = 1.2$) according to requirement **R.05**, even though most of the available experimental data was found only for $M = 0.95$. Moreover, several angles of attack α are considered (those values are shown in **Chapter 4**).

In order to obtain the static pressure and temperature required by the pressure far-field condition, first it is necessary to set a flight altitude. According to **R.04**, the flight altitude shall be 11600 m. Using the International Standard Atmosphere (ISA) model (described in **Appendix A**), the static pressure, temperature, and density can be obtained. Those values are shown in **Table 3.22**.

Altitude $[m]$	**Pressure** $[Pa]$	**Temperature** $[K]$	**Density** $[kg/m^3]$
11600	20588	216.65	0.3310

Table 3.22 Fluid magnitudes according to ISA model

However, since aircraft is flying at a certain speed, real values of static pressure and temperature need to be recalculated. This can be done by assuming the airflow at the boundaries of the far enclosure has an isentropic behaviour. Thus, equations **(3.14) - (3.15)** can be used to obtain the real static temperature and pressure with respect to the Mach number.

$$\frac{p_0}{p} = \left[1 + \frac{\gamma - 1}{2} \cdot M^2\right]^{\frac{\gamma}{\gamma - 1}} \qquad \textbf{(3.14)}$$

$$\frac{T_0}{T} = 1 + \frac{\gamma - 1}{2} \cdot M^2 \qquad \textbf{(3.15)}$$

where p_0 and T_0 are the total pressure and temperature, previously computed by the ISA model; p and T are the static pressure and temperature for a particular flight condition, respectively; M is the Mach number; and γ is the heat capacity ratio, which is considered to be constant and equal to 1.4 along this work. Hence, final static magnitudes can be obtained for each of the two flight envelopes. These values are shown in **Table 3.23**.

$\boldsymbol{M}$	$\boldsymbol{p}$ $[\boldsymbol{Pa}]$	$\boldsymbol{T}$ $[\boldsymbol{K}]$
0.95	11518	183.52
1.2	8490	168.21

Table 3.23 Static conditions for each Mach number

Once these variables are set, density can be obtained through the ideal gas law, previously defined by equation **(3.13)**.

It is worth noting that some fluid flow conditions could be affected by roundoff errors[11]. To avoid this problem, ANSYS Fluent subtracts an operating pressure (generally a large pressure roughly equal to the average absolute pressure in the flow) from the absolute pressure, and uses the result (named as gauge pressure) for further calculations. The relationship between the operating pressure p_{op}, gauge pressure p_{gauge}, and absolute pressure p_{abs} is shown below.

$$p_{abs} = p_{op} + p_{gauge} \qquad \textbf{(3.16)}$$

Roundoff error is less significant for high Mach number compressible flows (that is the case of our problem). Therefore, it is common convention to set the operating pressure to zero, making gauge pressure and absolute pressure equivalent. This simplifies post-analysis tasks since all pressures computed or reported by ANSYS Fluent are gauge pressures.

Having specified the boundary conditions, the next step is to define the reference values. These shall be correctly specified in order to obtain the same force and moment coefficients as defined in the experimental data. Hence, the reference area is the store cross-sectional area, while the reference lengths are the store diameter and the centre of gravity of the store (the former is used to compute moment coefficients). Those values were previously stated in **Table 3.1**, in **Section 3.1**.

---

[11] In low Mach number compressible flows, the overall pressure drop is small compared to the absolute static pressure, and density calculation can be significantly affected by numerical roundoff.

3.3.4 Solution Method

As previously mentioned in **Subsection 3.3.1**, the pressure-based solver allows to solve the problem in either a segregated or coupled manner. The coupled approach offers some advantages over the segregated approach. In particular, the couple scheme is more robust and efficient; similarly, the rate of solution convergence considerably improves. However, it implies a memory requirement increment by 1.5-2 times compared to the segregated algorithm.

To improve accuracy, a second order discretisation scheme is applied over pressure, density, momentum, and energy magnitudes. This is highly recommended when tetrahedral meshes are employed. Moreover, a Green-Gauss node-based scheme is applied since it is known to improve accuracy when tetrahedral unstructured meshes are used; however, this approach is relatively more expensive to compute, in comparison with the rest of schemes (such as the Green-Gauss cell-based). Finally, a high order term relaxation scheme is employed. This improves the start-up and the general solution behaviour when the second order discretisation scheme is used; also, it shown to prevent convergence stalling in some cases, according to [21]. As a consequence of the election of these methods, high-quality CFD simulations were obtained. This is supported by the convergence of residuals found in all the simulations accomplished along this work (see **Chapter 4**).

Before starting each CFD simulation, ANSYS Fluent must be provided with an initial guess for the solution flow field. Due to the nature of our problem, a hybrid initialisation is recommended. This technique is a collection of formulas and boundary interpolation methods. It iteratively solves Laplace’s equation to determine the velocity and pressure fields. In some simulations during this work, the number of iterations required to initialise the solution had to be increased from the predefined value in order to reach the minimum recommended convergence tolerance of 1e-06. Finally, each CFD simulation was ran for 600 of iterations. Main results and conclusions for each of those simulations are discussed in detail in **Chapter 4**.

4 RESULTS

In this chapter, CFD results for each simulation are presented and described, leaving some interesting discussions and conclusions. When possible, CFD results are assessed against experimental data and published literature to validate each design configuration. Likewise, all the assumptions considered until this point are reviewed. This will allow us to justify their consistence and discuss their limits. The chapter is divided into three main sections, each one dedicated to a particular configuration. **Section 4.1** summarises the main results for the free stream configuration (store alone); **Section 4.2** describes the outcomes for the baseline configuration; finally, **Section 4.3** deals with the two store translations about the carriage position. Achieved outcomes include, among other results, force and moment coefficients and surface pressure distributions. This allows to determine the limits of the designed configuration and validate its correct operation. It must be noticed that most of the found experimental data corresponds to $M = 0.95$. Consequently, most of the CFD results are shown for the former condition. Nevertheless, solutions for $M = 1.2$ are also discussed.

4.1 Free Stream Configuration

During this section, the store in free stream configuration is assessed. As described in detail in **Chapter 3**, three different meshes, based on surface grid resolution on the store L_S, were produced for the free stream configuration. The main aim was to validate an unstructured grid setup able to provide solutions that are independent to the grid itself (i.e., grid independent solutions). Even though it was concluded that a nominal mesh was sufficient to generate reliable simulations, a more exhaustive justification is displayed along this section.

First, it is worth pointing the evolution of the store's force and moment coefficients with respect to the angle of attack α of the free stream. Results are shown in **Figure 4.1** – **Figure 4.3** for coarse, nominal, and fine grid conditions, respectively. Asterisk marks are employed to display experimental data obtained from [10]. Flight condition for each of these simulations is $M = 0.95$.

Regarding the aerodynamic force coefficients, it can be noticed that the normal force coefficient C_N is in quite good agreement with experimental data, for each of the three types of meshes. Similarly, this happens with the lateral force coefficient C_Y for most of the angles of attack under analysis (notice that significant discrepancies are found for $\alpha > 10°$). Finally, it is worth noting that the axial force coefficient C_A follows the expected behaviour, but this coefficient is oversized by a factor of ~ 1.3 when compared to the experimental data. The main reason behind this issue could be the modelling of the aft end of the store. Wind tunnel model of the store has a modified aft region followed by the Captative Trajectory Support System, as shown in **Figure 4.4**. The CFD model did not include this device; consequently, this has an impact on the base drag. As it will be justified later in this section, negative pressure coefficients appear behind the aft end of the CFD model. This indicates that the flow around this region is separated from the store surface, suggesting that base drag is significant in this particular region. According to [28], base drag assumes an approximately constant percentage of the theoretical limit of the total drag, for slender bodies. This justifies the origin of the former discrepancy.

About the aerodynamic moment coefficients, the rolling moment coefficient C_l is well correlated for all the angles of attack. The pitching moment coefficient C_m, which is an important quantity in determining the store trajectory during the releasing problem [12], is well predicted. However, it is worth noting that some discrepancies appear when the mesh is refined, for $\alpha > 10°$. This divergence was also noticed by [29]. The author concludes that, for angles of attack above the previous limit, viscous models are necessary to improve accuracy. Finally, some evident discrepancies were found for the yawing moment coefficient C_n in each of the three simulations. This could be a consequence of the numerical errors found in the store's lateral forces. Nevertheless, the former coefficient has not a significant impact on the final trajectory of the store, according to [11] and [12].

To sum up, aerodynamic force and moment coefficients are in quite good agreement with respect to experimental data and published literature. Additionally, it has been validated that mesh setup guarantees grid independent solutions. The remaining discussions throughout this section are shown for a nominal mesh setup.

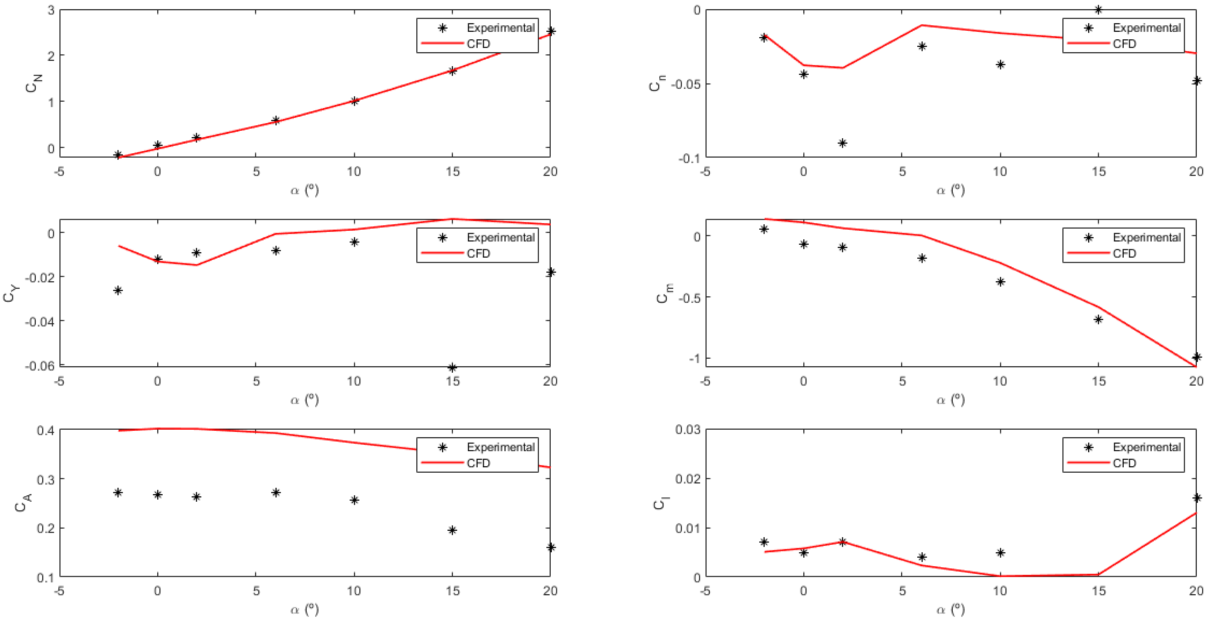

Figure 4.1 Force and moment coefficients for coarse mesh

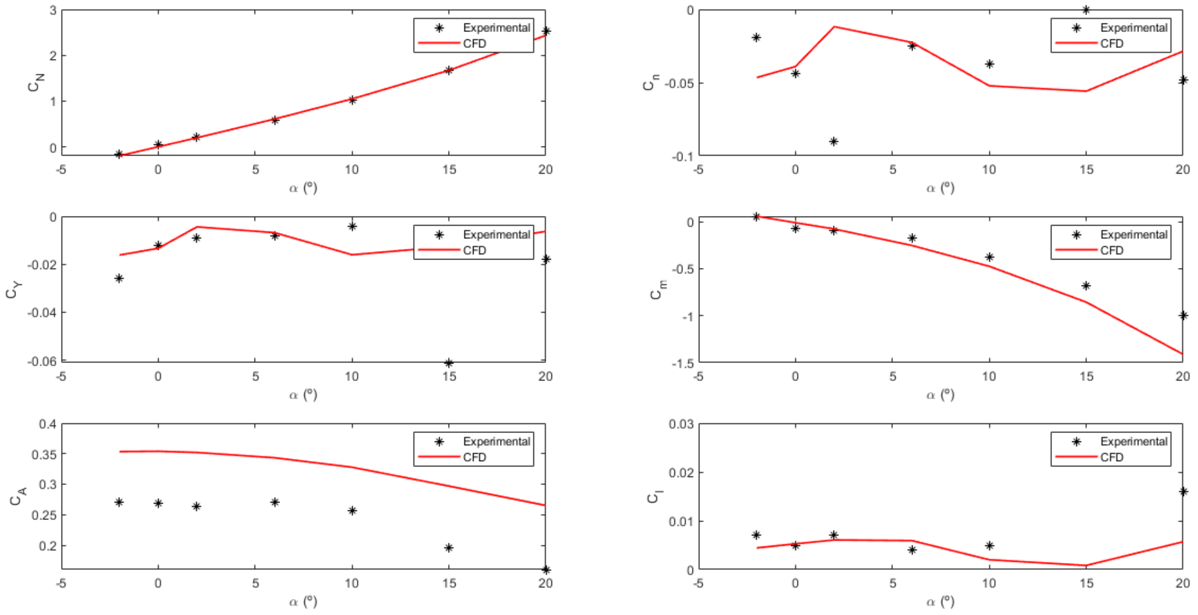

Figure 4.2 Force and moment coefficients for nominal mesh

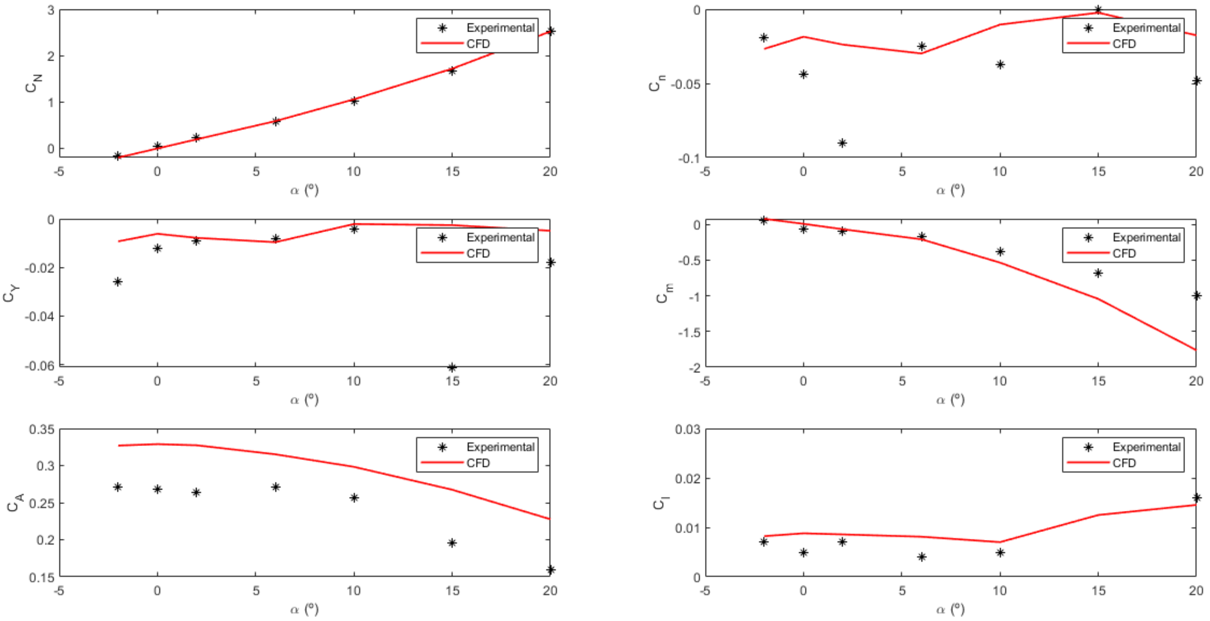

Figure 4.3 Force and moment coefficients for fine mesh

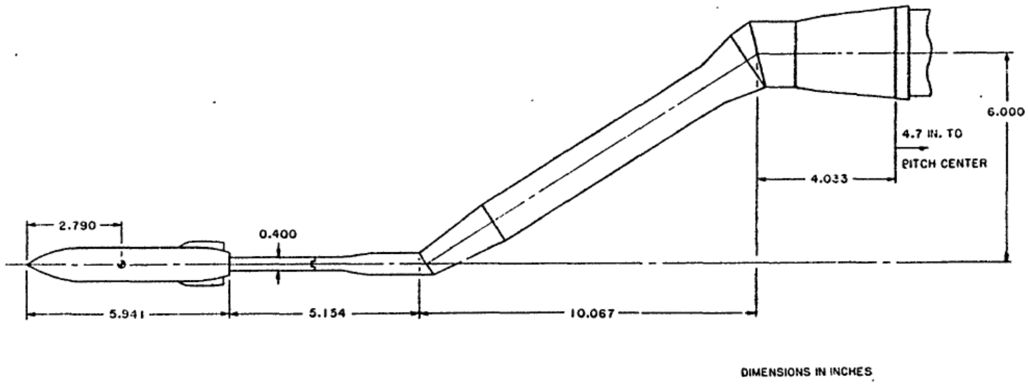

Figure 4.4 Experimental model of the store according to [10]

Further conclusions are shown along the rest of this section to better understand the physics behind our problem. In particular, both C_p and Mach contours are shown for an angle of attack of $\alpha = 0°$. **Figure 4.5** and **Figure 4.6** show the results for a flight condition of $M = 0.95$.

Under these conditions, the very front section of the store is characterised by a distribution of high pressures (see **Figure 4.5**). As described in **Chapter 2**, this is clear evidence of the existence of a weak shock wave. This is also justified by **Figure 4.6**, where an important reduction in fluid flow velocity is found (from $M{\sim}1$ until $M{\sim}0.12$). Then, an expansion wave is found at the beginning of the cylindrical section of the store. This is characterised by a continuous reduction in the pressure. On the other hand, fluid flow velocity continuously increases until it turns into supersonic (reaching a maximum value of $M{\sim}1.2$). It must be noticed that this evolution occurs in a more continuous way, unlike for a shock wave. For the rest of the cylindrical part of the store, both velocity and pressure remain almost constant. The aft part of store is characterised by another expansion wave, where supersonic velocities are reached again. Notice that the maximum fluid flow velocity is reached at the truncated part of the store ($M{\sim}1.45$). Finally, this region is characterised by negative C_p values. As demonstrated before, this suggests that a recirculating region (or turbulent wake) appears behind the end of the store. As a consequence, base drag would be a significant component of the total drag. Additionally, some oscillations may appear on force and moment coefficients.

A similar behaviour was found for a flight condition of $M = 1.2$. Both C_p and Mach contours are shown in **Figure 4.7** and **Figure 4.8**, respectively.

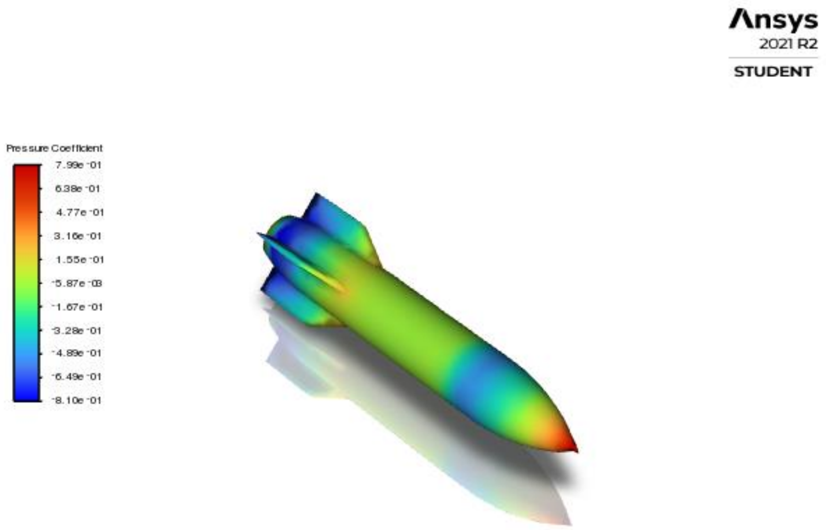

Figure 4.5 C_p contours for $M = 0.95$

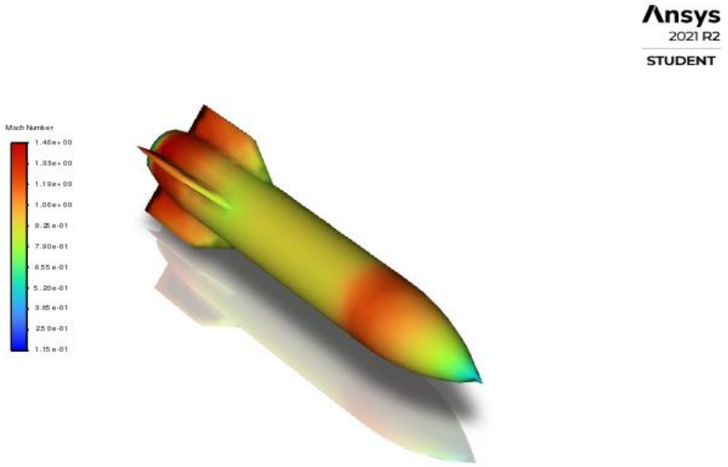

Figure 4.6 Mach contours for $M = 0.95$

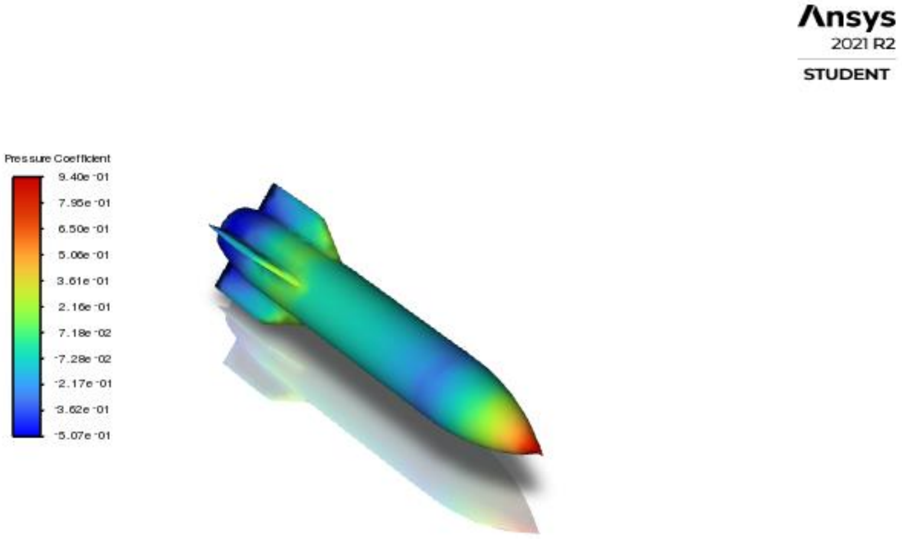

Figure 4.7 C_p contours for $M = 1.2$

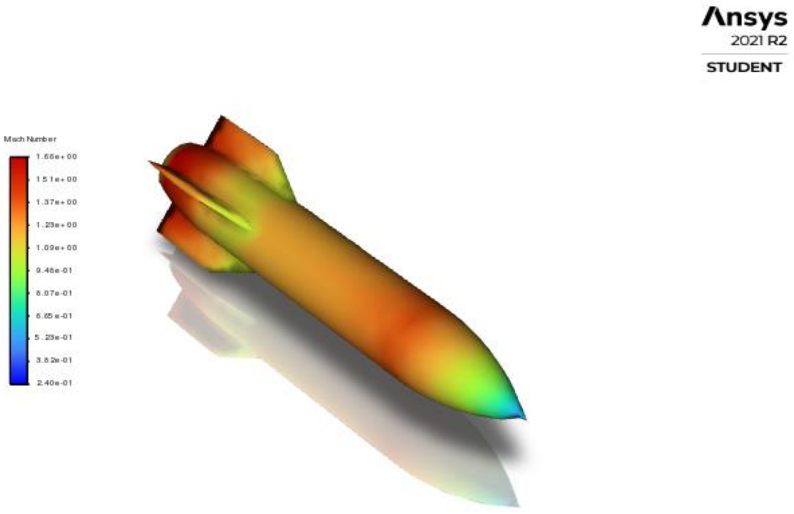

Figure 4.8 Mach contours for $M = 1.2$

Finally, **Figure 4.9** and **Figure 4.10** represent fluid flow velocity vectors close to the store's surface for $M = 0.95$ and $M = 1.2$, respectively. Notice that the shock wave originated in the very front section of the store can be easily found in the left-side figures (i.e., yellow/green region). On the right-side figures, on the other hand, the recirculating region close to the aft region of the store is identified (notice that this region is more prominent for $M = 1.2$). This reinforces all the conclusions displayed within this section.

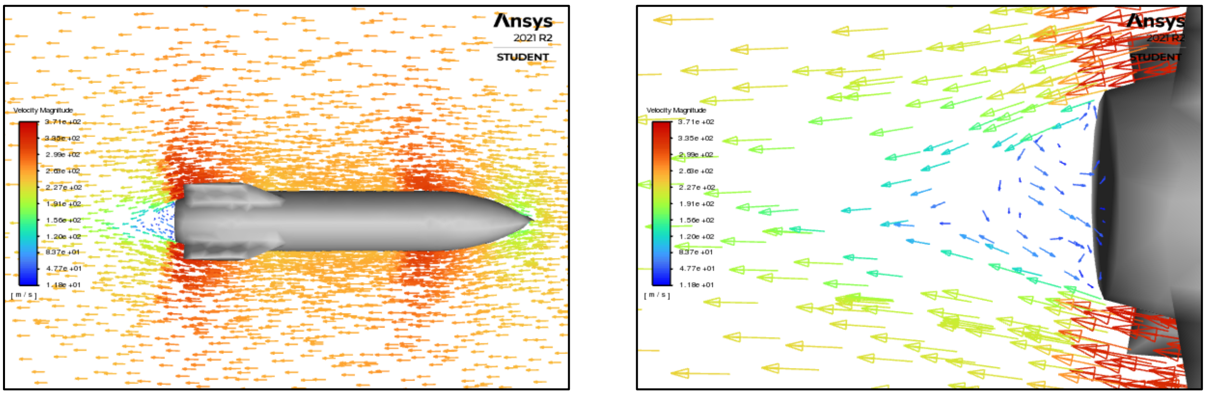

Figure 4.9 Fluid flow velocity vectors for $M = 0.95$

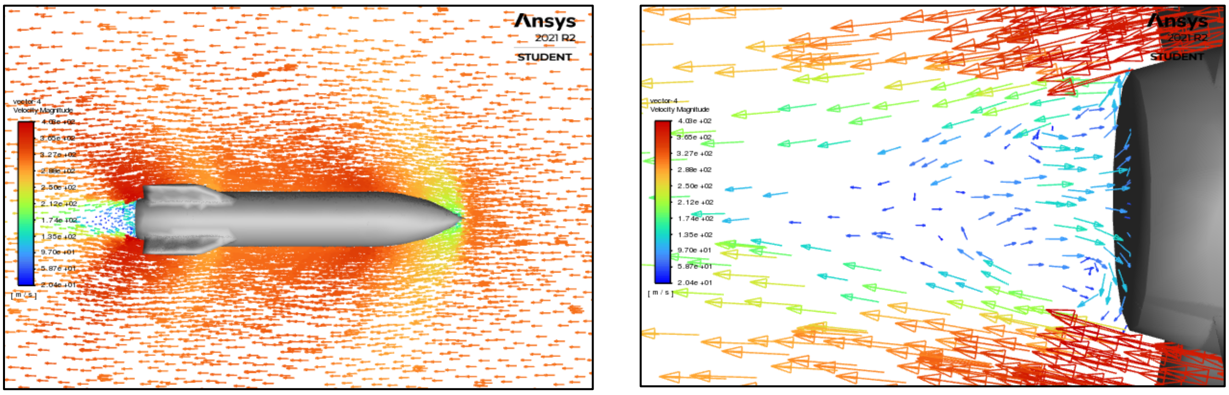

Figure 4.10 Fluid flow velocity vectors for $M = 1.2$

4.1.1 Convergence of Solutions

At this point, a brief discussion about convergence of results shall be considered. **Figure 4.11** shows residuals' evolution with respect to the number of iterations, for a flight condition of $M = 0.95$. Even though continuity does not reach the minimum required value ($< 1e^{-5}$), the overall behaviour and convergence of the rest of residuals can be considered as a positive indicative of the good quality of the solution. A similar behaviour was observed for $M = 1.2$.

Figure 4.12, on the other hand, shows the evolution of the lateral force coefficient C_Y with respect to the number of iterations. Notice that this parameter slightly oscillates around a constant value. This could be another consequence of the recirculating region previously identified. A similar behaviour was found for C_N, C_m and C_n coefficients, for both $M = 0.95$ and $M = 1.2$. Despite this behaviour, it can be considered that convergence is reached. These oscillations, though, disappear if a density-based fluid flow solver is employed.

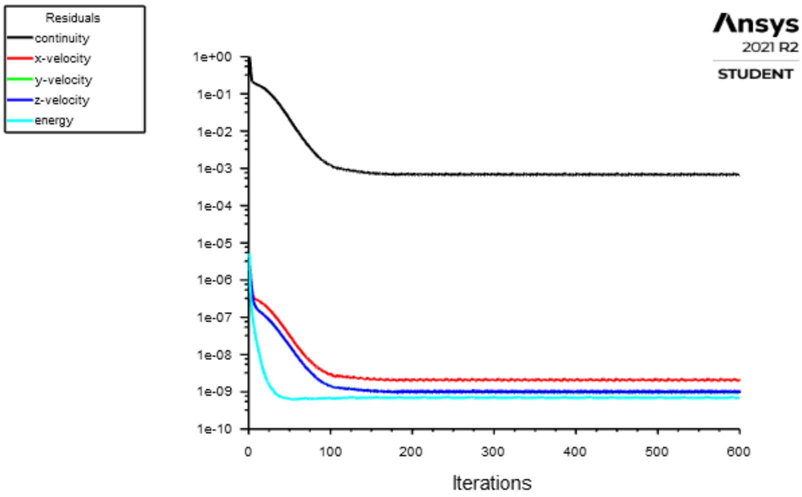

Figure 4.11 Evolution of residuals

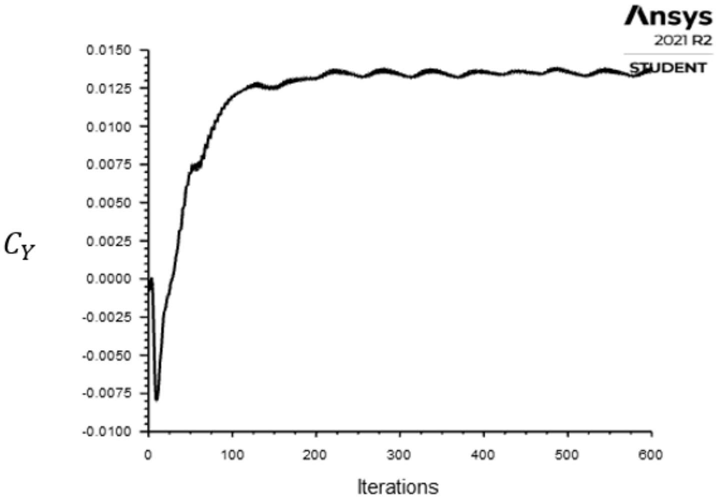

Figure 4.12 Evolution of the lateral force coefficient

Overall, it can be concluded that an inviscid flow solution based on an unstructured grid approach over a generic store in free stream configuration has been correctly validated and it faithfully reproduces the real behaviour of the problem. **Subsection 4.1.2** deals with the viscous approach.

4.1.2 Viscous Analysis

During this subsection, the store in free stream configuration is assessed under viscous considerations. First, it is worth pointing the evolution of the store's force and moment coefficients with respect to the angle of attack α of the free stream. Results are shown in **Figure 4.13** for a nominal grid configuration. Obtained outcomes are compared against experimental data (see asterisk marks) and inviscid simulations (see red lines). Flight condition for each of these simulations is $M = 0.95$.

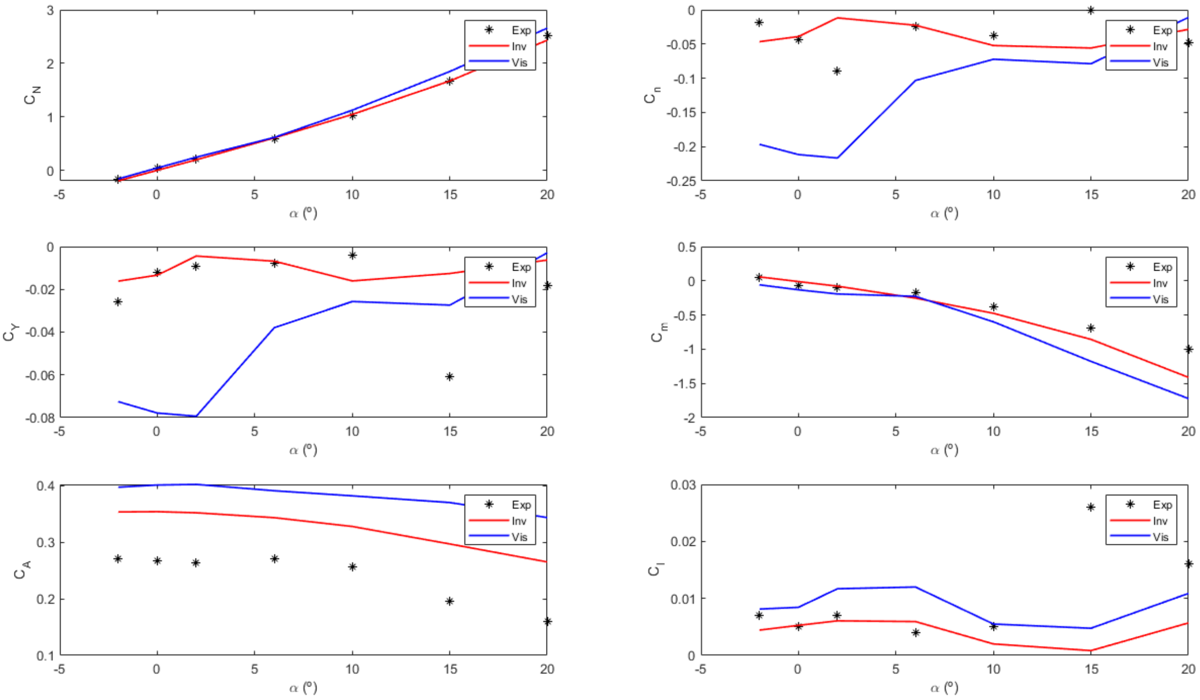

Figure 4.13 Force and moment coefficients for viscous approach

Regarding the aerodynamic force coefficients, it can be noticed that the normal force coefficient C_N is again in quite good agreement with experimental data. Similarly, the axial force coefficient C_A follows the expected behaviour, but this coefficient is oversized by a factor of ~ 1.5 when compared to the experimental data (remember that the inviscid solution was oversized by a factor of ~ 1.3). The main reason behind this issue is the modelling of the aft section of the store. Additionally, viscous effects introduce an additional component in drag (i.e., skin friction drag). All this justifies the origin of the former discrepancy. Finally, it is worth noting that the lateral force coefficient C_Y is worst predicted by the viscous approach (when compared to the inviscid solution). As it will be justified later, the recirculation area in the aft section of the store is more prominent for the viscous approach; subsequently, discrepancies in the C_Y coefficient are more evident.

About the aerodynamic moment coefficients, the rolling moment coefficient C_l is well correlated for almost all the angles of attack. Similarly, the pitching moment coefficient C_m is well predicted. Nevertheless, discrepancies for $\alpha > 10°$ in the former coefficient are more prominent than for the inviscid approach. In contrast with [29], the addition of viscous effects does not seem to improve the accuracy of C_m. Finally, some evident discrepancies were also found for the yawing moment coefficient C_n.

To sum up, aerodynamic force and moment coefficients are in good agreement with experimental data. Nevertheless, the addition of viscous effect does not improve the accuracy of results. On the other hand, as it will be justified later, the computational cost required for a viscous simulation is much higher than for the equivalent inviscid approach. Consequently, viscous simulations are not required to correctly model our problem.

Further conclusions are shown along the rest of this subsection to better understand how viscous effects modify the results for the free stream configuration. In particular, both C_p and Mach contours are shown for an angle of attack of $\alpha = 0°$. **Figure 4.14** and **Figure 4.15** show the results for a flight condition of $M = 0.95$.

Under viscous conditions, the very front section of the store is again characterised by a distribution of high pressures (see **Figure 4.14**). As previously justified, this is clear evidence of the existence of a weak shock wave. Then, an expansion wave is found at the beginning of the cylindrical section of the store. This is characterised by a continuous reduction in the pressure. For the rest of the cylindrical part of the store, both velocity and pressure remain almost constant. The aft part of store is characterised by another expansion wave. All over again, a recirculating region (or turbulent wake) appears behind the aft section of the store (see **Figure 4.18**). Therefore, base drag would be a significant component of the total drag. Finally, the addition of viscous effects produces more abrupt C_p contours than for the equivalent inviscid approach (compare it with **Figure 4.5**).

Regarding Mach contours on store's surface (see **Figure 4.15**), its representation may not seem illustrative at all since velocity contours are almost constant. However, this behaviour is due to the boundary layer. Skin friction causes the velocity in the vicinity of the surface to be smaller than the equivalent inviscid approach. Another difference with the inviscid approach is found in the maximum Mach number achieved in the surroundings of the store: while for the inviscid approach the maximum velocity was $M{\sim}1.45$, for the viscous simulation this value is reduced until $M{\sim}1.32$.

A similar behaviour was found for a flight condition of $M = 1.2$. Both C_p and Mach contours are shown in **Figure 4.16** and **Figure 4.17**, respectively. The maximum Mach number achieved in the surroundings of the store is $M{\sim}1.57$ for the viscous approach, while the maximum value for inviscid approach was $M{\sim}1.66$.

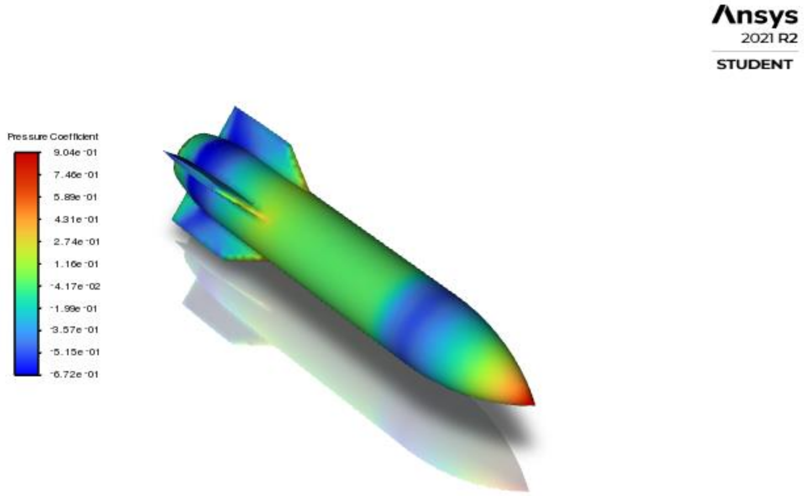

Figure 4.14 C_p contours for $M = 0.95$

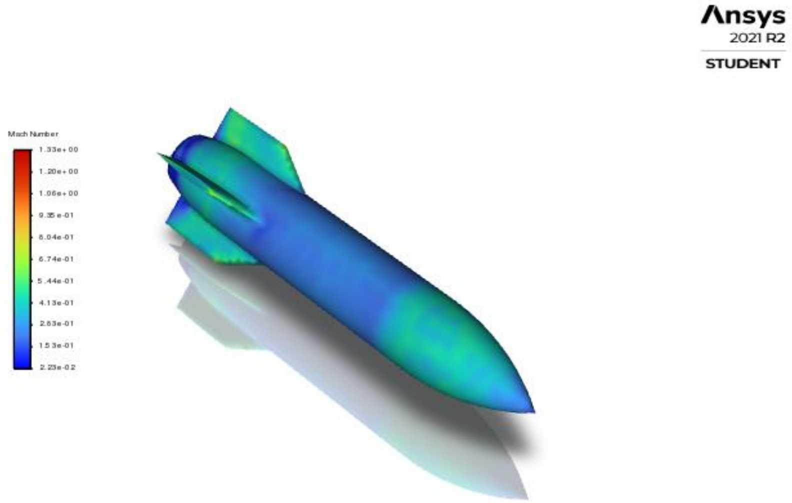

Figure 4.15 Mach contours for $M = 0.95$

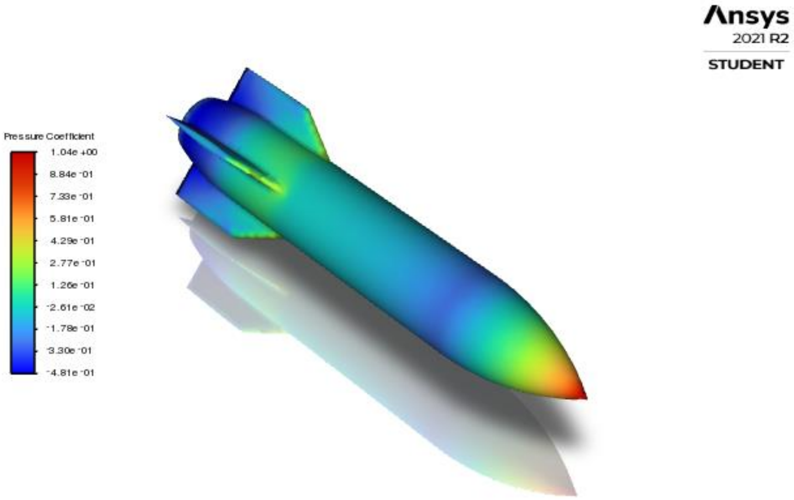

Figure 4.16 C_p contours for $M = 1.2$

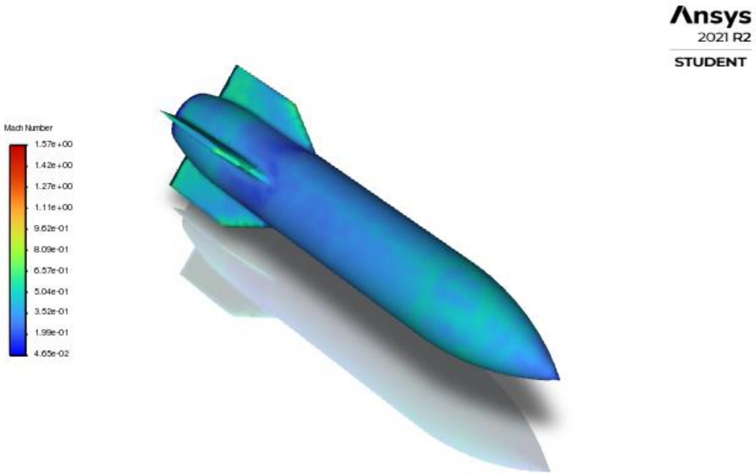

Figure 4.17 Mach contours for $M = 1.2$

Figure 4.18 and **Figure 4.19** represent fluid flow velocity vectors close to the store's surface for $M = 0.95$ and $M = 1.2$, respectively. Notice that the shock wave originated in the very front section of the store can be easily found in the top left-side figures (i.e., blue/green region). Additionally, expansion regions are more clearly identified than for the inviscid approach (see red regions). On the top right-side figures, on the other hand, the recirculating region close to the aft section of the store is identified (notice that this region is more prominent for the viscous approach, because of the skin friction). The growth of the fluid flow velocity within the boundary layer in the cylindrical section of the store is easily identified in the bottom left-side figures. Finally, the bottom right-side figures represent the velocity vectors on the fore section of the store.

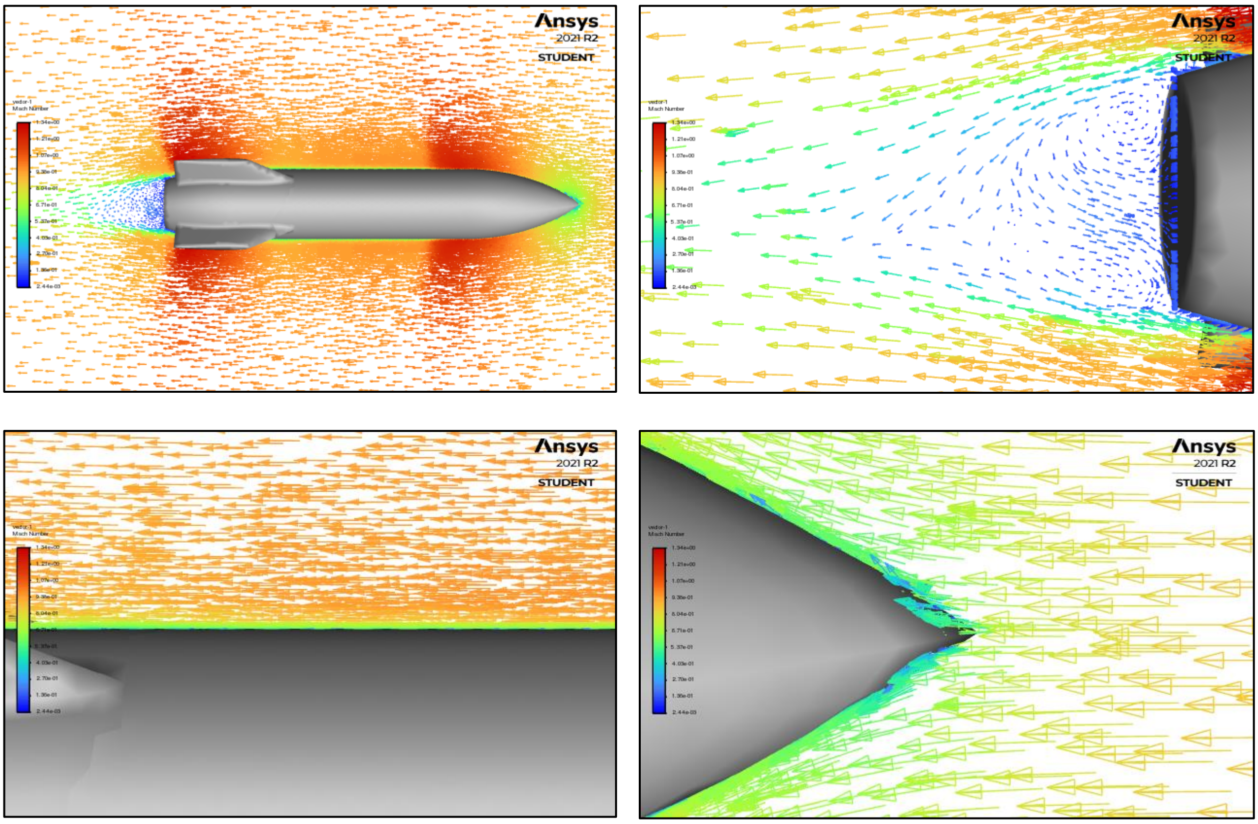

Figure 4.18 Fluid flow velocity vectors for $M = 0.95$

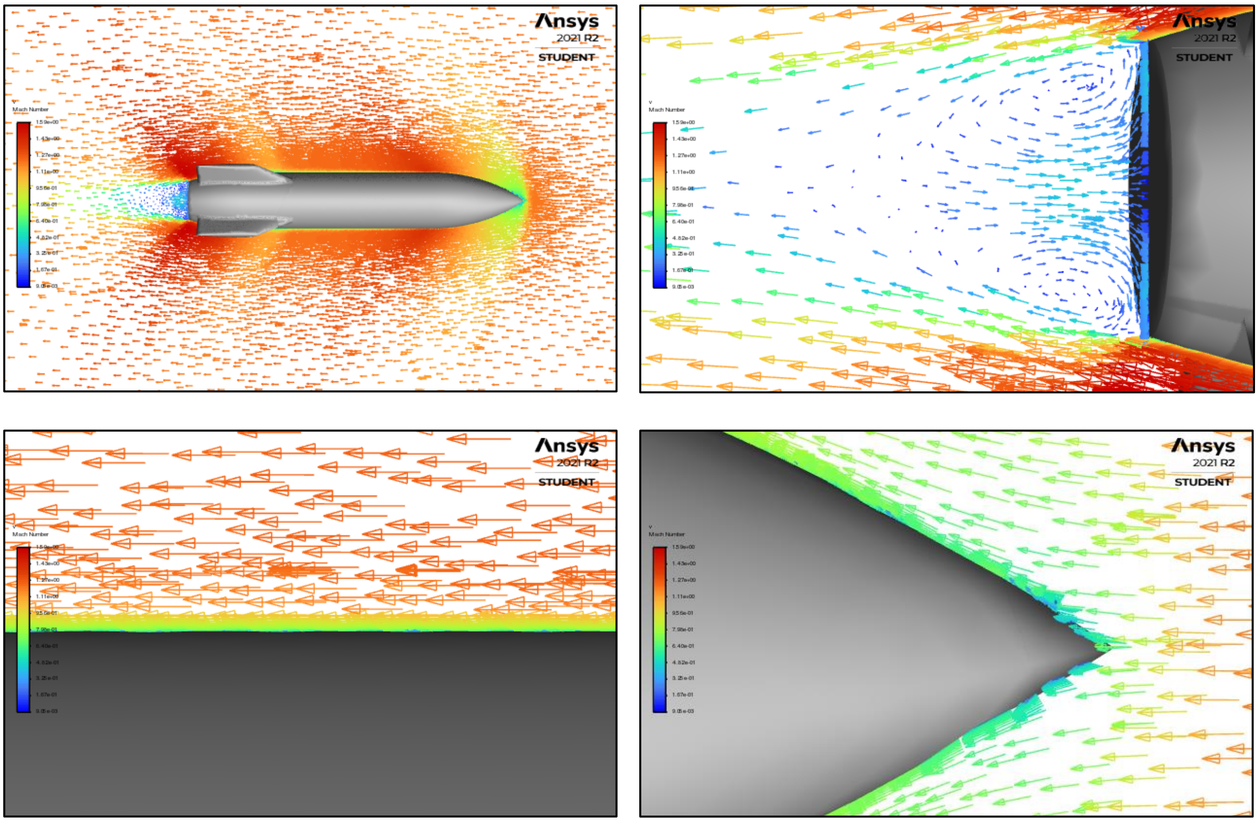

Figure 4.19 Fluid flow velocity vectors for $M = 1.2$

Figure 4.20 and **Figure 4.21** represent velocity contours close to the store for $M = 0.95$ and $M = 1.2$, respectively. On the right-side figures, the evolution of the boundary layer after the first expansion wave is well illustrated.

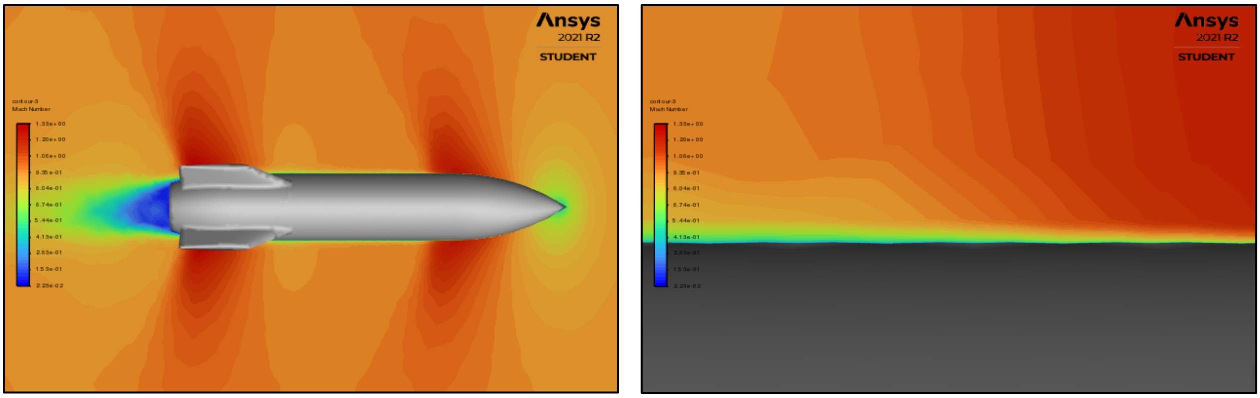

Figure 4.20 Mach contours and boundary layer progression for $M = 0.95$

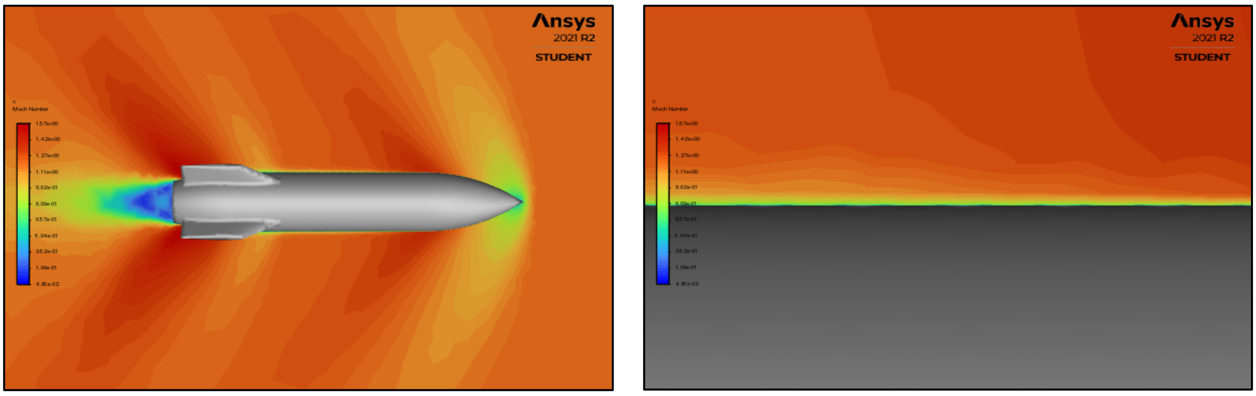

Figure 4.21 Mach contours and boundary layer progression for $M = 1.2$

Finally, **Figure 4.22** and **Figure 4.23** represent the evolution of the tangential Mach (U_x/a_∞), across the boundary layer in the cylindrical section of the store for $M = 0.95$ and $M = 1.2$, respectively. These graphs allow us to validate whether the inflation layers designed in **Chapter 3** were correctly sized. Remember that it must be guaranteed that the velocity boundary layer thickness δ_v is contained within the total height of the inflation layer y_T.

For $M = 0.95$ (see **Figure 4.22**) and $M = 1.2$ (see **Figure 4.23**) the free stream velocity is reached at $y \approx 0.04\, m$. Both values are below the y_T considered to build the total thickness of the inflation layer ($y_T \approx 0.05\, m$, see equation **(3.9)** and **(3.10)**). Consequently, the hypotheses and assumptions applied in **Chapter 3** are valid in this regard.

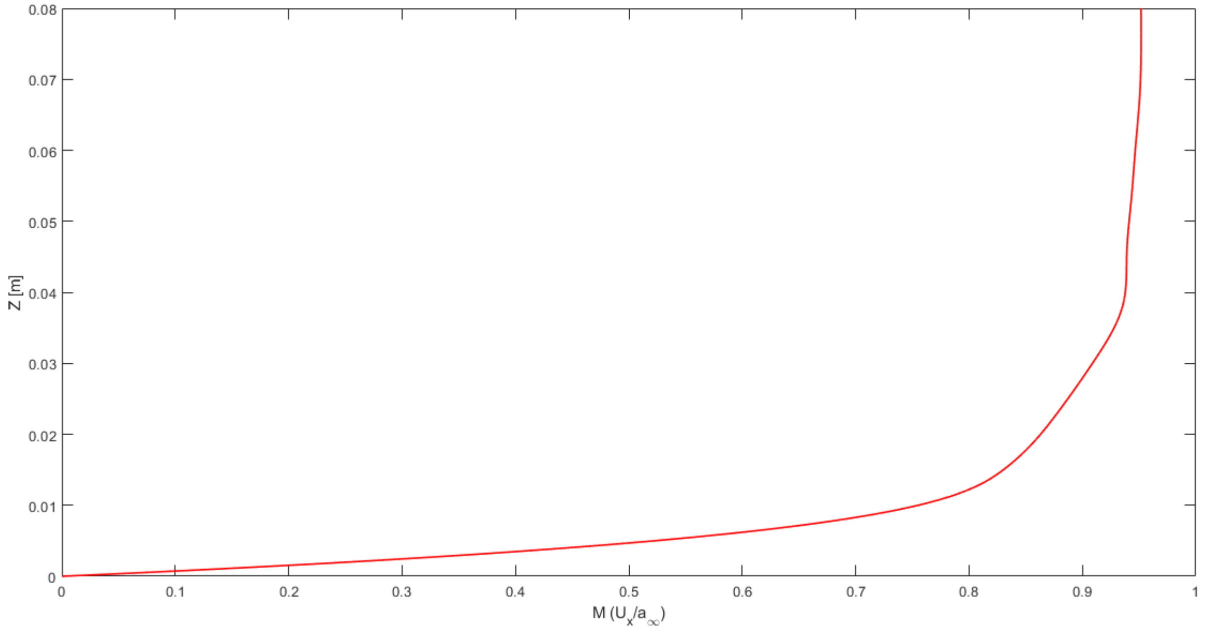

Figure 4.22 Evolution of tangential velocity across the boundary layer for $M = 0.95$

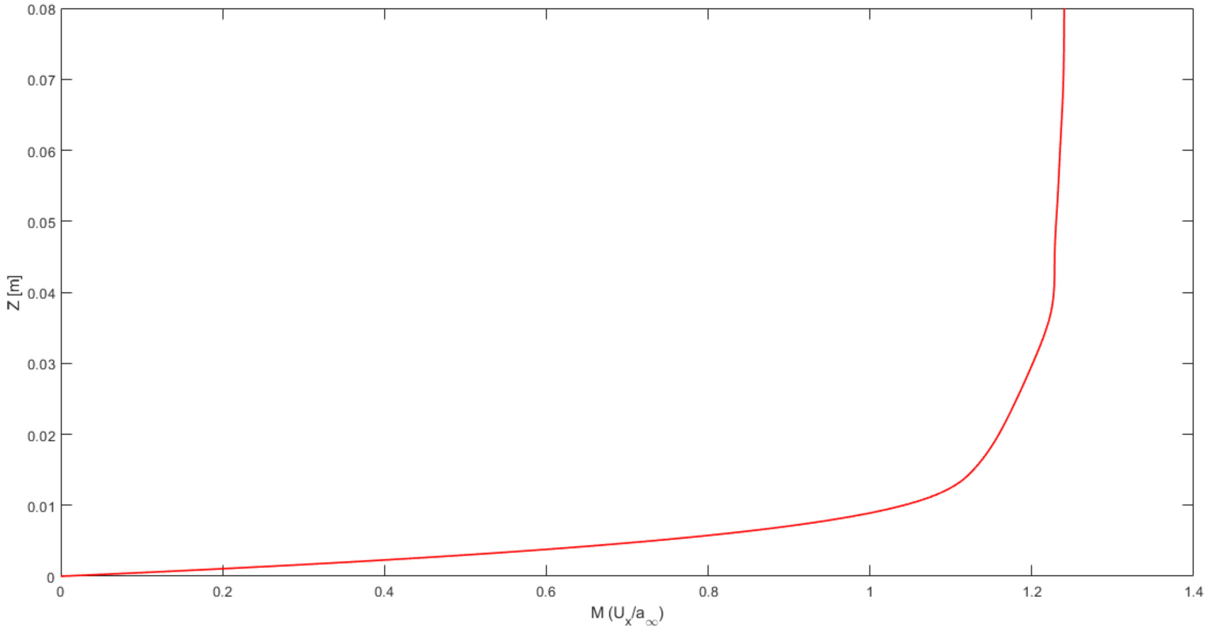

Figure 4.23 Evolution of tangential velocity across the boundary layer for $M = 1.2$

4.1.2.1 Convergence of Solutions

At this point, a brief discussion about convergence of results shall be considered. **Figure 4.24** shows residuals' evolution with respect to the number of iterations, for a flight condition of $M = 0.95$. Even though continuity does not reach the minimum required value ($< 1e^{-5}$), the overall behaviour and convergence of the rest of residuals can be considered as a positive indicative of the good quality of the solution. A much better behaviour was observed for $M = 1.2$; convergence for this flight condition is rapidly reached for all the residuals.

Figure 4.25, on the other hand, shows the evolution of the lateral force coefficient C_Y with respect to the number of iterations, for $M = 0.95$. Again, this parameter slightly oscillates around a constant value. A similar behaviour was found for the C_n coefficient. Despite this behaviour, it can be considered that convergence is reached. However, the number of iterations required to reach convergence is much higher than for the equivalent inviscid simulation. Consequently, viscous simulations are considered to be unnecessary to correctly model our problem. Throughout the rest of this chapter, only inviscid simulations will be assessed for the remaining geometric configurations.

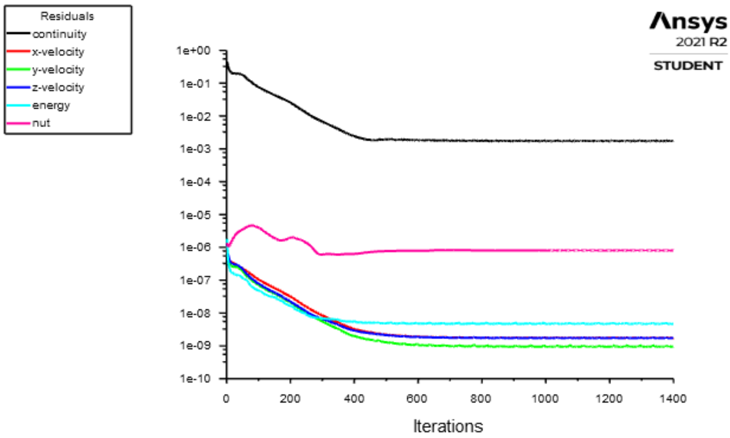

Figure 4.24 Evolution of residuals

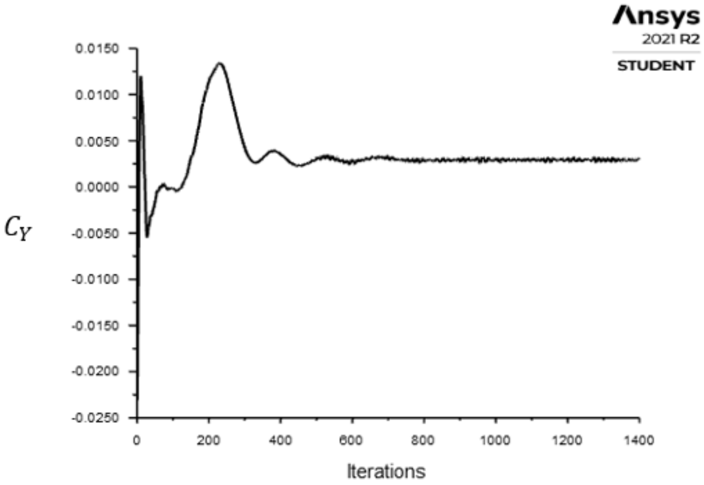

Figure 4.25 Evolution of the lateral force coefficient

4.2 Baseline Configuration

During this section, the designed CFD setup is assessed on a generic pylon/store configuration attached to a clipped delta wing, as previously described in detail in **Chapter 3**. Three different meshes were created for this configuration, based on L_s and L_w parameters. The main aim is to validate an unstructured mesh setup able to provide grid independent solutions. Even though it was concluded that a nominal mesh was sufficient to generate reliable simulations, a more exhaustive justification is displayed along this section.

First, it is worth describing store's force and moment coefficients for a flight condition of $\alpha = 0°$. Results are shown in **Table 4.1** and **Table 4.2** for $M = 0.95$ and $M = 1.2$, respectively. Comparisons are made with experimental data [10], linear-potential results from [3] and [12], and Euler results from [15].

Case	C_N	C_A	C_Y	C_m	C_n	C_l
Experimental [10]	0.644	0.901	-0.954	-1.430	1.520	0.100
Published [3]	1.270	0.936	-0.654	-2.680	0.054	0.024
Published [12]	0.562	0.520	-0.900	-1.538	1.470	0.055
Published [15]	0.687	1.132	-1.036	-1.761	1.791	0.104
Coarse	0.941	1.167	-1.007	-1.910	1.574	0.092
Nominal	0.967	1.188	-1.091	-1.957	1.704	0.096
Fine	0.959	1.130	-1.056	-1.910	1.662	0.088

Table 4.1 Force and moment coefficients for $M = 0.95$

Case	C_N	C_A	C_Y	C_m	C_n	C_l
Experimental [10]	0.520	1.038	-0.531	-1.488	1.200	0.044
Published [3]	0.799	1.240	-1.029	-2.305	1.420	0.055
Published [12]	0.417	0.603	-0.469	-1.418	1.058	0.031
Published [15]	0.537	0.999	-0.540	-1.631	1.296	0.060
Coarse	0.729	1.065	-0.586	-1.715	1.259	0.055
Nominal	0.709	1.051	-0.621	-1.677	1.286	0.053
Fine	0.716	1.034	-0.619	-1.640	1.278	0.053

Table 4.2 Force and moment coefficients for $M = 1.2$

As it can be seen in **Table 4.1** and **Table 4.2**, CFD results for coarse, nominal, and fine approaches are very similar. Therefore, it can be concluded that grid independent solutions were achieved. This strengthens the excellent quality of the designed mesh setup.

For $M = 0.95$ (see **Table 4.1**), CFD results for C_Y, C_l and C_n coefficients are in quite good agreement with experimental data. Notice that some of the obtained parameters are even better than the corresponding published data. However, a subtle discrepancy was found for the C_A coefficient. It must be remembered that the experimental model and the CFD model differed in the aft region of the store, due to the Captative Trajectory Support System. Consequently, CFD results for the former coefficient are larger than the experimental value. This is due to the circulatory region previously identified in **Section 4.1**. Finally, C_N coefficient is clearly oversized with respect to both published and experimental data. The source of this discrepancy may be produced by the small gap considered in the CFD model, between the store and the pylon structure (see **Chapter 3** and **Figure 4.26**).

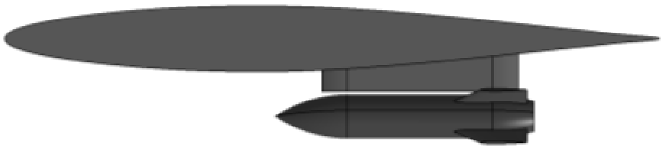

Figure 4.26 Gap between the store and the pylon

This gap causes a suction phenomenon known as Venturi effect. In fluid dynamics, velocity increases as fluid passes through a constriction in accord with the principle of mass continuity. Therefore, static pressure must decrease in accord with the principle of conservation of mechanical energy (i.e., Bernoulli's principle). As a consequence of these low pressures, the normal force on the store increases (and so does the C_N coefficient). This difference, however, mitigates as the store moves away from the pylon (see **Section 4.3**). Further discussions about this phenomenon are displayed along the rest of this chapter. Finally, differences in the C_m coefficient are caused by the C_N discrepancy. Note that this nose-down pitching moment translates into a safe release environment since the store will not collide with the pylon in the event of a perturbation. Similar conclusions can be obtained by analysing **Table 4.2**, for a flight condition of $M = 1.2$.

To sum up, CFD results are, in general, in quite good agreement with both published and experimental data. Even though some differences were observed in various of the force and moment coefficients in the carriage configuration, ejector forces initially dominate the dynamics of the separation problem as the store is rapidly pushed far from the influence of the pylon [7]. Consequently, these discrepancies would have little impact on the final trajectory of the store. On the other hand, it has been justified that mesh setup guarantees grid independent solutions. The remaining discussions throughout this section are shown for a nominal mesh setup.

C_p distributions were evaluated on several sections of the baseline configuration for $M = 0.95$. A detailed pressure coefficient distribution is shown in **Figure 4.27 – Figure 4.36**, where CFD results are compared with experimental data. Some interesting conclusions can be obtained from these figures.

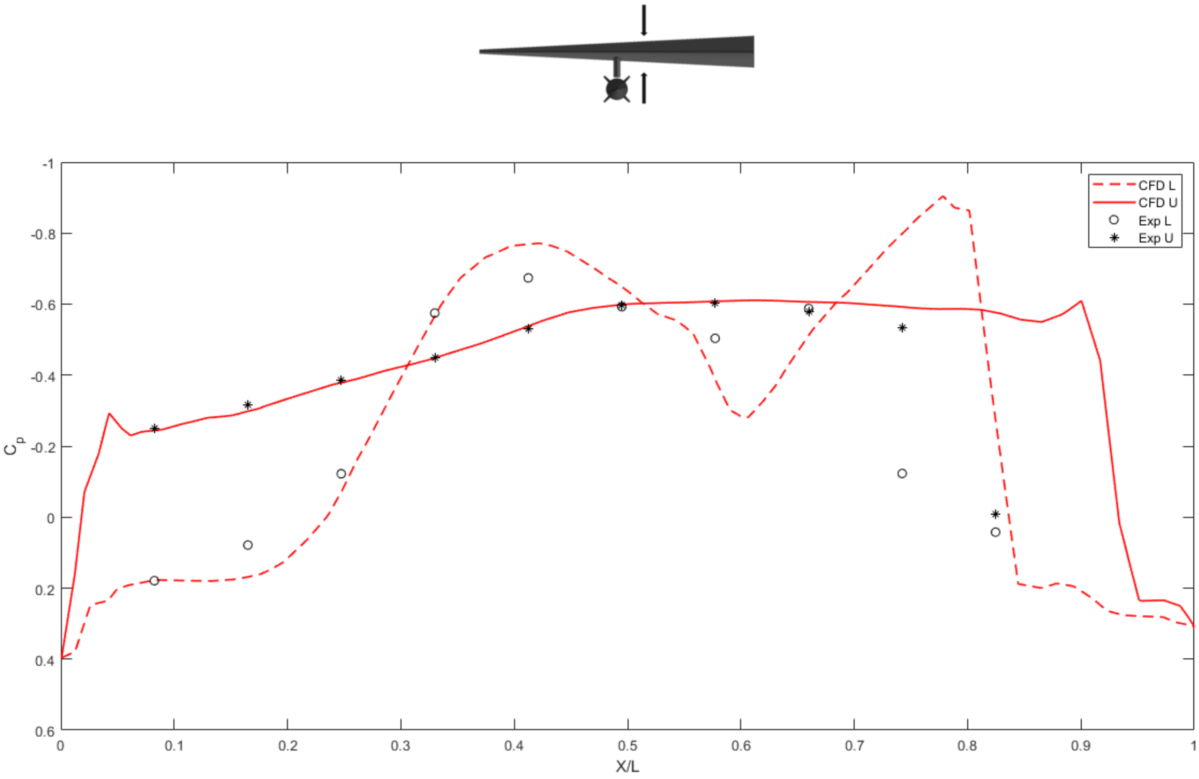

Figure 4.27 C_p comparison for wing at BL 5.3 for $M = 0.95$

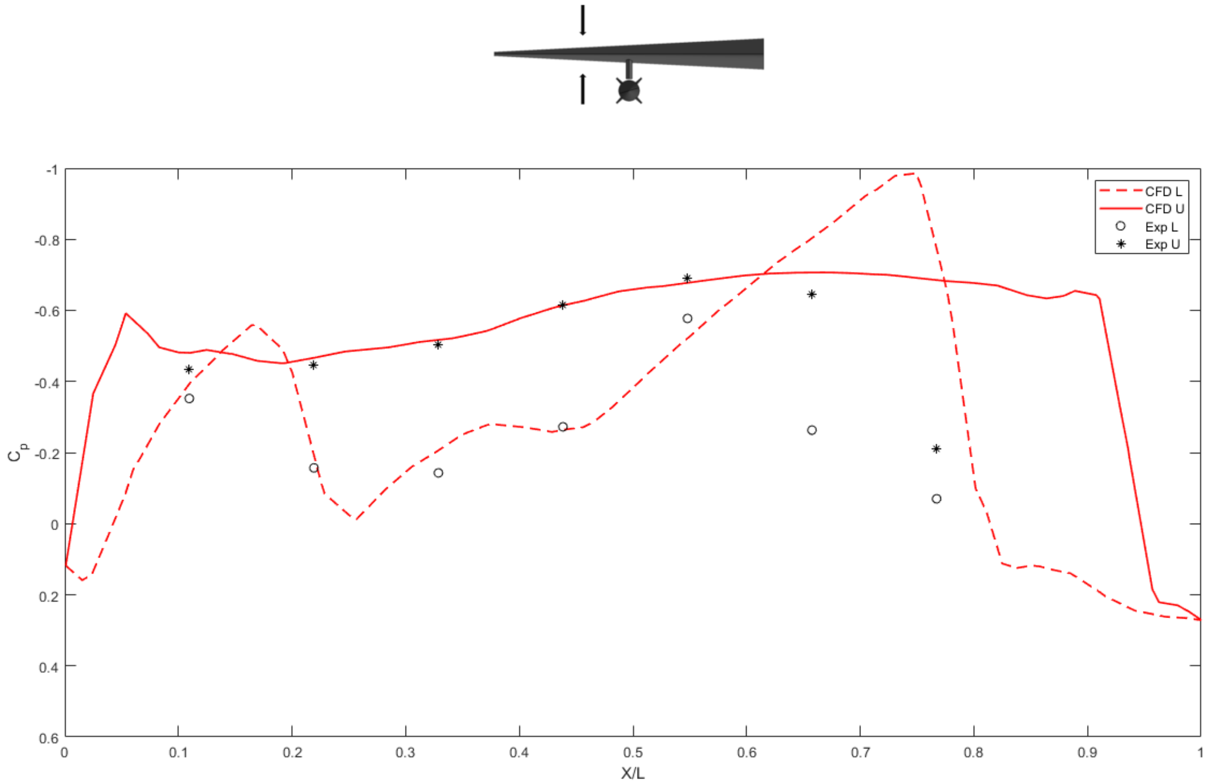

Figure 4.28 C_p comparison for wing at BL 7.7 for $M = 0.95$

Figure 4.27 and **Figure 4.28** compare both CFD and experimental data on the wing along two spanwise sections. The two selected sections (named as BL 5.3 and BL 7.7 in the tunnel test report) correspond to $1.2D$ inboard and outboard of the pylon, respectively. For these figures, U and L refer to wing upper and lower surface, respectively. For the two sections, comparison with experimental data is excellent on both the upper and lower surface up to about 70 percent of the chord.

CFD solutions on the upper surface are in good agreement with experimental data except in predicting the shock location which is detected downstream of that measured by the experiments. The origin of this discrepancy is the inviscid nature of the CFD solution. Indeed, inviscid solutions typically predict shocks 5 to 15 percent downstream of their actual location, according to [12]. Lower surface comparisons are again in good agreement with experimental data until a strong shock is encountered at about 80 percent of the chord. An assessment of the surface Mach contours in the CFD simulation show a strong expansion close to the aft region of the pylon which propagates both inboard and outboard along the wing (see **Figure 4.39**). This causes the overpredicted shock strength in the lower surface of both sections of the wing. On the other hand, a weak shock is observed for BL 5.3 at about 40 percent of the chord, whereas a strong shock is found for BL 7.7 at about 20 percent of the chord. This is another consequence of the interference introduced by the pylon.

Finally, the pressure distribution on the upper surface is similar for the two sections showing essentially no aerodynamic interferences, while on the lower surface the interference effect produced by the store and the pylon is evident in both sections of the wing.

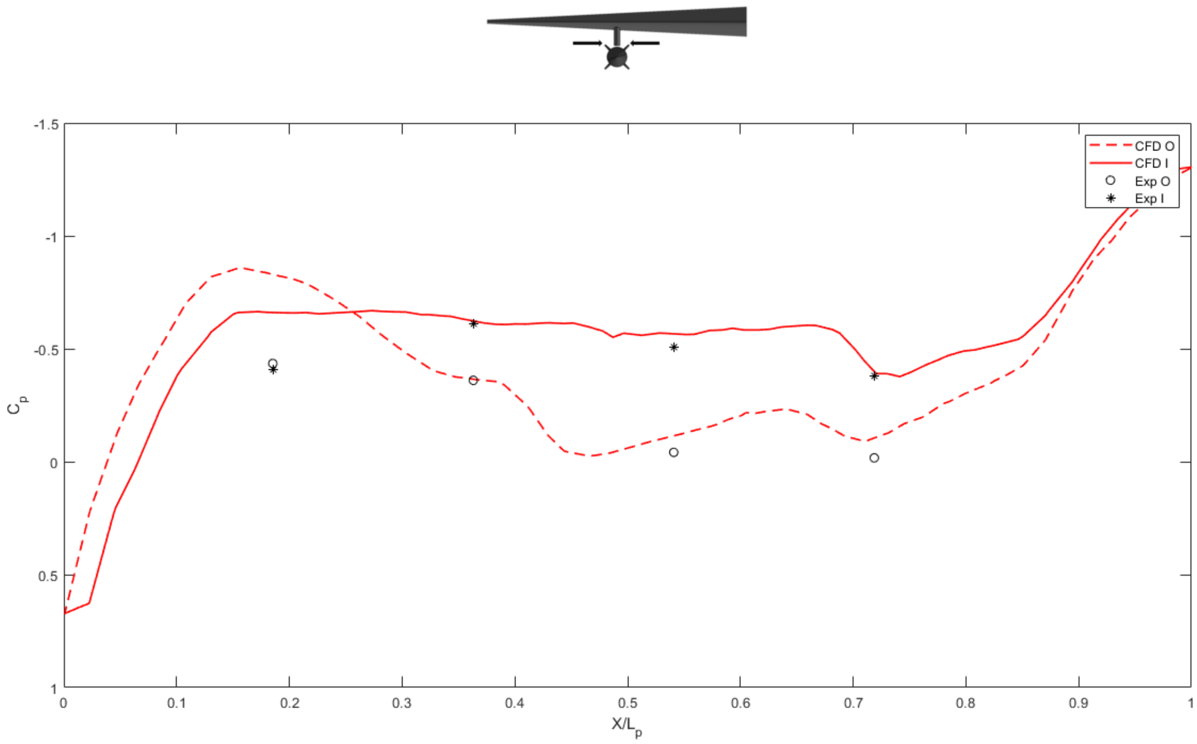

Figure 4.29 C_p comparison for pylon at lower row for $M = 0.95$

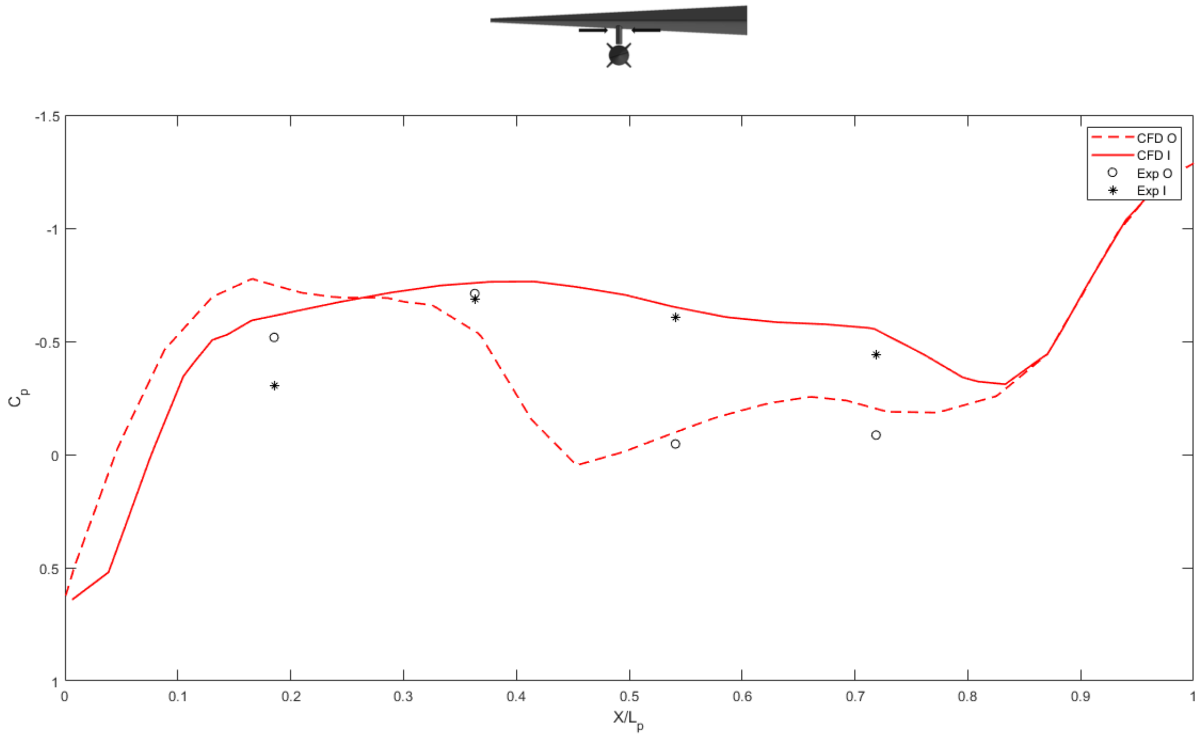

Figure 4.30 C_p comparison for pylon at upper row for $M = 0.95$

Figure 4.29 and **Figure 4.30** compare CFD and experimental data on the pylon along two different sections. For these figures, O and I refer to outboard and inboard surface, respectively. For the two cases, comparison with experimental data is excellent on both surfaces of the pylon. Nonetheless, CFD simulation predicts a more pronounced expansion in the leading edge of the pylon. On the other hand, there is an additional expansion in the proximity of the pylon's trailing edge. Remember that an assessment of the surface Mach contours in the CFD simulation show a strong expansion over the aft region of the pylon which propagates both inboard and outboard along the wing (see **Figure 4.39**).

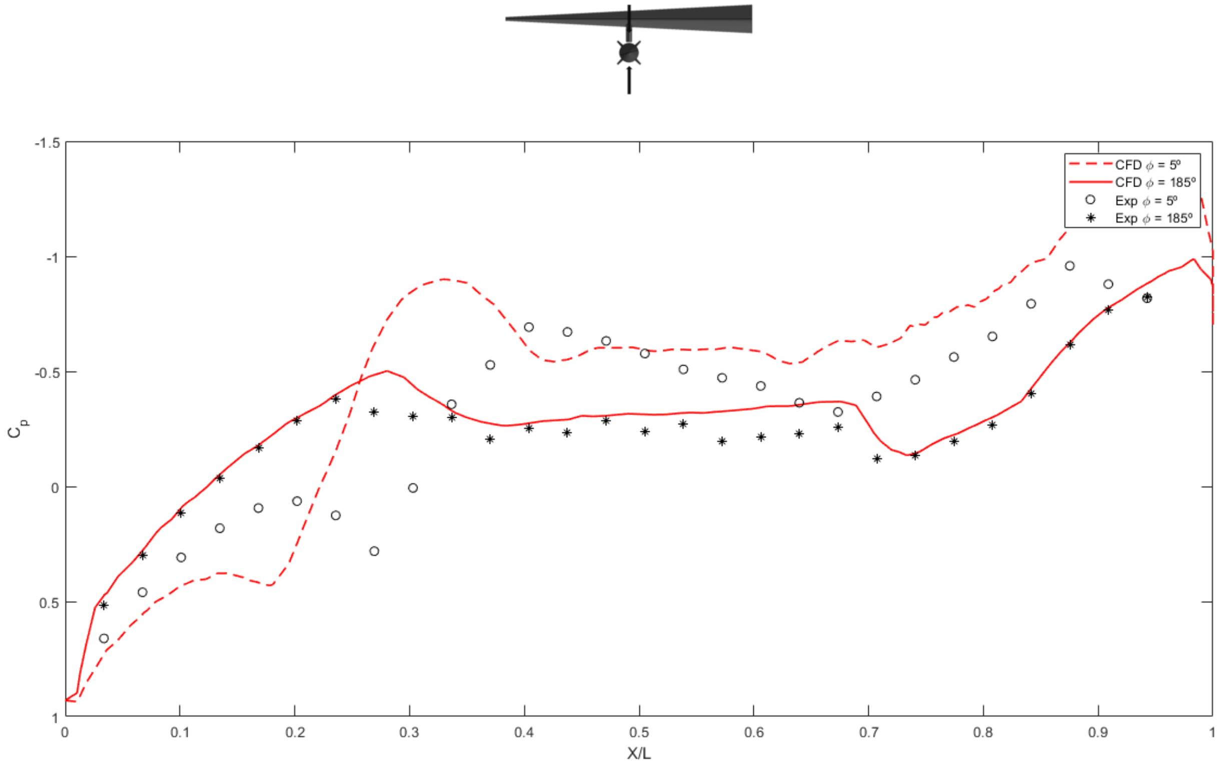

Figure 4.31 C_p comparison for store at $\phi = 5°$ and $\phi = 185°$ for $M = 0.95$

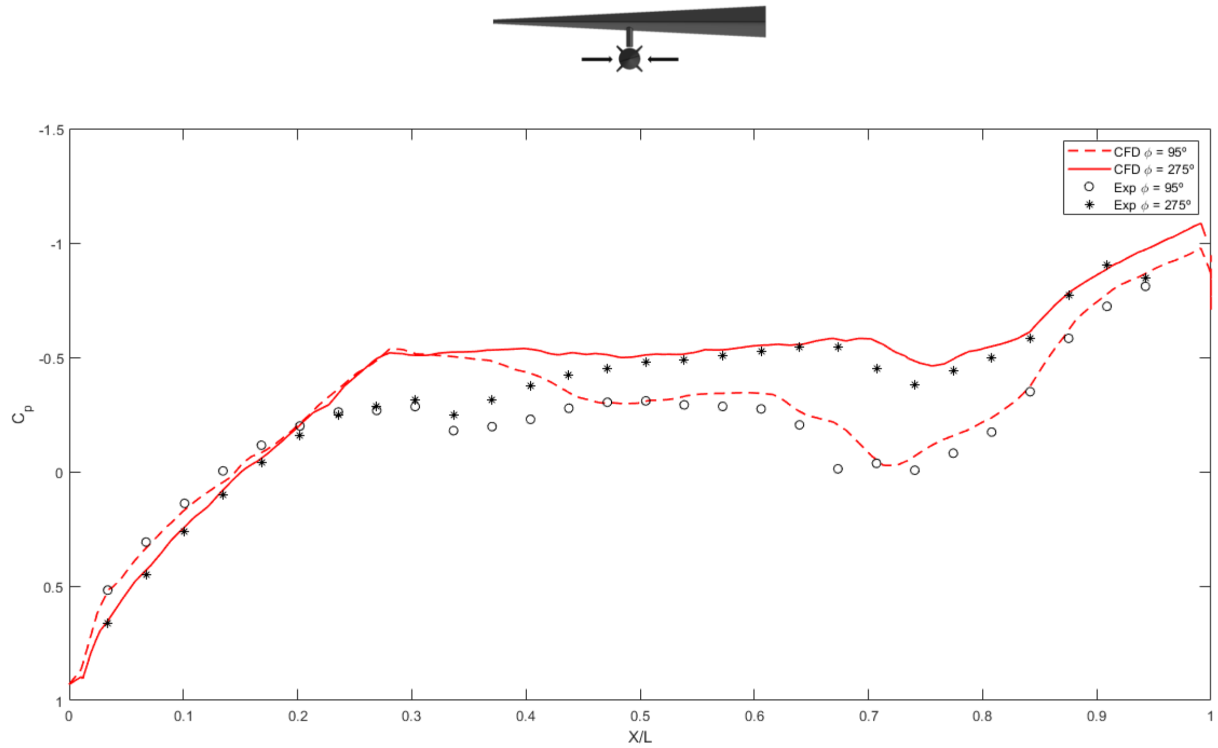

Figure 4.32 C_p comparison for store at $\phi = 95°$ and $\phi = 275°$ for $M = 0.95$

Figure 4.31 and **Figure 4.32** show C_p comparison on the store. Results are presented along four streamwise rays from the nose to the tail of the store. The location for each ray is defined by the circumferential angle ϕ, which is defined positive clockwise from the pylon centre looking downstream. **Figure 4.31** contains data at rays along the top and the bottom of the store at $\phi = 5°$ and $\phi = 185°$, respectively. **Figure 4.32**, on the other hand, shows C_p comparisons along the inboard and outboard rays at $\phi = 95°$ and $\phi = 275°$, respectively.

In general, CFD results compare very well with experimental data. Nevertheless, it must be mentioned that along the $\phi = 5°$ ray, which passes through the gap, some substantial discrepancies were found. In particular, CFD approach misses the small shock at about 28 percent of the chord. On the other hand, some differences appear in the aft region of the store (at about 90 percent of the total length). These discrepancies are attributable to the difference in modelling the aft end of the store and the aerodynamic interference produced by the gap. Finally, the CFD simulation predicts a flow expansion in the front side of the store larger than the expected by the experimental analysis.

Overall, in all four sections of the store the general trends are captured qualitatively, and the shock strengths and locations are reasonable considering the inviscid nature of the CFD fluid flow solver. Finally, it is worth mentioning that pressure on the inboard side of the store ($\phi = 95°$) is greater than the pressure on the outboard side of the store ($\phi = 275°$). This is produced by a cross flow due to the sweep of the wing. This greater pressure on the inboard side of the store is more pronounced in the mid region of the store and will exert a strong force pulling the store away from the fuselage if the store were to be released from the aircraft, generating a safe release.

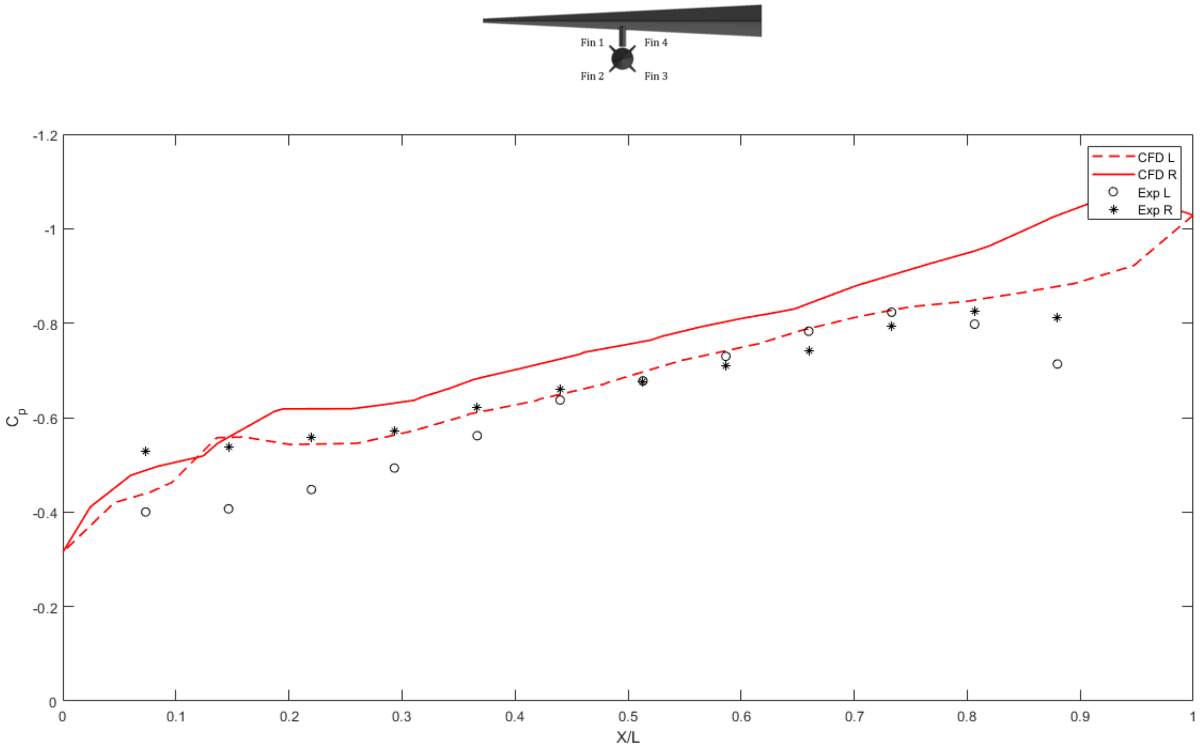

Figure 4.33 C_p comparison for fin 1 for $M = 0.95$

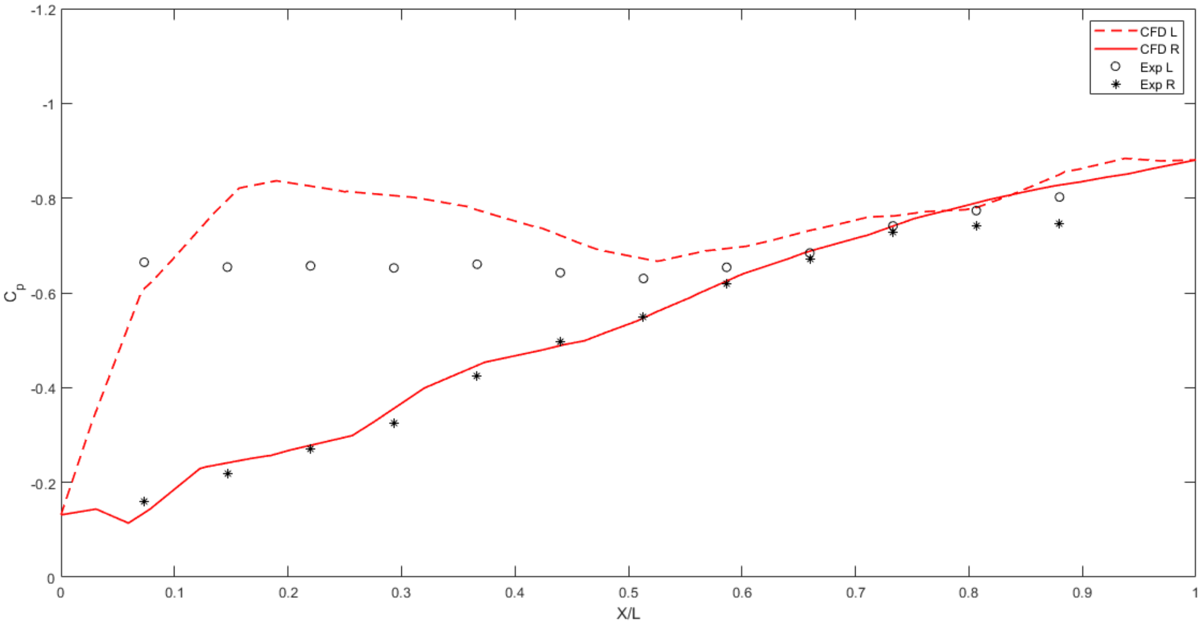

Figure 4.34 C_p comparison for fin 2 for $M = 0.95$

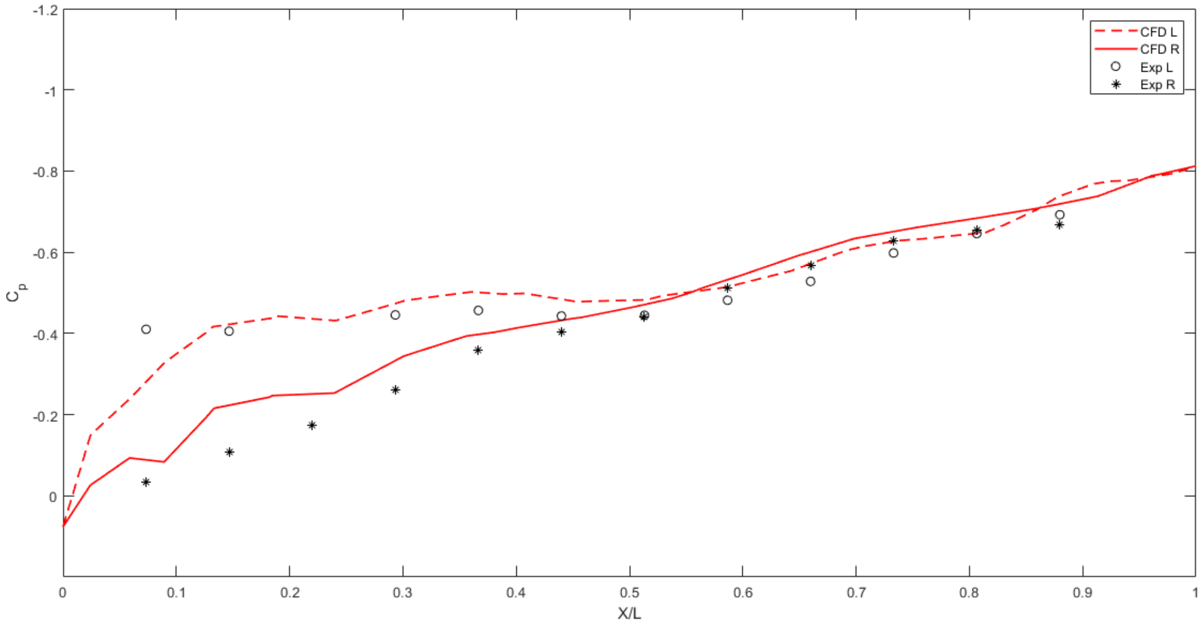

Figure 4.35 C_p comparison for fin 3 for $M = 0.95$

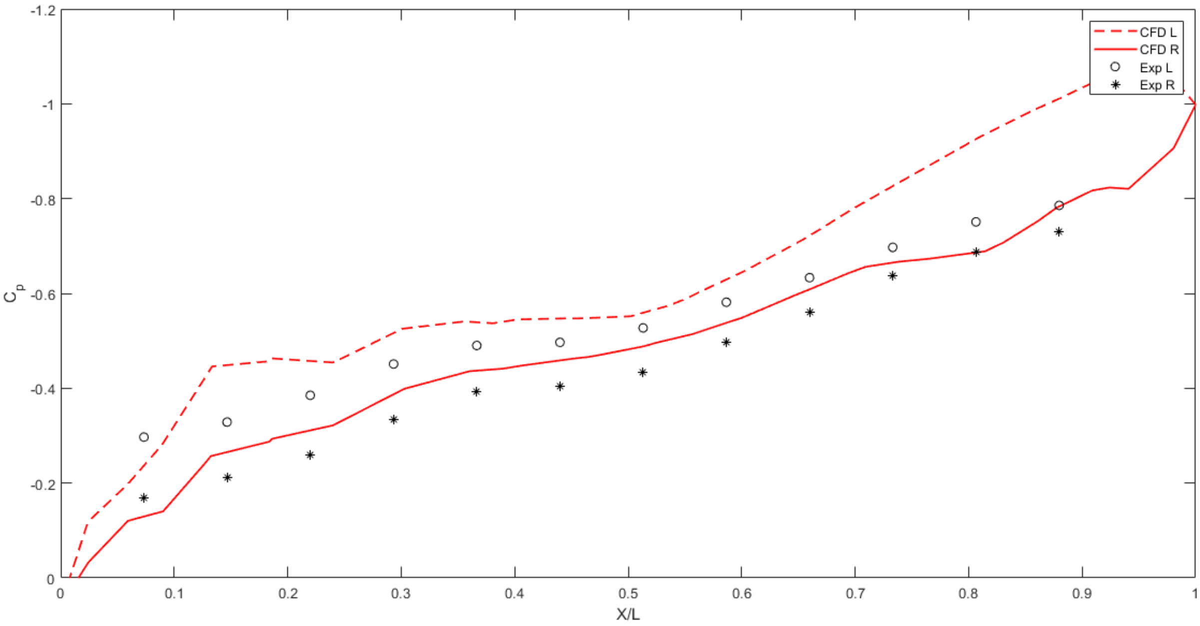

Figure 4.36 C_p comparison for fin 4 for $M = 0.95$

Finally, **Figure 4.33 – Figure 4.36** show comparison with experimental data on the fins. The selected sections are approximately midway of the fin span. For these figures, L and R refer to the observer's left and right side of the fin, respectively, when viewed from the store looking downstream. The overall agreement with experimental data is acceptable. However, some relevant discrepancies were found for fin 1 and fin 4 as those surfaces are close to the gap.

After these analyses, it can be concluded that the gap between the pylon and the store introduces some relevant perturbations with respect to the experimental data. It is possible that a better simulation of this effect shall include boundary layer and shock-boundary layer effects.

Further conclusions are shown along the rest of this section to better understand the physics behind our problem. In particular, both C_p and Mach contours on both the wing and the store are shown for an angle of attack of $\alpha = 0°$. **Figure 4.37 - Figure 4.40** show the results for a flight condition of $M = 0.95$ while **Figure 4.41 - Figure 4.44** show the results for $M = 1.2$. Comparisons with published data are also displayed.

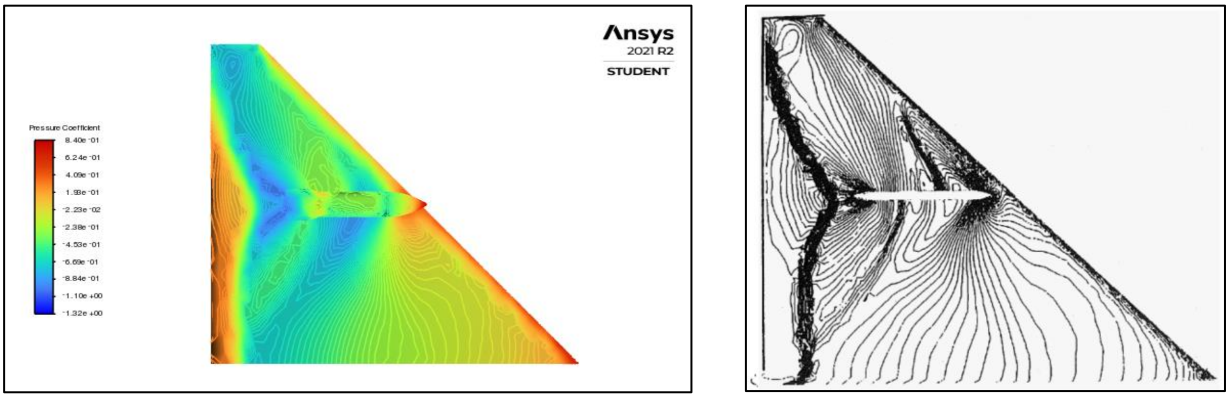

Figure 4.37 C_p contours on the lower surface of the wing for $M = 0.95$

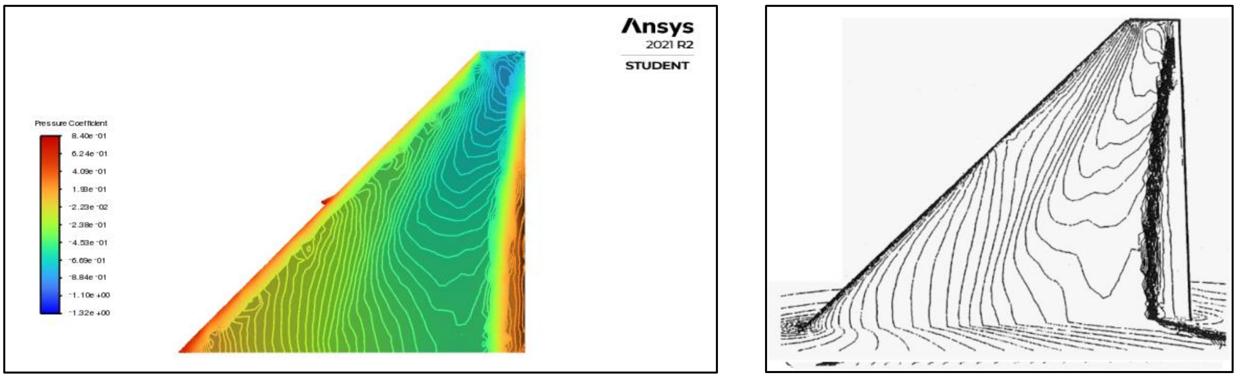

Figure 4.38 C_p contours on the upper surface of the wing for $M = 0.95$

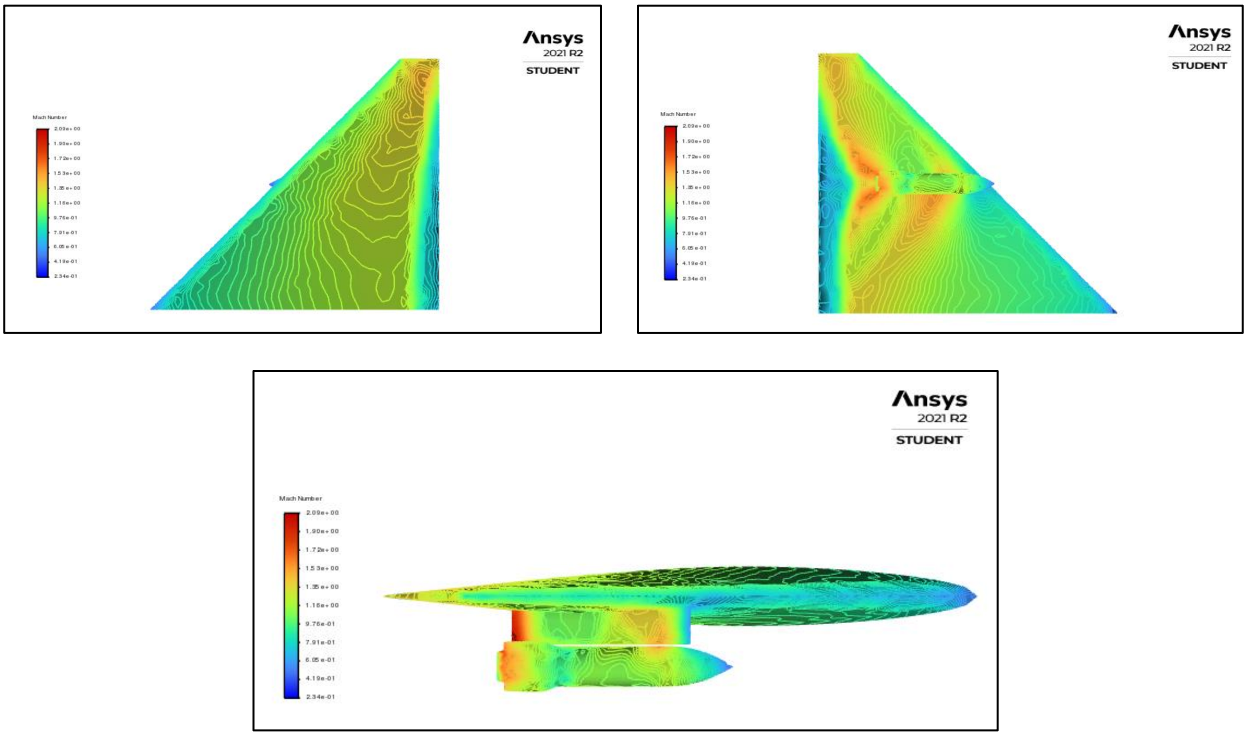

Figure 4.39 Mach contours on the wing for $M = 0.95$

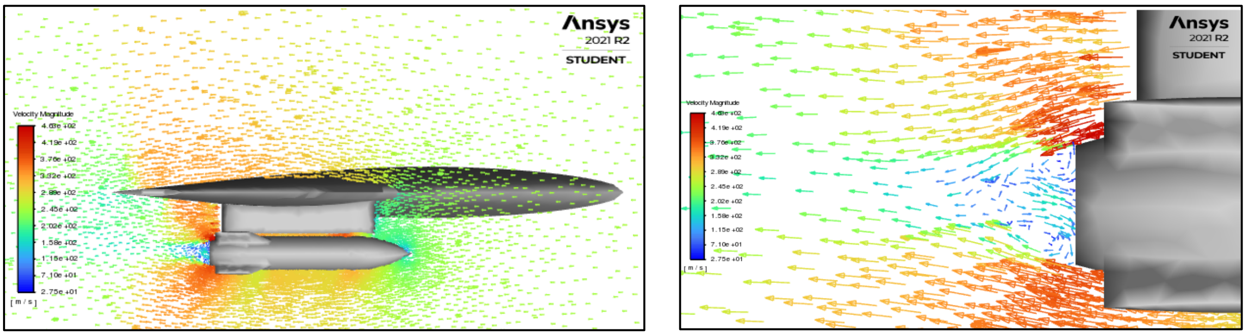

Figure 4.40 Fluid flow velocity vectors for $M = 0.95$

Figure 4.37 shows contours of C_p on the lower surface of the wing and the store, whereas **Figure 4.38** shows these contours on the upper surface of the wing. On the upper surface, the flow expands continuously up to about 90 percent of the chord where a shock takes place. The flow on the lower surface has a large interference effect due to the presence of the pylon and the store. The asymmetry caused by the cross flow of the wing is also evident in the C_p contours on the lower surface around the pylon. Finally, CFD contours are qualitatively similar to published data from [15] (see right-side of **Figure 4.37** and **Figure 4.38**), in both the upper and lower surface of the wing. Notice that published data only include C_p contours on the wing since the store and the pylon are removed for clarity.

Figure 4.39 illustrates the complex flow field (in terms of Mach contours) on the wing and the store during the carriage configuration. Two shocks develop on the fore section of the pylon and the store (see blue region). Two expansion waves are found on either side of the aft sections of the pylon (see red region). Note that there is a mutual interference between the store and the pylon, where numerous shocks are visible on the store. **Figure 4.39** also illustrates the shock created in the trailing edge of the wing (blue region).

Finally, **Figure 4.40** represents fluid flow velocity vectors projected in the symmetry plane of the pylon. Notice that the weak shock originated in the very front section of the store can be easily found in the left-side figure (see blue region). On the right-side figure, on the other hand, the recirculating region close to the aft region of the store is identified. This region is weaker than the recirculating region in the free stream configuration since there is an injection of velocity produced by the gap between the store and the pylon. The acceleration in the fluid flow by the end of the gap is a consequence of the Venturi effect. This figure reinforces some of the conclusions displayed within this section.

Similar conclusions can be obtained for $M = 1.2$. **Figure 4.41** and **Figure 4.42** show C_p contours on the wing and the store. On the upper surface, **Figure 4.42**, a shock-less flow exists this time. On the lower surface, **Figure 4.41**, a strong interference, created by the presence of the store and the pylon, can be recognised. C_p contours are qualitatively similar to the published data [15] (right-side of **Figure 4.41** and **Figure 4.42**), in both the upper and lower surface of the wing. On the other hand, the effects of the shocks in the nose and the aft region of the store, and the asymmetry due to the cross flow of the wing are also evident in **Figure 4.43**. Finally, the shock wave in the trailing edge is less strong compared to the transonic case, and also affects a smaller portion of the wing.

Finally, **Figure 4.44** represents fluid flow velocity vectors projected in the symmetry plane of the pylon. Notice that the weak shock originated in the very front section of the store can be easily found in the left-side figure (see blue region). On the right-side figure, on the other hand, the recirculating region close to the aft region of the store is identified. This region is weaker than the recirculating region in the free stream configuration since there is an injection of velocity produced by the gap. Again, the acceleration in the fluid flow in the vicinity of the end of the gap is a consequence of the Venturi effect.

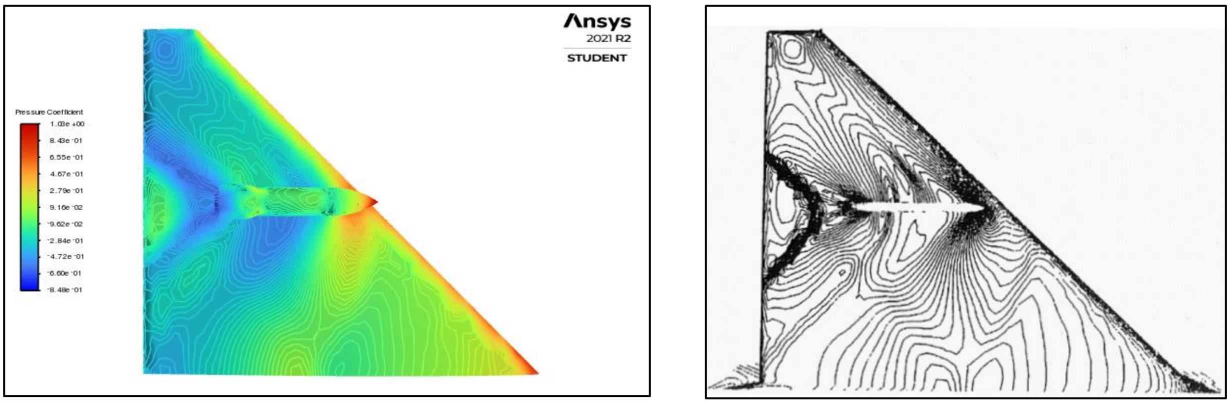

Figure 4.41 C_p contours on the lower surface of the wing for $M = 1.2$

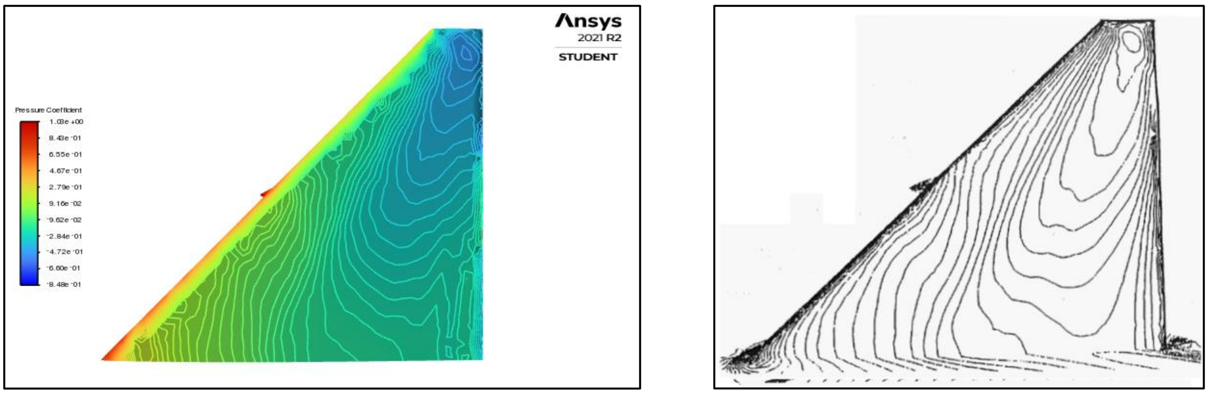

Figure 4.42 C_p contours on the upper surface of the wing for $M = 1.2$

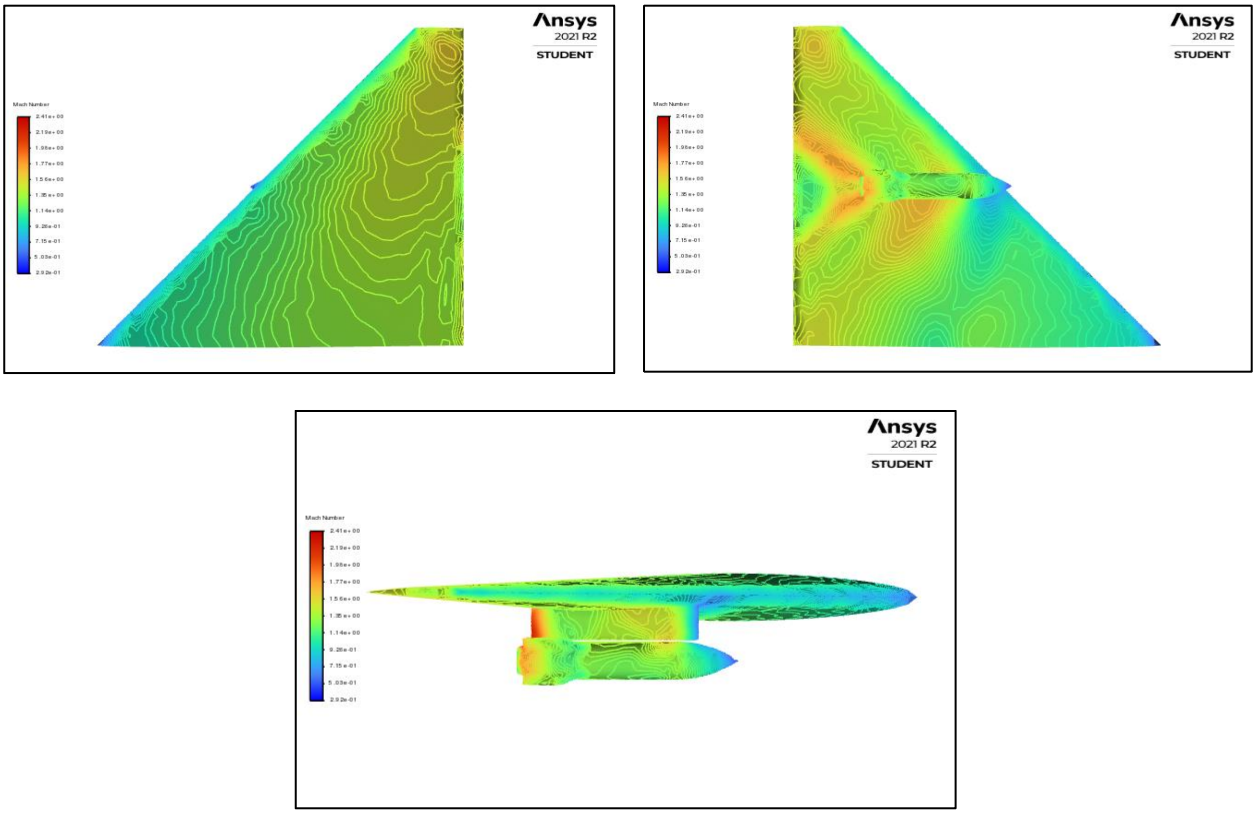

Figure 4.43 Mach contours on the wing for $M = 1.2$

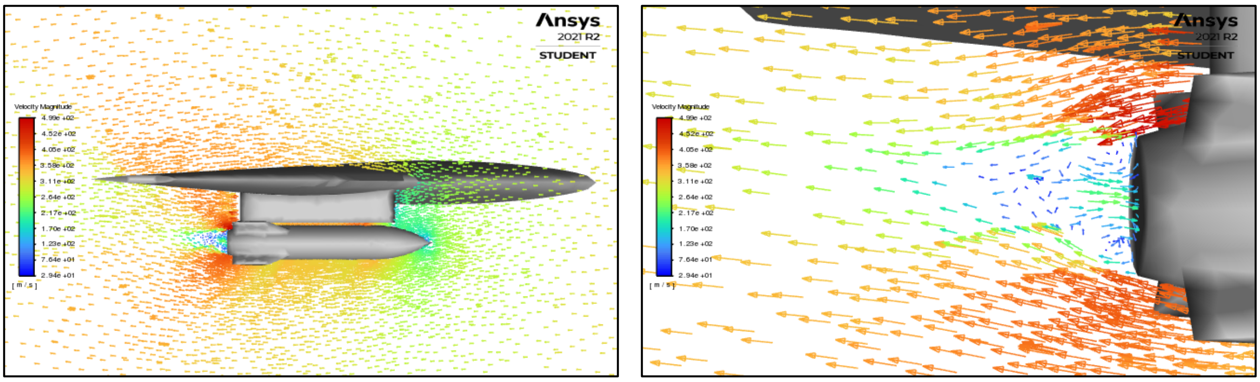

Figure 4.44 Fluid flow velocity vectors for $M = 1.2$

Throughout this section, it has been demonstrated how complicated is the fluid flow around the baseline configuration. Several aerodynamic interferences were identified among the bodies that conform the model. Nevertheless, it is evident that CFD simulations are in good agreement with both published and experimental data.

4.2.1 Convergence of Solutions

At this point, a brief discussion about convergence of results shall be considered. **Figure 4.45** shows residuals' evolution with respect to the number of iterations, for a flight condition of $M = 0.95$. Even though continuity does not reach the minimum required value ($< 1e^{-5}$), the overall behaviour and convergence of the rest of residuals can be considered as a positive indicative of the good quality of the solution. A similar behaviour was observed for $M = 1.2$.

Figure 4.46, on the other hand, shows the evolution of the lateral force coefficient C_Y with respect to the number of iterations. Notice that this time there are no oscillations in its value as happened in the free stream configuration. The same behaviour was noticed for the rest of the force and moment coefficients, for both $M = 0.95$ and $M = 1.2$. This reinforces the statement that the effect of the recirculation is reduced by the injection of velocity produced by the gap.

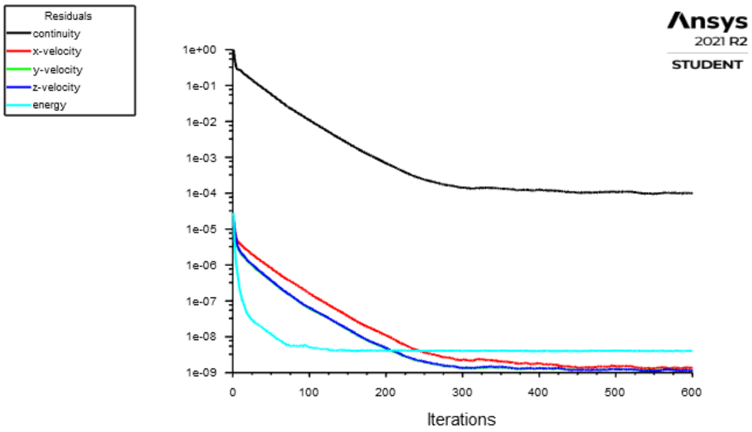

Figure 4.45 Evolution of residuals

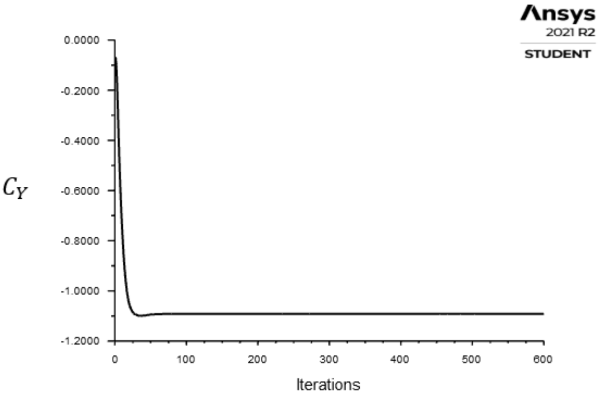

Figure 4.46 Evolution of the lateral force coefficient

Overall, it can be concluded that an inviscid flow solution based on an unstructured grid approach over the baseline configuration has been accurately validated and it faithfully reproduces the real behaviour of the problem. In **Section 4.3**, two translations of the store around the carriage position are be assessed.

4.3 Store Translated in Two Positions

As stated in **Chapter 1**, several configurations of the geometric model shall be assessed to correctly validate the final CFD setup. To achieve that, the full store/wing/pylon model is evaluated with the store translated in two different positions. These locations, representative of an intermediate (near) and the farthest position (far) when the store is released from aircraft, were previously defined in **Chapter 3** by means of their translations and rotations with respect to the store's centre of gravity while in carriage position.

Validation against experimental data is another crucial requirement. It must be remembered from **Chapter 2** that experimental trajectory propagations summarised in [10] were computed based on a quasi-steady approximation, in which steady flow at sample points along the store trajectory is used to derive loads. This feature allows to simulate intermediate positions of the store and compare those CFD results with experimental data. Experimental report, however, only includes force and moment coefficients for each of the aforementioned positions. Consequently, comparisons such as C_p contours are not available this time.

First, it is worth assessing store's force and moment coefficients by comparing CFD results against experimental data. Results are shown in **Table 4.3** and **Table 4.4** for near and far position, respectively. Flight condition for each of these simulations is $\alpha = 0°$ and $M = 0.95$ (N.B.: experimental data was only available for this particular flight condition). As demonstrated earlier during this chapter, the designed mesh setup guarantees grid independent solutions. Therefore, only the nominal mesh configuration is employed throughout this section.

Case	C_N	C_A	C_Y	C_m	C_n	C_l
Experimental [10]	1.147	0.872	0.146	−1.408	0.444	0.007
CFD	1.236	0.986	0.159	−1.597	0.368	0.012

Table 4.3 Force and moment coefficients for near position

Case	C_N	C_A	C_Y	C_m	C_n	C_l
Experimental [10]	0.955	0.831	1.201	-1.312	0.385	-0.005
CFD	0.858	0.859	1.242	-1.232	0.569	-0.059

Table 4.4 Force and moment coefficients for far position

For the near position (see **Table 4.3**), the C_Y coefficient is in quite good agreement with experimental data. On the other hand, a subtle discrepancy was found for the C_A, C_l and C_n coefficients. It must be remembered that the experimental model and the CFD model differed in the aft region of the store, due to the Captative Trajectory Support System. Consequently, CFD results for the former coefficients are different. Finally, discrepancies on C_N and C_m coefficients diminish as soon as the store moves away from the pylon. This means that the aerodynamic interference introduced by the gap is only relevant during the carriage configuration. Similar conclusions can be obtained by analysing **Table 4.4**, for the far position. In this case, discrepancies in the C_N and C_m almost disappear. However, it is worth pointing that both C_n and C_l are poorly predicted by the CDF simulation. At this angle of incidence, viscous effects become prominent and both vortex formation and flow separation take place in the close region of the store.

To sum up, CFD results are in quite good agreement with experimental data, even though slight differences were observed in some of the force and moment coefficients. These discrepancies, however, were found to have a little impact on the final trajectory of the store, according to literature review. Therefore, an inviscid approach is accurate enough to correctly represent the behaviour of the problem.

Further conclusions are shown along the rest of this section to better understand the physics behind our problem. In particular, C_p contours, Mach contours, and fluid flow velocity vectors are shown for each of the two positions. **Figure 4.47 - Figure 4.49** show the results for the near position while **Figure 4.50 - Figure 4.52** show the results for the far position.

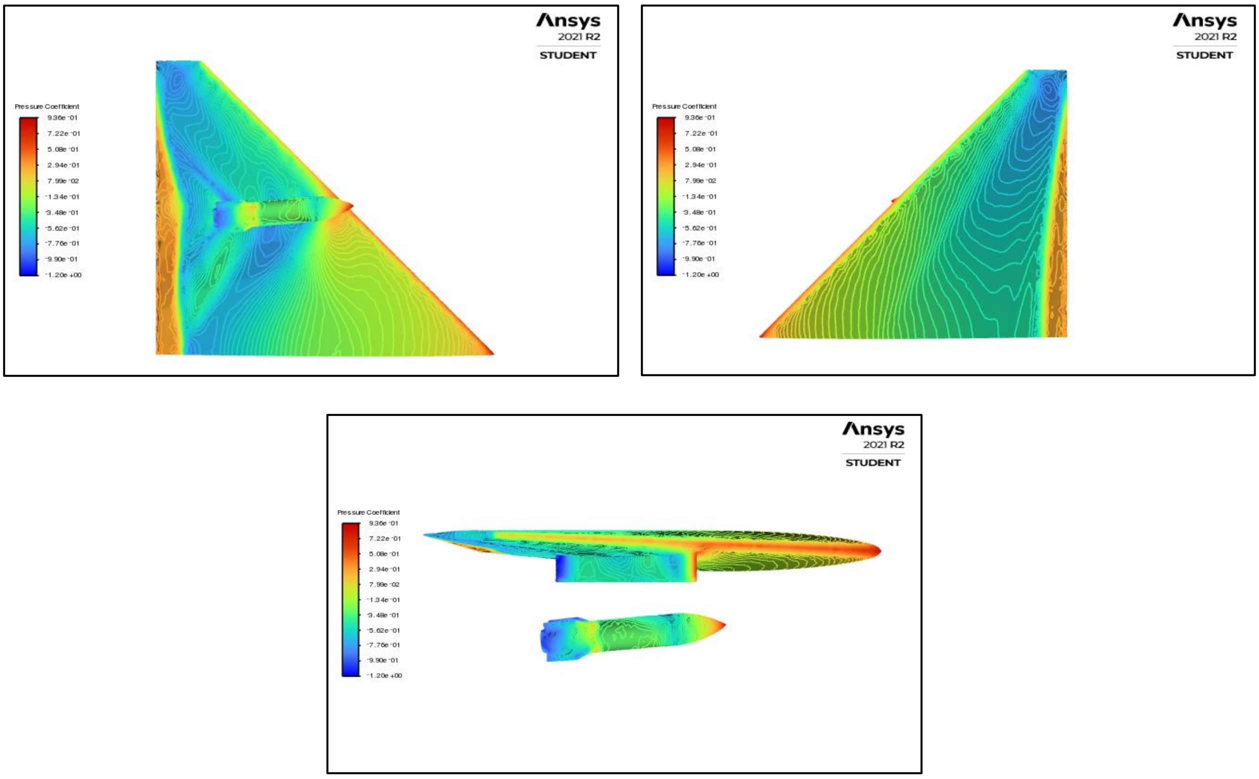

Figure 4.47 C_p contours for near position

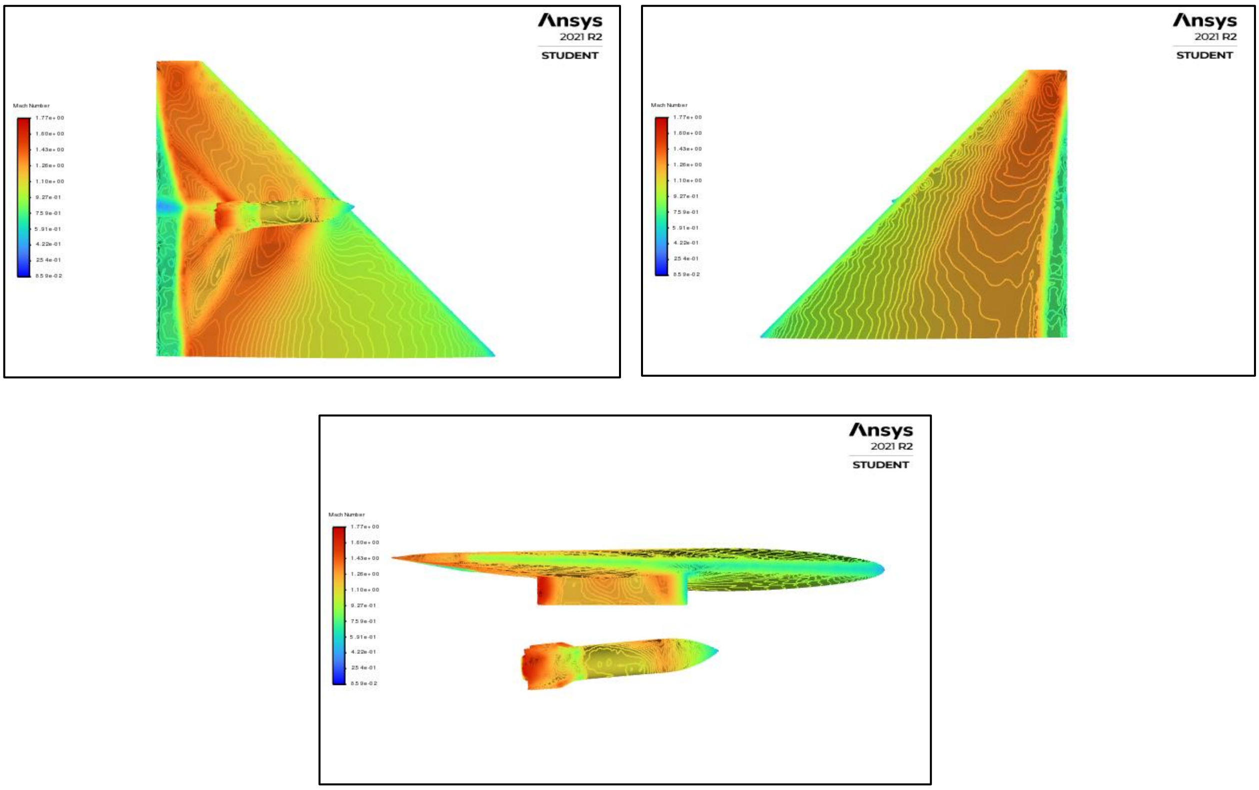

Figure 4.48 Mach contours for near position

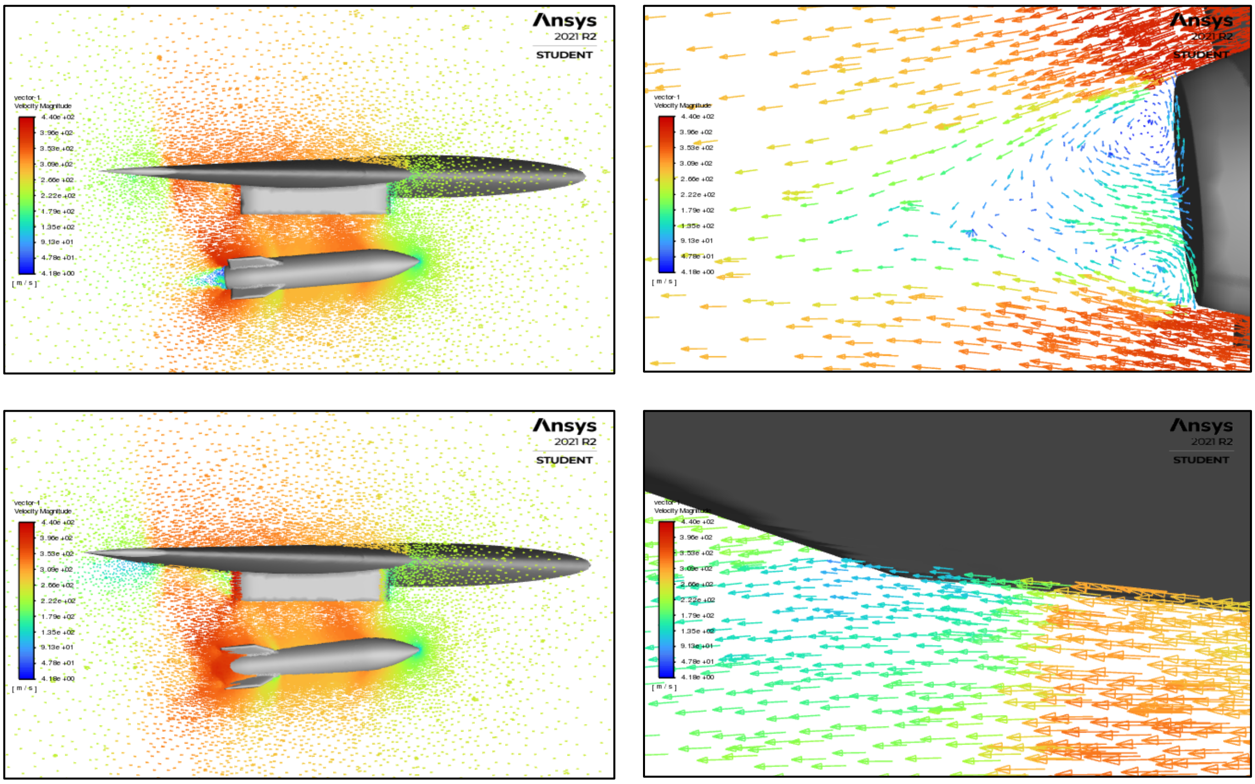

Figure 4.49 Fluid flow velocity vectors for near position

Figure 4.47 shows contours of C_p on the structure. On the upper surface of the wing, the flow expands continuously up to about 90 percent of the chord where a shock takes place. The flow on the lower surface has a significant interference effect due to the presence of the pylon and the store. The asymmetry caused by the cross flow of the wing is also evident in the C_p contours on the lower surface around the pylon.

Figure 4.48 illustrates (in terms of Mach contours) how complicated is the flow field around the wing and the store. Notice that a shock develops on the fore section of the pylon and the store (see blue region). An expansion wave is found on the aft region of the store while two additional expansion waves are found on either side of the aft sections of the pylon (see red region). Finally, a wake region (see dark blue area) develops behind the pylon, which interacts with the wing trailing edge shock. This wake region suggests that the injection of velocity close to aft region of the pylon has decreased in comparison with the carriage configuration. In other words, the Venturi effect produced by the gap is an important aerodynamic interference in the CFD model as it adds energy to the fluid flow close to that region.

Finally, **Figure 4.49** represents fluid flow velocity vectors for the near position. Top figures represent velocity vectors projected in a plane containing store's longitudinal axis and perpendicular to the global y-axis. Bottom figures, on the other hand, represent velocity vectors projected in the symmetry plane of the pylon. The weak shock originated in the very front section of the store can be easily found in the left-side figures (see blue region). On the top right-side figure, the recirculating region close to the aft region of the store is identified. It shall be noticed that this area grows as the store moves away from the pylon, since the injection of velocity delivered by the gap diminishes. Finally, the wake region close to the trailing edge of the wing is identified in the bottom left-side figure.

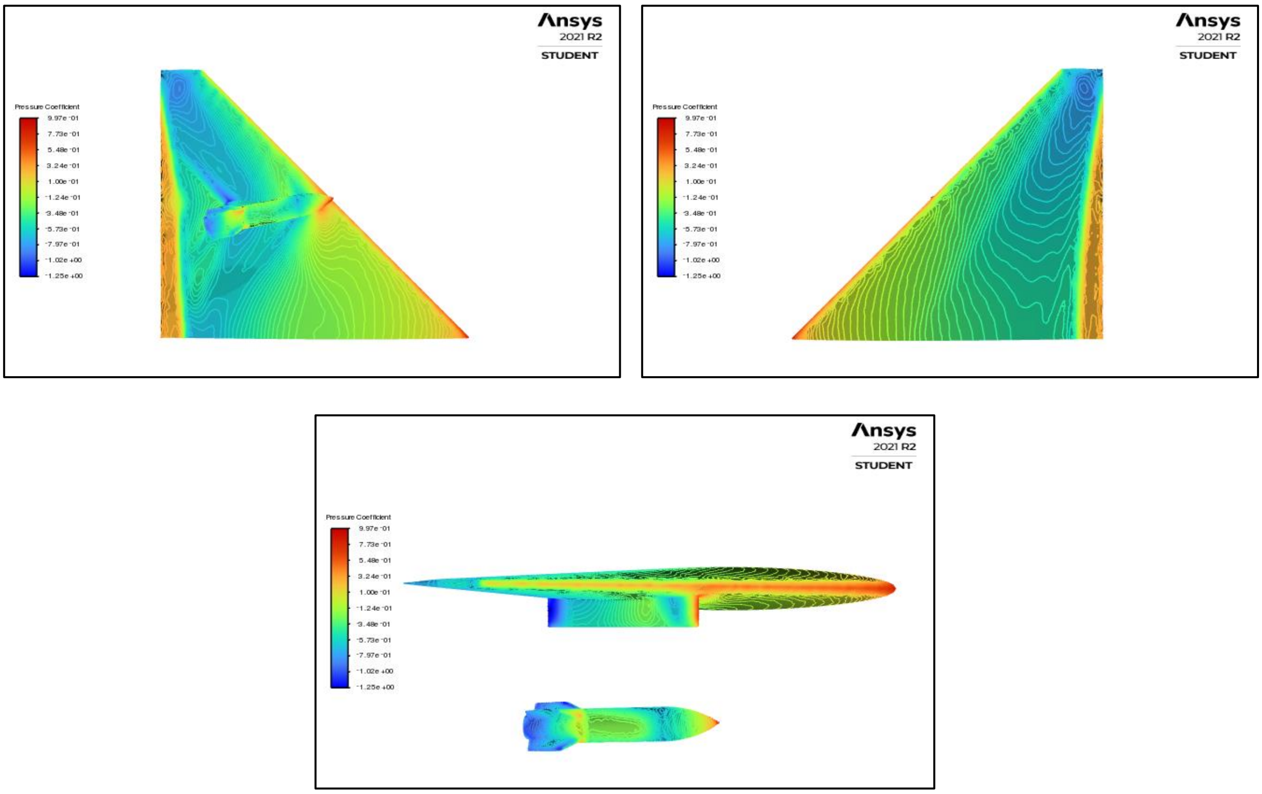

Figure 4.50 C_p contours for far position

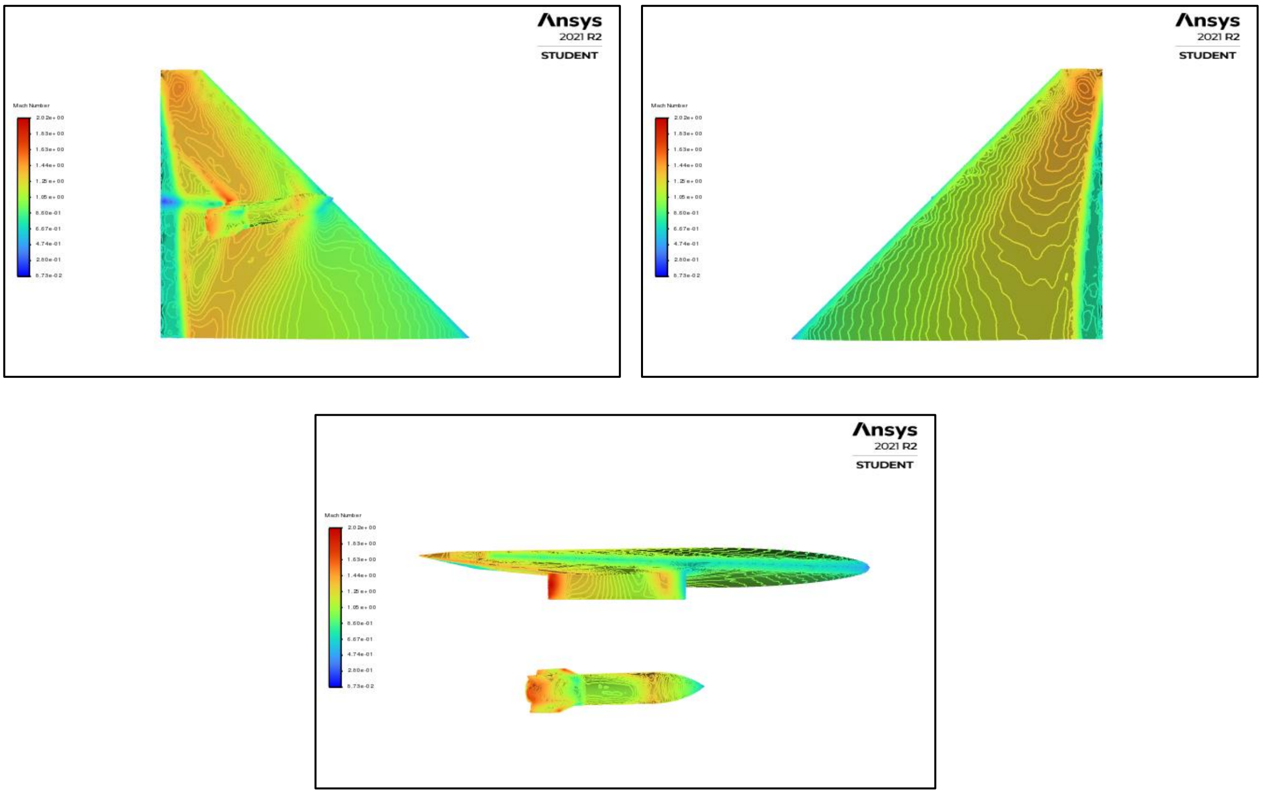

Figure 4.51 Mach contours for far position

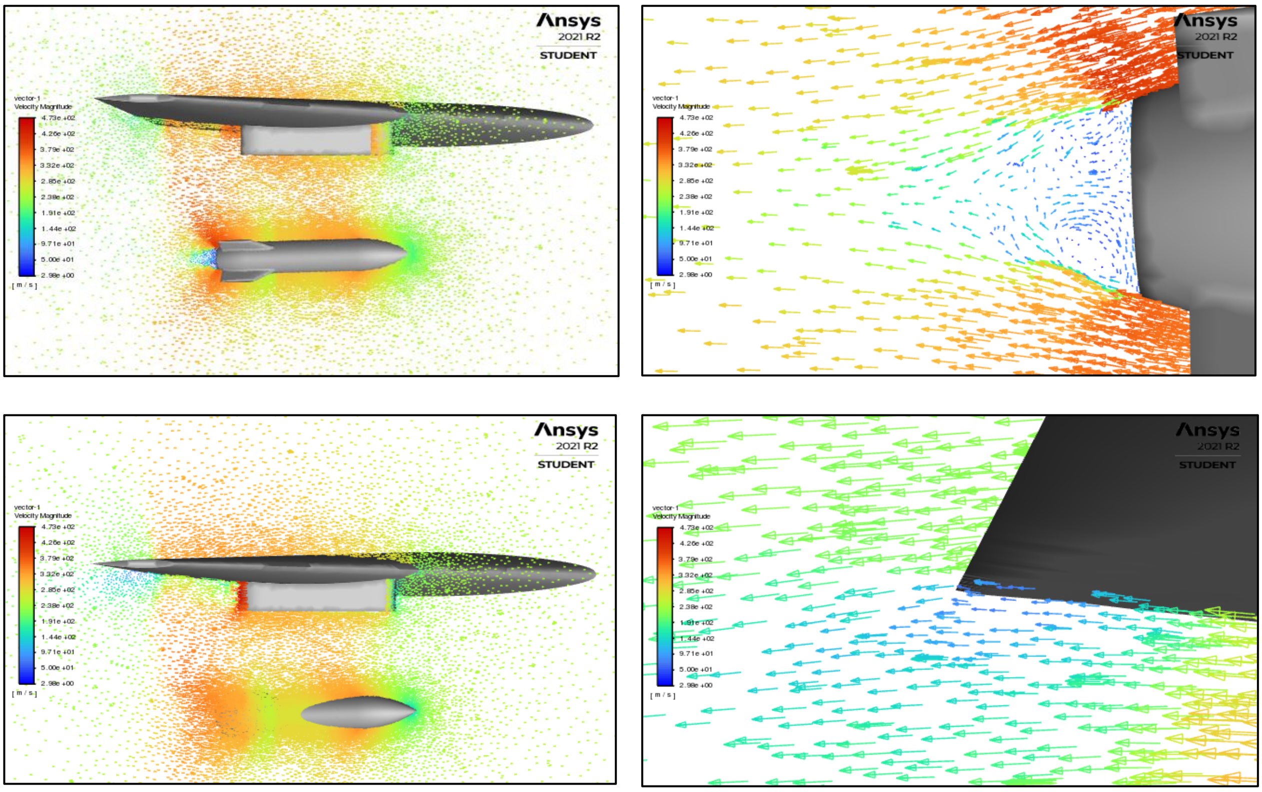

Figure 4.52 Fluid flow velocity vectors for far position

Similar conclusions can be obtained for the far position, by analysing **Figure 4.50** – **Figure 4.52**. First, it is worth noting that the wake region developed behind the pylon intensifies in comparison with the near position. This occurs because the injection of velocity close to that region vanishes since the gap between the store and the pylon is too large to trigger a Venturi effect. On the other hand, aerodynamic interferences between the pylon and the store have almost disappeared and the store might be deemed to be in free stream configuration (see bottom left-side figure in **Figure 4.52**).

4.3.1 Convergence of Solutions

At this point, a brief discussion about convergence of results shall be considered. **Figure 4.53** shows residuals' evolution with respect to the number of iterations, for the near position analysis. Even though continuity does not reach the minimum required value ($< 1e^{-5}$), the overall behaviour and convergence of the rest of residuals can be considered as a positive indicative of the good quality of the solution. A similar behaviour was observed for the far position.

Figure 4.54, on the other hand, shows the evolution of the lateral force coefficient C_Y with respect to the number of iterations. Notice that, again, there are no oscillations in its value as happened previously in the carriage configuration. The same behaviour was noticed for the rest of the force and moment coefficients, for both the near and far position.

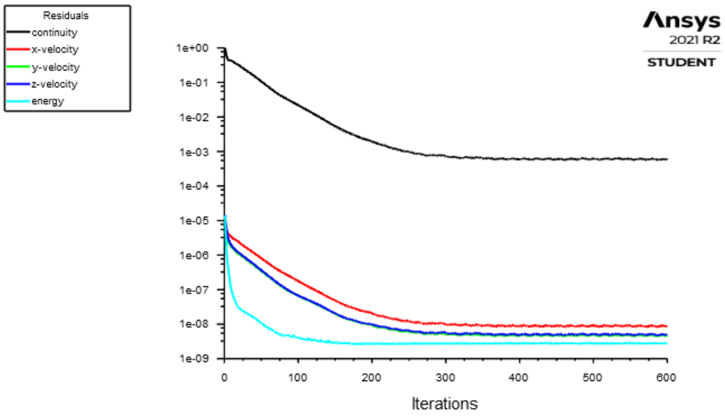

Figure 4.53 Evolution of residuals

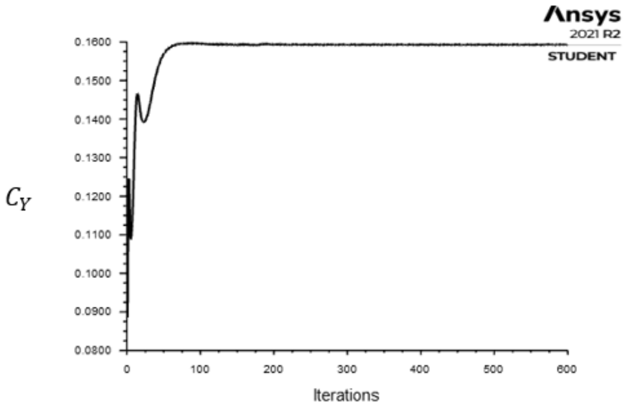

Figure 4.54 Evolution of the lateral force coefficient

5 CONCLUSIONS AND FUTURE WORK

At the end of this report, it can be concluded that the main goal of this TFM has been successfully achieved. An inviscid fluid flow solution based on an unstructured grid approach over a stationary wing/pylon/store configuration has been designed. The efficiency of the proposed setup was found to be more than acceptable as it faithfully reproduces the real behaviour of the problem. Validation against both experimental and published data has also been achieved. Not only rigid body aerodynamics and but also mutual interference effects have been explored to justify the limits of the designed CFD setup. All the conclusions obtained until this point will ease to rigorously develop non-stationary release simulations in the future.

Within this final chapter, main conclusions obtained during this work are summarised in **Section 5.1**. Finally, **Section 5.2** shows the theoretical development required to reproduce non-stationary release scenarios by means of CFD simulations.

5.1 Main Conclusions

When working with CFD tools, one must bear in mind that a particular approach may never work the best for all geometries, flight conditions and all configurations. However, as it has been demonstrated throughout this report, the problem assessed during this TFM can be correctly suited by an inviscid approach with unstructured meshing. The efficiency of the proposed setup provides an acceptable level of accuracy with a significant savings in time, effort, and computational cost. The fact that this setup was successfully demonstrated at transonic speeds makes the technique an attractive tool not only for preliminary design but also for more sophisticated assessments.

Aerodynamic force and moment coefficients are in quite good agreement with respect to both experimental data and published literature, even though some differences were detected in each geometric configuration. Particularly, some discrepancies were observed in the carriage configuration; nevertheless, ejector forces initially dominate the dynamics of the separation problem since the store is rapidly pushed far from the influence of the pylon. Consequently, these discrepancies have little impact on the final trajectory of the store.

Flow visualisation was another important tool within this TFM. Analyses of C_p distribution in different surfaces of the geometry compared very well with experimental data. Nevertheless, shock locations were predicted downstream of that measured by the experiments. The origin of this discrepancy is the inviscid nature of the CFD solution. This and other divergences were identified in areas where viscous effects were dominant (i.e., where flow separation and boundary layer growth were prevalent).

Geometry modelling was another significant source of discrepancy (e.g., the modelling of the aft region of the store and the gap between the pylon and the store). In terms of the modelling of the aft end of the store, wind tunnel model had a modified aft region followed by the Captative Trajectory Support System. The CFD model, on the other hand, did not include this device. Hence, fluid flow around this region was separated from the store's surface, according to CFD simulations. This implied a considerable increment on the base drag. On the other hand, the gap between the pylon and the store introduced some relevant perturbations with respect to the experimental data. It is possible that a better simulation of the former effect shall include boundary layer and shock-boundary layer effects.

Finally, modelling a reliable mesh was perhaps one of the most critical aspects within the CFD design process. Several factors were demonstrated to be involved but having a good comprehension about problem's physics was crucial in order to produce a mesh that guaranteed that obtained results were reliable and sufficiently close to the real behaviour. At the end, an unstructured mesh setup ensured grid independent solutions in all the configurations under assessment. Ultimately, it is worth noting that the viscous approach requires to improve some features of the mesh setup since grid quality was poor for some its elements.

5.2 Future Work. Non-stationary Release Simulations

The prediction of the trajectory of a store released form a military aircraft is an important task in the aerodynamic design area in order to define the safe operational envelope. As said in **Chapter 1**, aerodynamic and physical parameters have an influence in the solution. Aerodynamic parameters include the store shape, the velocity, attitude, and flow field around the store; physical parameters, on the other hand, include store geometric characteristics, centre of gravity position, ejector forces, etc. These parameters are highly coupled and react with each other in a complex manner. An accurate prediction of the trajectory of a store involves a correct prediction of the flow field around it, the resulting forces and moments, and an accurate integration of the equations of the motion. This implies a coupling between the CFD fluid flow solver and a 6-DOF rigid body dynamics simulator. Consequently, a computational approach for this phenomenon consists of three main components: fluid flow solver, rigid body dynamics model, and dynamic mesh algorithm.

The fluid flow solver deals with the governing fluid dynamic equations at each time step of the simulation. From that, aerodynamic forces and moments acting on the store can be computed by integrating pressure distribution over the store's surface. Knowing that, the movement of the store is computed by the 6-DOF model. Finally, the grid must be modified to account for the movement of the store by means of a dynamic mesh algorithm. The loop is then repeated for the next time step of the simulation. This procedure is schematically illustrated in **Figure 5.1**. Main considerations for each segment of the analysis are summarised below.

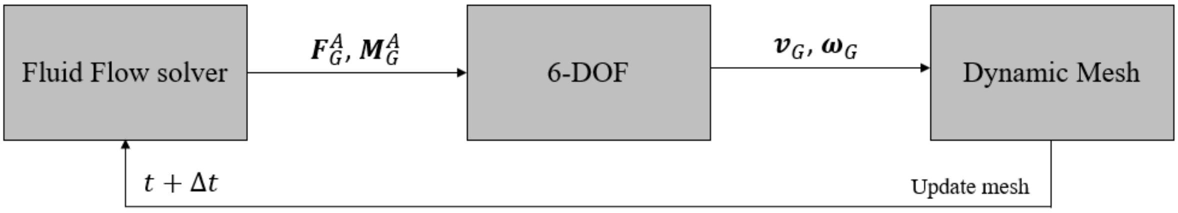

Figure 5.1 Scheme of a CFD release simulation

5.2.1.1 Fluid Flow Solver

The fluid flow solver is used to work out the governing fluid dynamic equations at each time step of the simulation. As demonstrated at the end of this work, a viscous approach is not necessary to correctly simulate this problem. Therefore, the unsteady Euler equations are integrated in ANSYS Fluent, in a similar way as it was done for the stationary configuration throughout this TFM.

The fluid flow solver setup designed in this work has demonstrated to provide accurate results; thus, it is recommended to employ the same configuration (see **Section 3.3**). The only additional setup feature that shall be considered is the type of transient formulation. In that sense, a first order implicit formulation shall be employed. It is worth pointing that a second order formulation is only recommended in cases with very low remeshing frequency [21]. Finally, the initial condition for unsteady analyses must be the fully converged steady state solution; then, the carriage configuration solution must be employed as initial condition.

5.2.1.2 Trajectory Evolution

The 6-DOF rigid body motion of the store is calculated by numerically integrating the Newton and Euler equations within ANSYS Fluent, by using the user-defined function (UDF) property. This written function is dynamically linked with the flow solver at each time step. Aerodynamic forces and moments on the store ($\boldsymbol{F}_G^A$ and $\boldsymbol{M}_G^A$) are calculated as part of the flow solver, based on the integration of pressure over its surface. This information is communicated to the 6-DOF model in inertial coordinates.

Then, the governing equation for the translational motion of the centre of gravity of the store is solved, as shown below:

$$m \cdot \dot{\boldsymbol{v}}_G = \sum \boldsymbol{F}_G \tag{5.1}$$

where $\dot{\boldsymbol{v}}_G$ is the acceleration of the store's centre of gravity, m is the mass of the store and $\boldsymbol{F}_G$ is the resultant of the all the forces applied to the store (i.e., aerodynamic forces $\boldsymbol{F}_G^A$, ejector forces, etc.).

The angular motion, on the other hand, is more easily computed in body frame coordinates to avoid variations on inertia properties:

$$I\dot{\boldsymbol{\omega}}_B + \boldsymbol{\omega}_B \times I\boldsymbol{\omega}_B = \sum \boldsymbol{M}_B \tag{5.2}$$

where I is the inertia tensor and $\boldsymbol{M}_B$ is the total moment of the store in the body reference frame. Notice that the orientation of the body frame with respect to the global frame can be tracked by using a standard 321 Euler rotation sequence, as shown in **Appendix C**. Therefore, moments can be transformed from inertial to body reference frame by:

$$\boldsymbol{M}_B = R\boldsymbol{M}_G \tag{5.3}$$

where R is the transformation matrix defined in **Appendix C** and $\boldsymbol{M}_G$ is the total moment of the store in the global reference frame.

Once the translational and angular accelerations are computed from equations **(5.1)** and **(5.2)**, rates can be determined by numerical integration. Several approaches can be used, from very simple procedures such as the Euler method:

$$x^{k+1} = x^k + \frac{1}{2}\dot{x}^k \tag{5.4}$$

to more sophisticated techniques such as the Adams-Moulton formulation, recommended in [16]:

$$x^{k+1} = x^k + \frac{\Delta t}{24}\left(9\dot{x}^{k+1} + 19\dot{x}^k - 5\dot{x}^{k-1} + 2\dot{x}^{k-2}\right) \tag{5.5}$$

where x in equation **(5.4)** and **(5.5)** represents either $\boldsymbol{v}_G$ or $\boldsymbol{\omega}_B$.

It must be noticed that the dynamic mesh algorithm takes as input $\boldsymbol{v}_G$ and $\boldsymbol{\omega}_G$; therefore, the angular velocity shall be transformed back to inertial coordinates by:

$$\boldsymbol{\omega}_G = R^T \boldsymbol{\omega}_B \tag{5.6}$$

Remember that an important characteristic of R is that $R^{-1} = R^T$. This simplifies numerical calculations.

According to the experimental test [10], the store is forced away from the wing/pylon structure by means of identical piston ejectors located in the lateral plane of the store (18 cm forward from the centre of gravity and 33 cm aft, respectively). The ejector forces operate for the duration of $t_{ops} = 0.054\ s$ after releasing the store and they extend during operation for 10 cm. The force of each ejector is a constant function of this stroke extension with values of $10.7\ kN$ and $42.7\ kN$, respectively (see **Figure 5.2**).

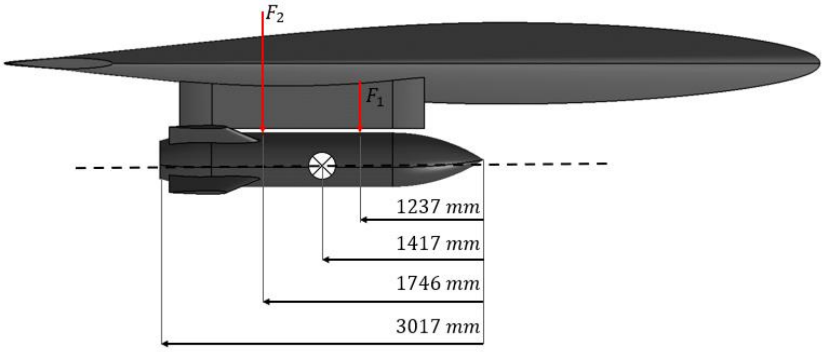

Figure 5.2 Ejector force data

Finally, the basic physical properties of the store and the ejector forces required for dynamic simulations are summarised in **Table 5.1**.

Magnitude	**Value**
Mass, $m\ [kg]$	907
Axial moment of inertia, $I_{xx}\ [kg \cdot m^2]$	27
Transverse moment of inertia, I_{yy} and $I_{zz}\ [kg \cdot m^2]$	488
Forward ejector location, $L_1\ [m]$	1.237 (after store nose)
Forward ejector force, $F_1\ [kN]$	10.7
Aft ejector location, $L_2\ [m]$	1.746 (after store nose)
Aft ejector force, $F_2\ [kN]$	42.7
Ejector stroke length, $l_{ops}\ [m]$	0.1

Table 5.1 Store physical properties for dynamic simulation

5.2.1.3 Dynamic Mesh

A dynamic mesh method is another crucial component within a release simulation in ANSYS Fluent. Combined with the 6-DOF solver, a dynamic mesh method allows the trajectory of the moving object to be determined. There are three different schemes within ANSYS Fluent (i.e., smoothing, layering, and remeshing), depending on the features of the problem. For a store release problem, the remeshing method option shall be employed since it deals with situations where the boundary displacement is large compared to the size of the local cells.

Finally, it must be remembered from **Chapter 2** that experimental trajectory propagations summarised in [10] were computed based on a quasi-steady approximation, in which steady flow at sample points along the store trajectory is used to derive loads. One must be aware of that when comparing CFD results against experimental data.

REFERENCES

[1] A. Arabshahi and D. Whitfield, "A multiblock approach to solving the three-dimensional unsteady Euler equations about a wing-pylon-store configuration," in *16th Atmospheric Flight Mechanics Conference*, 1989.

[2] E. Covert, "Conditions for safe separation of external stores," *Journal of Aircraft,* vol. 18, no. 8, pp. 624-630, 1981.

[3] A. Cenko, E. Tinoco, R. Dyer and J. DeJongh, "PAN AIR applications to weapons carriage and separation," *Journal of Aircraft,* vol. 18, no. 2, pp. 128-134, 1981.

[4] A. Calder, "The E-Fan X puts its aerodynamic design to the test," AIRBUS, 4 February 2020. [Online]. Available: https://www.airbus.com/newsroom/stories/The-e-fan-X-puts-its-aerodynamic-design-to-the-test.html. [Accessed 2 November 2021].

[5] K. Keen, "New approaches to computational aircraft/store weapons integration," in *28th Aerospace Sciences Meeting*, Reno, Nevada, 1990.

[6] R. Koomullil, G. Cheng, B. Soni, R. Noack and N. Prewitt, "Moving-body simulations using overset framework with rigid body dynamics," *Mathematics and Computers in Simulation,* vol. 78, no. 5-6, pp. 618-626, 2008.

[7] W. Westmoreland, "A comparison of inviscid and viscous approaches for store separations," in *20th AIAA Applied Aerodynamics Conference*, 2002.

[8] D. Snyder, E. Koutsavdis and J. Anttonen, "Transonic store separation using unstructured CFD with dynamic meshing," in *33rd AIAA fluid dynamics conference and exhibit*, 2003.

[9] L. Rojas, "Effect of Free-Stream Turbulence Intensity on Transonic Airfoil with Shock Wave," ResearchGate, 09 2017. [Online]. Available: https://www.researchgate.net/figure/Transonic-flow-illustration_fig1_319603937. [Accessed 10 03 2022].

[10] E. Heim, "CFD wing/pylon/finned store mutual interference wind tunnel experiment," ARNOLD ENGINEERING DEVELOPMENT CENTER ARNOLD AFS TN., 1991.

[11] R. Meyer, A. Cenko and S. Yaros, "An influence function method for predicting store aerodynamic characteristics during weapon separation," GRUMMAN AEROSPACE CORP BETHPAGE NY, 1981.

[12] M. Madson, S. Moyer and A. Cenko, "TranAir computations of the flow about a generic wing/pylon/finned-store configuration," in *32nd Aerospace Sciences Meeting and Exhibit*, 1994.

[13] J. Sahu and J. Danberg, "Navier-Stokes computations of transonic flows with a two-equation turbulence model," *AIAA journal,* vol. 24, no. 11, pp. 1744-1751, 1986.

[14] D. MacLucas and I. Gledhill, "Modelling flow phenomena in time dependent store release from transonic aircraft," 2014.

[15] P. Parikh, S. Pirzadeh and N. Frink, “Unstructured grid solutions to a wing/pylon/store configuration using VGRID3D/USM3D,” in *Astrodynamics Conference*, 1992.

[16] E. Panagiotopoulos and S. Kyparissis, “CFD transonic store separation trajectory predictions with comparison to wind tunnel investigations,” *International Journal of Engineering,* vol. 3, no. 6, pp. 538-553, 2010.

[17] N. Prewitt, D. Belk and W. Shyy, “Parallel computing of overset grids for aerodynamic problems with moving objects,” *Progress in Aerospace Sciences,* vol. 36, no. 2, pp. 117-172, 2000.

[18] F. Moukalled, L. Mangani and M. Darwish, The finite volume method in computational fluid dynamics, Berlin, Germany: Springer, 2016.

[19] W. contributors, “Shock wave,” Wikipedia, The Free Encyclopedia, 18 01 2022. [Online]. Available: https://en.wikipedia.org/w/index.php?title=Shock_wave&oldid=1066505219. [Accessed 14 03 2022].

[20] R. Nichols, in *Turbulence Models and Their Application to Complex Flows*, Birmingham, University of Alabama, p. 214.

[21] I. ANSYS, “ANSYS Fluent Theory Guide,” 2013.

[22] C. Brennen, Law of the wall, An Internet Book on Fluid Dynamics.

[23] F. White, Fluid Mechanics, McGraw Hill, 2015.

[24] I. ANSYS, “Pressure Far-Field Boundary Conditions,” 29 01 2009. [Online]. Available: https://www.afs.enea.it/project/neptunius/docs/fluent/html/ug/node245.htm. [Accessed 08 02 2022].

[25] A. Danilov, “Unstructured tetrahedral mesh generation technology,” *Computational Mathematics and Mathematical Physics,* vol. 50, no. 1, pp. 139-156, 2010.

[26] H. Schlichting and K. Gersten, Boundary-Layer Theory, Springer, 2017.

[27] V. Vorobyov, “ResearchGate,” 03 2015. [Online]. Available: https://www.researchgate.net/figure/the-law-of-the-wall-dimensionless-horizontal-velocity-near-the-wall_fig8_294578412. [Accessed 15 02 2022].

[28] S. Hoerner, “Base drag and thick trailing edges,” *Journal of the Aeronautical Sciences,* vol. 17, no. 10, pp. 622-628, 1950.

[29] D. MacLucas and I. Gledhill, “Time-accurate transonic CFD Simulation of a generic store release case,” *R&D Journal,* vol. 34, pp. 9-16, 2018.

[30] N. Tabatabaei, R. Vinuesa, R. Örlü and P. Schlatter, “Techniques for turbulence tripping of boundary layers in RANS simulations,” *Flow, Turbulence and Combustion,* pp. 1-22, 2021.

APPENDICES

A. International Standard Atmosphere

The International Standard Atmosphere (ISA) is a static atmosphere model of how air's properties such as pressure, temperature, or density of the Earth's atmosphere change over a range of altitudes. It was stablished to provide a common reference for temperature and pressure and consists of tables of values at various altitudes, plus some formulas to which those values are derived.

ISA model divides the atmosphere into layers with linear distributions of temperature and it is based upon average conditions. The values of interest for this report are shown in **Table A.1**, where a is known as the thermal gradient.

Layer	$h_0\ [m]$	$a\ [K/km]$	$T_0\ [K]$	$p_0[Pa]$	$\rho_0[kg/m^3]$
Troposphere	0	−6.5	288.15	101325	1.225
Tropopause	11000	0	216.65	22632	0.3639
Stratosphere	20000	1.0	216.65	5474.9	0.0880

Table A.1 International Standard Atmosphere

Intermediate values of temperature, pressure, and density can be found numerically. Equations **(A.1) - (A.3)** represent values for $a = 0$,

$$T(h) = T_0 \tag{A.1}$$

$$p(h) = p_0 \cdot e^{-\frac{g}{RT}\cdot(h-h_0)} \tag{A.2}$$

$$\rho(h) = \rho_0 \cdot e^{-\frac{g}{RT}\cdot(h-h_0)} \tag{A.3}$$

whereas equations **(A.4) - (A.6)** represent values for $a \neq 0$,

$$T(h) = T_0 + a \cdot (h - h_0) \tag{A.4}$$

$$p(h) = p_0 \left(\frac{T(h)}{T_0}\right)^{-\frac{g}{aR}} \tag{A.5}$$

$$\rho(h) = \rho_0 \left(\frac{T(h)}{T_0}\right)^{-1-\frac{g}{aR}} \tag{A.6}$$

It is worth mentioning that within those equations $R = 287\frac{m^2}{s^2K}$ is the universal gas constant and g is gravity constant.

B. Computational Geometry

This appendix shows additional information about geometric generation by means of technical drawings. Each dimension shown in **Figure B.1** to **Figure B.5** is expressed in meters.

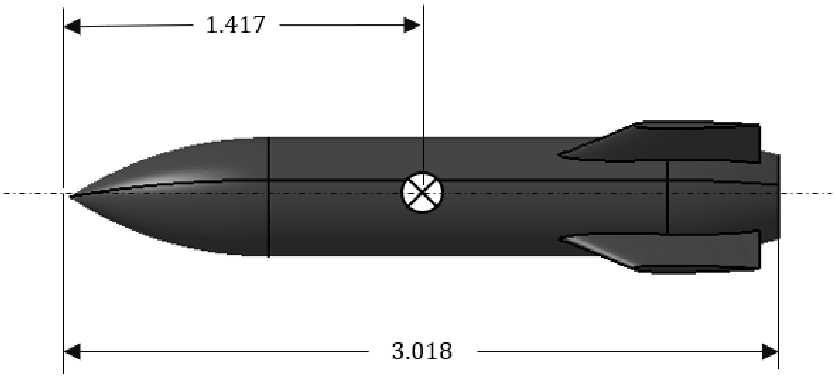

Figure B.1 Store's centre of gravity position

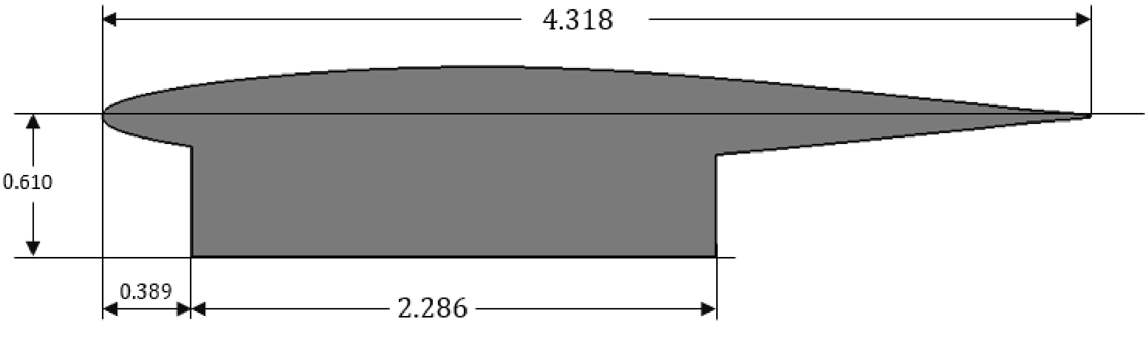

Figure B.2 Pylon dimensions (view looking outboard)

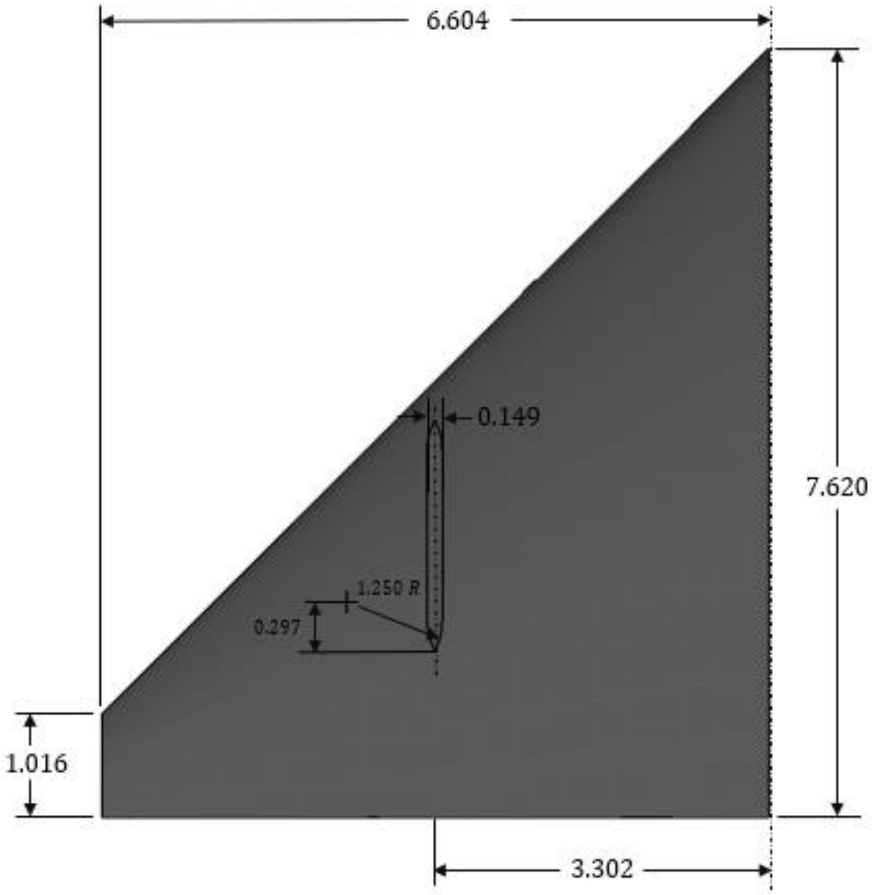

Figure B.3 Wing lower surface dimensional data

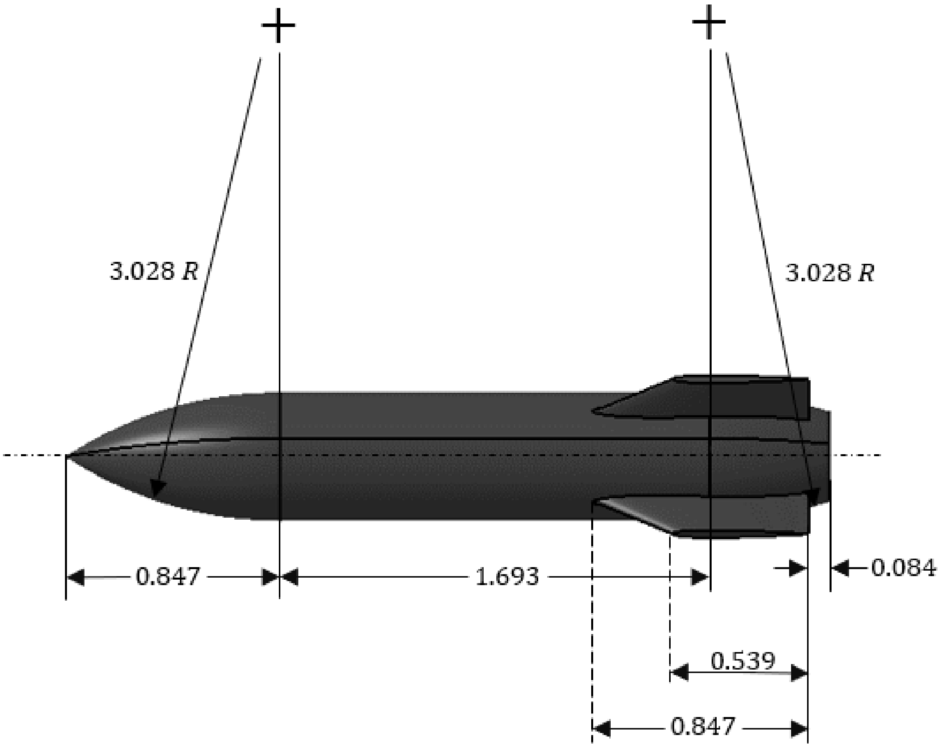

Figure B.4 Store model dimensional data I

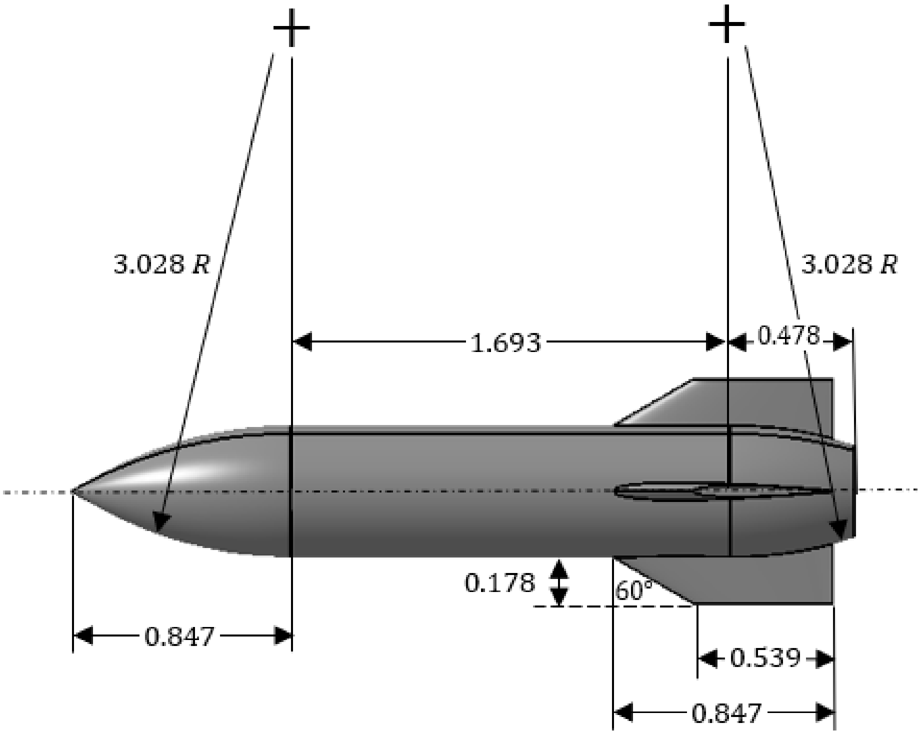

Figure B.5 Store model dimensional data II

C. 321 Euler Transformation

An Euler sequence is defined by three simple frame transformations which, applied successively, combine to physically rotate a rigid body within the same reference frame (when active transform is considered). Each transformation in the sequence corresponds to a rotation about a basis frame axis. Each transformation in the sequence is parameterised by an angle, therefore the overall transformation is parameterised by 3 angles plus the knowledge of the order in which the elementary transforms are performed. Overall, there are 12 distinct Euler sequences.

In particular, the 321 sequence is performed in the following order:

- The first rotation of ψ is about the z-axis of the original frame (i.e., the global reference frame).
- The second rotation of θ is about the y-axis of the first intermediate frame.
- The third rotation of ϕ is about the x-axis of the second intermediate frame.

Combining the three elementary rotation matrices give the overall Direction Cosine Matrix (DCM), represented by equation **(C.1)**,

$$R = \begin{bmatrix} c\theta c\psi & c\theta s\psi & -s\theta \\ s\phi s\theta c\psi - c\phi s\psi & s\phi s\theta s\psi + c\phi c\psi & c\theta s\phi \\ c\phi s\theta c\psi + s\phi s\psi & c\phi s\theta s\psi - s\phi c\psi & c\theta c\phi \end{bmatrix} \tag{C.1}$$

where the shorthand notation $c\alpha = \cos\alpha$, $s\alpha = \sin\alpha$ is used.